Environmental Mechanics Research in China

LI JIACHUN, LIU QINGQUAN, and ZHOU JIFU

Department of Engineering Sciences, Institute of Mechanics, Chinese Academy of Sciences, Beijing 100080, China

Abstract

By recalling mankind's path during past 50 years in the present article, we mainly highlight the significance of environmental issues today. In particular, two major factors leading to environment deterioration in China such as water resources and coal burning are stressed on.

Present-day environmental issues are obviously interdisciplinary, of multiple scales and multi-composition in nature. Therefore, a process-based approach for environment research is absolutely necessary. A series of sub-processes, either physical, chemical or biological, are subsequently analyzed in order to establish reasonable parameterization

E-mail address: candj@dial.pipex.com (L. Jiachun).

scheme and credible comprehensive model. And we are now in a position to answer questions still open to us, improve existing somewhat empirical engineering approaches and enhance quantitative accuracy in prediction.

To illustrate this process-based research approach, three typical examples associated with the Yangtze River Estuary, Loess Plateau and Tenggli Desert environments have been dealt with, respectively. A theoretical model of vertical flow field accounting for runoff and tide interaction has been established to delineate salinity and sediment motion which are responsible for the formation of mouth bar at the outlet and the ecological evolution there. A kinematic wave theory combined with the revised Green–Ampt infiltration formula is applied to the prediction of runoff generation and erosion in three types of erosion region on the Loess Plateau. Three approaches describing water motion in SPAC system in arid areas at different levels have been improved by introducing vegetation sub-models. However, we have found that the formation of a dry sandy layer and biological crust skin are additional primary causes leading to deterioration of water supply and succession of ecological system.

I. Introduction

The 20th century has seen the emerging need for environmental fluid mechanics and the need has been increasing with time after the World War II. The grave pollution events such as the stifling smoke in hazy winter of London were astonishingly alarming to rouse attention in the 1950s. As pointed out in the book 'Silent Spring' by R. Carson in the 1960s, the revelation of severe pesticide pollution as a primary cause set a milestone for the world to recognize the threat from environment degradation. The United Nations Conference on Human Environment (UNCHE) was convened in 1972 to promote the resolution of these emerging problems. Consequently, the United Nations Environment Program (UNEP) was established in Nairobi, Kenya, followed by signing up of a series of international treaties. Under these circumstances, the representatives of both developed and developing countries gathered at the United Nations Conference on Environment and Development (UNCED) held at Rio de Janeiro, Brazil to explore the compromise between environment protection and economic development in the world. Just as G. H. Brundtlands suggested in the well-known book 'Our Common Future,' a new concept of sustainable development has become a consensus. It means that such a kind of developmental mode must meet the demand of the current generation without doing any harm to the coming generations (Fuwa, 1995; Li and Wu, 1998). The environmental problem can perhaps be traced back as early as to the time of sparsely populated and primarily agrarian world long past, but the impacts on the communities were then negligible. With the world population rapidly growing and urban centers expanding, the adverse effects have gradually become vital and urgent (Reible, 1999).

Nowadays, the environment issues in contemporary society are noted to have the following characteristics and salient features:

(1) Comprehensive environmental irregularities occur more frequently. As a result, the so-called environment problems should be investigated and understood in a broader sense. They include worldwide climate anomalies such as the cold summer in 1980, warm winter in 1989, dry weather in 1984, 1986 and 1987. In addition, such natural disasters as abrupt variations in temperature, rainfall, wind force and water level generally have inflicted heavy tolls upon the living world and properties. Toxic industrial discharges and daily life contaminants released to the air, water and soil bodies constitute the primary cause of environmental pollution. Degradation of the ecological environment arises usually by overgrazing and deforestation. Such ecosystem unbalances are known to lead to worsening consequences that are responsible for desertland formation, pasture degeneration and loss of biological diversity. In particular, the aforementioned episodes tend to occur interactively rather as solitary cases. For example, the pollution by phosphorus compounds tends to give rise to overgrowth of algae, thus resulting in breaking out of red tide. The global warming tends to induce flooding of coastal cities owing to the rise of sea surface level (Bigg, 1996; Singh, 1996).

(2) The loss in environmental events becomes increasingly more severe. The principal characters of a contemporary society are industrialization and urbanization, the speed of which is much accelerated in today's developing countries. In case an accident should take place suddenly without warning, the loss of properties and lives could be overwhelming. Such cases now seem to be the rule rather than merely incidental. This is clearly exhibited by the long list of the natural hazards such as flood and drought, hurricane and tornado, storm surge and tsunami, volcano eruption and earthquake, landslide and debris flows, snow avalanche and dust storm, etc. It is estimated in a report issued by the Adversary Committee on International Decade of Natural Disaster Reduction (INDNR) that natural hazards have claimed more than 2.8 million lives, together with adversely affecting 820 million people during 1979–1990. On the most severe occasions in Bangladesh and China, one single disaster is already seen to have taken more than one quarter million lives, plus the accompanied property damage evaluated at 25–100 billion USD.

(3) The influences of adverse human activities can be significant. Some of the environmental problems may be due to certain natural causes. Nevertheless, the adverse human activities now have become comparable with or even surpassing the roles of natural factors. The major impact of this category is evidently shown by the total effects of burning of fossil fuels on the local and regional air quality and on its role as a dominant contributor to the green house gases emitted into

the atmosphere. Aerosols affect climate by scattering and absorbing solar radiation. At the same time, they form condensation nuclei that are critically responsible for cloud formation and precipitation. The natural sources of aerosols are volcano debris released in volcano eruption and the dissolved salt contained in the sea water spray thrown into the air during wave breaking and left to ride in air updrafts. The routes of human activities in altering aerosol number density and size distribution are through industrial emission and biotic marine fluxes of Dimethyl Sulphide (DMS) flux into the air. As is known and reported, the combustion of fossil fuel and the burning associated with deforestation may add 87 Tg sulfur, about 1.5 times of the amount by natural emission, annually into the atmosphere. The daily phenomena of low visibility range, increased cloud cover, and especially the acid rain falling over North America and European continents amply afford the evidence of sulfate aerosol accumulation. The land use and cover change (LUCC) such as from forest to arable land and from savannah to desert in habitable regions is also enormous. The effects of LUCC are not only restricted to altering surface albedo, moisture and thermal characters, but also through affecting global carbon cycling. It is reported that over the last 200 years, the contributions from fossil fuel combustion and land use conversion are approximately comparable. In addition to its central role in affecting global change, many facets of human welfare are closely linked to LUCC, including biological diversity and food production (Bernard, 1981; Jager, 1988; Bigg, 1996).

Looking forward to the future at the turn of the century, the world population will most likely continue to grow on this globe already populated with more than 6 billion of people, especially in Africa, India and Southeast Asia. Furthermore, the magnifying requirement of material civilization will certainly result in consumption of more energy and resources. It seems that the pressure of environment degradation will not be alleviated shortly and hence the environmental issue will certainly remain a challenging problem in the 21st century (Fuwu, 1995; Li and Wu, 1998; Reible, 1999).

II. Environmental Problems in China

As a developing country with an area of 9.60 million km^2 and population of 1.295 billion, China is facing great challenge in environmental issues to maintain the current speed for economic booming. In most western part of China far from east coastal line are mountains and plateaus. The Tibet plateau prevents vapor over the India Ocean from penetrating into inner land. Consequently, water is always a central issue in most provinces in China. Except for natural factors,

humanity's activities, especially dramatic explosion of population and inappropriate cultivation of land further deteriorate the situation. In the following, we shall address in detail China's principal environmental issues, in particular, those associated with water resources:

A. WATER RESOURCES AND HYDROLOGY HAZARDS

It is estimated that the total amount of water resources available is 2800 billion cubic meters annually, ranking the sixth in the world. However, the water supply per capita is 2162 m^3, merely one fourth of the world's average level. Moreover, they are not evenly distributed either seasonally or geographically. The situation that contaminated water tends to be released without processing further aggravates its emergency. More than tens of big cities, in particular, the metropolises are commonly confronted with shortage of water. Some of the great rivers such as the Yellow River even dries out downstream more frequently in the 1990s, which may last as long as half a year. Excessive use of water without planning in upstream provinces accounts for the cause. Except for management in water use, the government has lately decided to initiate 'China's South Water to North Transfer' project including three routes in the near future in order to mitigate the severe crisis. The middle route project (MRP) with a free flow trunk as long as 1240 km shall annually transfer 14.5 billion m^3 of water to highly cultivated and water-deficient Huang-Huai-Hai plain. Similarly, the Tarimu river in the south Xinjiang province formed a green corridor in the desert in the last century. However, the ecological environment downstream have been severely threatened by river shrinkage of 320 km since 1950. Recent transfer of 0.7 billion m^3 of water from the Bosten lake into the Tarimu river refills the disappearing Teitema lake, saving patches of dying popular diversifolia. In contrast, the great rivers are not always calm as have been reflected by more frequent catastrophic flooding in the 1990s. The disaster in 1998, comparable to those in 1931 and 1954, was the most severe one, resulting in total property loss of 25 billion USD (Table I). Consecutive torrential rains due to anomalous activity of atmospheric circulation and reclamation of land around lakes in the Jingjiang region were responsible for why high level water failed to retreat during July and August of 1998. Densely populated and well-developed flood diversion areas brought about more difficulties for us to make decision. Besides, land subsidence, debris flow, saltwater intrusion, sediment transport are all among the same category (Singh, 1996).

TABLE I
COMPARISON OF THE YANGTZE RIVER FLOOD IN 1954 AND 1998

	Hankou		Yichang	
	Flux (m³/s)	Water level (m ASL)	Flux (m³/s)	Water level (m ASL)
1954	70,700	29.73	63,600	55.73
1998	72,300	29.43	66,800	54.50

B. SOIL EROSION AND DESERT INVASION

Owing to unfavorable climatic conditions in the Northwest China, arid and semi-arid areas occupy 3.78 million km^2 (39% of total area). Desert scatters along the north border of China and forms a belt as long as 4000 km with the width of 600 km. Their total area amounts to 0.71 million km^2. The largest one is the Takramagan desert with an area of 0.33 million km^2. Anthropogenic activities along with adverse weather conditions accelerate the speed of desert invasion, the annual rate of which turns out to be 2.46 thousand km^2. Total area has amounted to 2.62 million km^2 (27%) (Table II). Soil erosion carrying away 5 billion ton fertile surface soil annually by wind or water is the major cause leading to soil erosion. Take the Loess Plateau as an example, the eroded area is 0.43 million km^2. The most serious situation has an erosion module as large as 30,000 ton/km^2. As for downstream, the direct consequences are waterway blockage and water pollution. Furthermore, wind erosion brings about more frequent sandstorms in the north China in the last decade. During recent economy boost in the west China, we should pay prior attention to these problems in order to render this area more beautiful than before.

C. OTHER ISSUES

An additional influential issue in this respect is the coal-dominated energy structure, namely, coal (70%), petroleum (22%), hydropower (5%), natural gas

TABLE II
CHINA'S LAND USE INDICES

	Arid and semi-arid	Deserted land	Desert	Erosion
Area (million of km^2)	3.78	2.62	0.71	3.60
Proportion (%)	39.3	27.2	7.39	37.5

TABLE III
CHINA'S MAJOR POPULATION AND ENERGY PRODUCTION INDICES

	Population (billion)	GDP per capita (USD)	Coal (billion T)	Oil (billion T)	Gas (billion m^3)	Electricity (G kWh)
1953	0.62	–	0.11	–	–	12
1964	0.72	–	0.20	–	–	73
1982	1.03	196	0.62	0.10	–	379
1990	1.16	313	1.00	0.15	1.53	623
2000	1.29	842	1.00	0.16	3.00	1209

(2%) and others. It is reported that China's GDP has surpassed 10,000 USD and GDP per capita has been enhanced from 114 USD in 1970 to 842 USD in 2000. We may expect that the living standard will stride forward in foreseeable future. Although the growth rate of population has been slowed down to less than 1%, we still have to make great effort to combat pollution during the period of economy boost. The government has taken measures to accelerate the construction of carbon-free hydro- and nuclear power station. Total capacity of hydropower and nuclear power plants amounts to 72.8 and 2.1 GW, respectively, by the end of 2000. The production of natural gas with lower carbon emission is also doubled from 15.3 to 30 billion m^3 during the last 10 years (Table III). Therefore, the pattern of energy consumption is unable to change significantly in a short period though, the implement of energy conservation and efficiency enhancement along with the above-mentioned policy have certainly contributed to reducing global carbon dioxide and local sulfur oxides emissions (Jager, 1988; Zhang, 1994).

III. Process-Based Research Approach

Conventionally, the task of an environmental engineer is to copy with the foregoing episodes, aiming at minimizing any potential adverse effects and abating human's losses of traditional industrial and agricultural activities. Sometimes it is simply understood as finding some solutions to manipulate pollution events. Any efforts in modeling are regarded as useless for 'being wise after the event'. For a long time, collecting field data became a major job for the researchers in this field to establish an empirical formula. Nevertheless, this mode of investigation has often given way to process-based approaches. Since the former tends to obtain right answer for the wrong reasons rather than right reason, in the mean while, the latter verifying each process component as well as the final output and avoiding parameter optimization is more credible and preferred for

scientists and engineers in environmental field nowadays. It has been recognized that this kind of research approach, namely process-oriented modeling can fulfill the task of demonstrating the past event, predicting the future evolution, assessing the impact of an action and evaluate the effectiveness of human's intervention. In particular, the experiments on a large scale or for a long-term are always expensive or even beyond people's capability, the process-based model is the unique selection (Reible, 1999; Parsons and Abrahams, 1992).

Basically, any environmental problem is aroused by fluid-carried mass or energy transport. Even earthquake is indirectly relevant to mantle convection, which drives tectonic motion, magma plume and volcano eruption. However, the flows in nature seem to be considerably different from typical industrial flows with external forcing such as boundary layer, channel flows, pipe flows, mixing layer, wakes and jets. In general, buoyancy due to density difference is dominant over or at least equally important as shear stress in them. On the other hand, how the mass and energy are redistributed by convection-accompanied diffusion is also crucial. Moreover, it is commonly found that many physical, chemical or even biological phenomena are involved in more complex environmental issues. Hence, the analysis of them underlying the environmental problem is a preliminary step for process-oriented research. Therefore, we will describe those processes peculiar to environmental fluid flows in nature at first (Lumley *et al.*, 1996; Li, 2001a).

A. Sub-process Analysis

1. *Flows in Nature*

a. *Atmosphere Boundary Layer*

Atmospheric boundary layer (ABL) driven by outer free atmosphere and sensitively affected by ground indicates the lowest part of troposphere where human beings are inhabiting. Its importance is evidently attributed to the fact that the turbulent flows in ABL play a decisive role in climate variation and air pollution. According to atmospheric stability, ABL is usually classified into three categories: unstable convective boundary layer (CBL), neutral boundary layer and stable boundary layer (SBL). CBL in atmosphere is a multi-layered structure with the height h of about $1-2$ km and consists of surface layer (<0.1 h), mixing layer ($0.1-0.8$ h) and entrainment layer ($0.8-1.2$ h). The surface layer is characteristic of velocity shear and constant momentum flux. The mixed layer exhibits strong mixing feature of its buoyancy-driven turbulence and the highest

layer is influenced by entrainment effects, capping version and stable atmosphere aloft. In contrast, SBL ranging from 10 to hundreds of meters demonstrates small fluctuation and strong vertical inhomogeneity. In the 1960s, one of the most significant advances is the Monin–Obukhov theory and people endeavored to elucidate the mean behaviors such as fluxes and profiles. The most popular one accounting for stability effects on the average wind speed u is the Businger–Dyer formula verified by observations in Wagnara, Australia:

$$u = \frac{u_*}{\kappa}\left(\ln\frac{z}{z_0} - \psi_{\mathrm{M}}\right) \tag{3.1}$$

where u_* is the friction velocity, κ the Karman constant, z_0 the roughness and ψ_{M} a function of ς, which is of different form for stable and unstable circumstances and

$$\varsigma = \frac{z}{L}, \qquad L = \frac{\vartheta(\tau/\rho)^{3/2}}{\kappa g(H/\rho C_{\mathrm{p}})}, \tag{3.2}$$

in which L denotes the Monin–Obukhov length measuring the relative importance of wind shear and buoyancy. The statistical behaviors and coherent structure of turbulence were obtained by large eddy simulation (Deardorff, 1970; Moeng, 1984), in which large scale eddies are responsible for most of the energy transfer whereas those smaller than grid size can only be modeled. As for CBL, the research was directed to counter gradient transfer, entrainment nearby the tropopause and the role played by convective vortices and the asymmetry in updraught and downdraught flows has been identified. In contrast, the investigation of SBL relatively lags behind because of the difficulties in the interaction between internal waves and turbulence, variable height of SBL and low turbulence intensity measurement (Li, 1993; Garratt and Taylor, 1996). Owing to the damping induced by vegetation, the velocity profile exhibits inflexion nearby canopy and a shear layer is formed there. The mixing layer analogue brought forth lately by Finnigan (2001) has further deepened our understanding of canopy turbulence. The emphasis of the future study should be laid on cloud capped ABL, inhomogeneous underlying surface effects and their applications in global and regional circulation models (Garratt and Taylor, 1996).

b. *Bottom Boundary Layer*

The bottom boundary layer means the layer inside which the flow is substantially influenced by the bed and is generated by moving water or a plate back and forth in the laboratory. In coastal engineering, such kind of unsteady boundary layer is formed under water surface wave or tidal flows adjacent to

the bottom (Nielsen, 1992; Li *et al*., 1999b). The thickness of this oscillatory boundary layer is estimated as:

$$\delta_s = \sqrt{\nu T} \tag{3.3}$$

where ν is the kinetic viscosity, and T a typical period. Generally speaking, a wave-induced boundary can be as thick as a few millimeters, whereas tide-induced boundaries can extend to the whole water body owing to its longer period. Hence, wave-induced high stresses at the seabed could initiate sediment to re-suspend, while tidal flows could carry away suspended sediment. Hence, it is considerably significant to establish the quantitative links between the flow fields and the rates of morphological changes. The velocity profile of a laminar oscillatory boundary layer of circular frequency ω in z direction is given by:

$$u(z,t) - u_\infty(t) = A\omega \exp(-(1+\mathrm{i})z/\delta_s)\mathrm{e}^{\mathrm{i}\omega t} \tag{3.4}$$

where A indicates the amplitude. The transition to turbulence is generally dependent on the Reynolds number in terms of the oscillatory boundary layer thickness:

$$Re = A\sqrt{\frac{2\omega}{\nu}} \tag{3.5}$$

and bed roughness. The flow can be classified as laminar, disturbed laminar, intermittent turbulent and full-developed turbulent states. For smooth bed, the flow is found to remain laminar for $Re < 100$, to become turbulent for $Re > 3500$, and to appear partly laminar and partly turbulent for Re lying in between (Nino and Garcia, 1996; Li *et al*., 1999b). If we consider motion adjacent to solid or free surface or around small structure in waves, the viscous wave theory should be applied. Previous in-depth research (Lamb, 1945; Phillips, 1977) has given dissipation effects in waves due to viscosity. If the viscosity is assumed small, the difference between ideal and viscous waves with wavenumber k merely lies in that the amplitude decays exponentially at the rate of:

$$d = 2\nu k^2 \tag{3.6}$$

In practical applications, we need to examine the combined wave–current interaction boundary layer and also consider the effects of coastal line and topography.

c. *Buoyancy-Induced Convection*

As we know, density variations due to in-homogeneity in temperature and physico-chemical composition in various natural environment can give rise to buoyancy-induced flows, such as CBL, upwelling in the ocean, thermohaline

circulation, and mantle convection (Turner, 2000). With the characteristic velocity left unknown, the non-dimensional parameter for buoyancy-induced convection is the Grashof number defined as:

$$Gr = \frac{\alpha g \Delta T L^3}{\nu^2} \qquad (3.7)$$

where α is the bulk expansivity, g the gravity acceleration, ν the kinetic viscosity and L a characteristic length. For environmental flows at low speed with small density difference, we tend to assume the Boussinesq approximation, that is, the fluid is assumed incompressible except for that in the buoyancy term. The thermal plume over a heat source such as chimney or cooling water exhaust thus penetrates upward into stably stratified fluid, entrains ambient fluid and finally descends. The previous work has quantitatively answered the question concerning the rise height, flow inversion and mixing process. More attention should be paid to convection in porous media and with phase change (Lumley *et al.*, 1996).

d. *Flows in Rotating System*

To investigate geophysical flows on this rotating planet with angular velocity Ω, the effects of the Coriolis force is measured by the ratio of the inertial and Coriolis forces, the so-called Rossby number:

$$R_\text{o} = \frac{U}{fL} \qquad (3.8)$$

where $f = 2\Omega \sin \phi$ is the Coriolis parameter at the latitude ϕ, U and L are the characteristic velocity and length, respectively. Since the air in the atmosphere generally moves faster than the water in the ocean, the rotating effects should be accounted for those flows with length scale order of 1000 km (for the atmosphere) or with length scale order of 100 km (for the ocean). Typical examples are geostrophic flows, Taylor's column, Ekman effect and western strengthening of wind-driven circulation. If we restrict ourselves to a narrow latitude zone, we can adopt the *f*-plane or the β-plane approximation. A unique feature of rotating systems is their conservation of potential vorticity. Therefore, a Beta gyre appears during the movement of tropical cyclones. Such internal asymmetric structure is responsible for anomalous trajectory (Li and Kwok, 1997). Since the vertical velocity component is much smaller than the horizontal ones, the large-scale motion essentially is quasi-two-dimensional. Without vortex stretching, we have adverse energy cascade and normal entropy cascade. For this reason, geophysical fluid is a natural laboratory of two-dimensional turbulence.

In addition, people find that the vortices within the critical distance tend to merge (Hopfinger, 1988; Lumley *et al*., 1996; Turner, 2000).

2. *Transport of Mass and Energy*

In nature, there are varieties of minute particulates of different sizes such as smoke, dust, volcano debris, salt, fog, sediment, pollen and virus, of which those with diameter between 1 and 100 nm constitutes aerosol and suspensions in liquid. For investigating such systems, a non-Newtonian model (for densely concentrated sediment, mud), or a multiphase model, or passive scalar model may be applied. Here, by the so-called passive scalar model, it is meant that the concentration of dispersate is so rare that the motion of the dispersive medium is not affected, that is, there is no coupling between dispersate and dispersive medium. Instead, we shall be rather concerned with the diffusion, settling and flocculation of dispersate in dispersive media.

a. *Diffusion*

In laminar flows, the diffusivity can be derived based on kinetic theory. On the other hand, the Taylor theory for turbulent flows shows that the displacement variance in short duration is proportional to the time square and that in long-term to the time interval. Consequently, the turbulent diffusivity is finally proportional to the velocity variance and Lagrange integral time scale (Brenner and Stone, 2000). As far as suspending liquid is concerned, the migration of minute particles with radius R at temperature T in fluid is caused by the Brownian motion, and the corresponding diffusivity may be written as (where k is the Planck constant):

$$D = \frac{kT}{6\pi\mu R} \qquad (3.9)$$

Recent research on passive scalar indicates the differences in statistical behaviors between velocity and passive scalar fields: pdf of passive scalar is no longer Gaussian even for Gaussian velocity field; the passive scalar of grid turbulence exhibits a scale law even at low Reynolds numbers; passive scalar demonstrates more intermittent than the velocity and inhomogeneity appears in an inertial and dissipative range. Therefore, this area requires more exploration (Warhaft, 2000) to clarify for better understanding. In addition, we should emphasize on a key point that the turbulence structure in large scale plays a dominant role in the transport of momentum, mass and energy.

b. *Deposition*

Dispersate particles deposit in the gravity field and thus become separated from the dispersive medium. For small particles moving in dilute suspension at low Reynolds numbers, the Stokes formula is generally used to calculate the viscous drag and particle settling speed. For spherical droplets or bubbles in gas or water, the drag is smaller, versus their solid counterpart, owing to the motion of the internal fluid brought by the outer fluid, yielding a somewhat larger settling speed. Further, for larger Reynolds numbers and dispersate deformation, the settling speed can be calculated based on the following expression (Levich, 1962):

$$U = \sqrt{\frac{2\rho'gV}{C_d\rho S}} \tag{3.10}$$

in which V is the volume of a liquid droplet or gas bubble, S its frontal area, C_d stands for the drag coefficient, ρ and ρ' are the densities of particles and liquid (or gas), respectively. In addition, surfactants in liquid may further alter the deposition process. The aforementioned process is essential to studies of sediment motion, dry deposition, and wet scavenge in formulating acid rain models.

c. *Flocculation*

It is possible that dispersate particles may move to distances so close that the intermolecular Van der Waals force plays an active role in leading to flocculation. However, the repulsive force due to discharge at the particle surface is a stable factor to prevent them to come too close. Otherwise, flash flocculation would take place instead. We may obtain the temporal evolution of the number density in flocculation due to the Brownian motion as:

$$n = \frac{n_0}{1 + t/T}, \qquad T = (8\pi D R n_0)^{-1} \tag{3.11}$$

where R is the flocculation radius (equal to the diameter of the particle), D the diffusivity by the Brownian motion, T the characteristic time of flocculation. Flocculation is found to occur during the transport of aerosols in atmosphere and of sediment in estuaries. In the presence of prevailing flow fields, flocculation in shear flows is called the gradient flocculation. In this connection, dissolution, emulsification, etc. seem to need further investigations. Absorption, adsorption, and similar mass exchange at fluid interfaces should also deserve attention in environmental engineering.

3. *Other Physical, Chemical and Biological Processes*

a. *Radiation*

Solar radiation is the energy source for living creatures on the earth to grow and the major driving force of atmospheric and oceanic motion as well. The average flux at the outer edge of atmosphere on average is defined as the solar constant with minor variation:

$$I_0 = 1.97 \text{ Kar/cm}^2 \text{ min} = 1374 \text{ w/m}^2$$

which is updated based on the recent satellite measurements. Varying with the solar activity and distance between the sun and the earth, the solar radiation actually is represented as:

$$I = \frac{I_0}{\rho^2} (\sin\phi \sin\delta + \cos\phi \cos\delta \cos\omega) \tag{3.12}$$

where ρ is the relative distance between the sun and the earth, ϕ the latitude, δ the declination, and ω the temporal angle. Penetrating through the atmosphere, the direct radiation is estimated by transparency or turbidity and cloud quantity S. There are gas molecules, aerosol and water droplets in the atmosphere. The Rayleigh scattering occurs around the gas molecules with the radius smaller than electromagnetic wave length, while Mie scattering occurs around aerosols with diameter equivalent to electromagnetic wavelength. The scattering coefficient dependent on wavelength is inhomogeneous in different directions. In this way, the total radiation on the ground Q turns out to be the sum of the direct radiation S and the scattered radiation q:

$$Q = S + q \tag{3.13}$$

Depending on the color, moisture and roughness of the underlying surface, the ground reflects the incident waves, namely, albedo α. On the other hand, the long wave reflection from the ground is partly returned back to the ground, namely, the adverse radiation. The difference between them is known as effective radiation E. Based on the radiation balance at the ground, the net radiation R is derived as:

$$R = (1 - \alpha)Q - E, \tag{3.14}$$

which is responsible for where the sensible, latent and ground fluxes come from (Rosenberg, 1974; Ten Berge, 1990; Dingman, 1994). In water quality models, the solar radiation penetration should also be taken into consideration to understand the growth and metabolism of phytoplankton (Hamilton and Schladov, 1997).

b. *Chemical Reaction*

Some typical chemical reactions in the environmental sciences and technology that should be concerned with are listed as follows (Fuwa, 1995; Lei *et al*., 1998; Reible, 1999):

Reactions in ozone layer: While ozone is uniformly distributed in the troposphere, it drastically decreases in the stratosphere due to diffusion and dissociation. Ultraviolet radiation depletes ozone through the reactions by chlorine atom from chloroflurocarbons (CFC) released to the atmosphere as follows:

$$Cl + O_3 \rightarrow ClO + O_2 \qquad ClO + O \rightarrow Cl + O_2 \qquad (3.15)$$
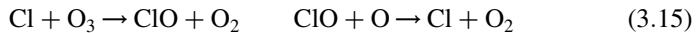
Since atomic chlorine may be continuously generated by the reaction of chlorine monoxide with atomic oxygen in stratosphere, the foregoing chain reaction may indeed be self-maintaining. This explains why single atomic chlorine in the atmosphere may remain for such a long time to break tens of thousand of ozone molecules. The reactions in the stratosphere seem to be very complicated; hydrogen, free radical of hydroxide, methane and oxides of nitrogen take part in the process directly or indirectly. Very probably, the inhomogeneous reaction of gas phase at the surface of sulfate aerosol should be considered to elucidate the formation of ozone hole over the Antarctic continent.

Mechanism of acid rain formation: The oxides of sulfur or nitrogen in the atmosphere are the principal elements to acidify rain. The reactions to produce acidified materials are as follows:

$$SO_2 + OH + M + O_2 + H_2O \rightarrow H_2SO_4 + M + HO_2 \qquad (3.16)$$
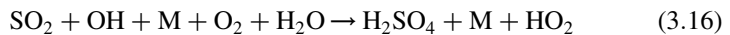
where M is a third matter. The chain reaction may be continued because the free radical of OH is generated again in the reactions. As for the reaction of nitric acid formation, it turns out that:

$$OH + NO_2 + M \rightarrow HNO_3 + M \qquad (3.17)$$
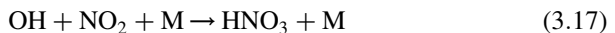
of which the reaction rate is one order higher than that for sulfuric acid formation. As a result, the lifetime of oxides of nitrogen is only one day, much shorter than that of oxides of sulfur. For this reason, it is only for long distance transport of pollutants that we need to consider effects of chemical reactions, dry deposition and wet scavenge (Lei *et al*., 1998).

c. *Biological Processes*

For green plants, the metabolism of water, mineral and organic matters are going on regularly. Water absorbed through roots is evaporated through

leaf stoma. The metabolism of organic matters is fulfilled by photosynthesis:

$$6CO_2 + 12H_2O \xrightarrow{\text{light, chlorophyll}} C_6H_{12}O_6 + 6H_2O + 6O_2 \qquad (3.18)$$
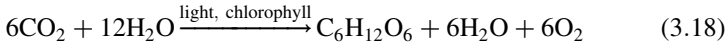
which turns the inorganic compounds into primary sugar to form complex sugar, starch, cellulose, etc. and stores the photo energy in the form of dry material in the plant. It should be noticed that plants are capable of adapting to the ambient environment. For instance, the evaporation diminishes due to lack of water in dry season, a process that can be represented with parameterization (Rosenberg, 1974). In modeling eutrophication of lakes and oceans, many factors should be considered such as the growth of zooplankton, metabolism of phytoplankton, cycling of nutritive salt, dissolved oxygen, conservation of total phosphorus and nitrogen. In considering long-term climate models, the geophysical biochemical cycling of dioxide oxygen is of significance (Hamilton and Schladov, 1997).

d. *Ecological Succession*

As is well known, all living creature experiences a process from a preliminary to an advanced one, or from a simpler to more complicated ones. When resources are enough to maintain a favorable condition, species evolve and ecological system tends to mature. Generally speaking, such natural evolution takes hundreds of million or billion years. Nevertheless, the alteration of species in short term (a few or tens years) known as succession occurs by external humanity's disturbance such as storm, wild fire, overgrazing and deforestation. The researchers should pay due attention to this kind of environmental variation (Bernard, 1981; Luo and Shen, 1994).

B. PARAMETERIZATION

The foregoing environmental problems cover a wide range of the spatial scales reducing from global, synoptic, meso-watershed to turbulence, and the temporal scales from century to seconds (Beniston, 1998). It is because the external forcing such as periodic variation of solar magnetic field and sunspot, motions of the sun, moon and earth is intrinsically of multiple scale in nature. For instance, the tilt of the earth axis with an average of 23.5° varies between 22.1° and 24.5° with a period of 40,000 years. And it precesses at a period of 20,000 years. In addition, the orbit eccentricity also changes with a period of 105,000 years (Bigg, 1996; Dingman, 1994; Watt, 1998). These variations in the solar orbit account for the fact that the ice sheet expands and recedes with a period of 100 kyr modulated by

cycles of 20 or 40 kyr due to radiation variation. The nonlinear interaction between external forcing with different periods leads to manifesting of multiple scale phenomena.

The parameterization in environmental problems has two implications. On the one hand, the sub-process analysis should be ended up with a quantitative description by supplementing new variables, new terms or even new equations and by altering boundary conditions reflecting the constituting sub-processes. On the other hand, we may have subgrid model to represent the influences arising from unresolved scales on the resolved scales, which is commonly seen in the research of turbulence and geophysical fluid mechanics. We consider it as a significant task in solving environmental problems (Smagorinsky, 1963; Galperin and Orszag, 1993; Lesieu and Metais, 1996; Zhou, 1998; Li and Xie, 1998; Li, 2001b).

C. Integrated Models

We note that while incorporating the last two procedures, an integrated model can be constructed. For establishing such a comprehensive model, the main points should cover factors as follows: firstly, the model should be simple and concise enough to achieve computational efficiency as well as to reflect its validity. Secondly, the relationship between different physical elements and factors involved should be correctly established. In this regard, the aforementioned sub-processes are indispensable elements in modeling the phenomenon found in nature. Therefore, each of them should be thoroughly investigated and verified by analysis, computation and even by laboratory experiments. Of course, we are able to borrow the mature results available in different fields. With such a comprehensive model established, more challenging undertakings such as answering controversial issues, revealing implied mechanism and improving prediction can be fulfilled.

IV. Case Study

A. Sediment Transport and Sea Water Intrusion in the Yangtze River Estuary

Scientists in the hydrodynamics field in China have focused their investigations on estuarine environmental problems in recent decades. On the one hand, many environmental events such as water pollution, toxic algae bloom, sea water intrusion, and waterway blockage have more frequently occurred than

ever before in over-populated areas. On the other hand, the complexity involved in interactions between various underlying influential factors seems to be really overwhelming. As a case study, the Yangtze River estuary, the most important waterway in China, is indeed typical. In the Yangtze River Estuary, there exists a very complex topography of islands and shoals spreading over the multi-forked river exit to the open sea. The quite large Chongming Island separates the North and South Branches of the Yangtze, while the Changxing and Hengsha Islands further divide the South Branch into the North and South Waterways. Again, the South Waterway bifurcates into the North and South Channels (see Fig. 1). Unfortunately, Typhoon 8310 in 1983 left with a legacy of a vast blockage of the South Channel with a great amount of sedimentation. People had to give up the South Channel, resorting instead of dredging the North Channel for a navigation passage since then. However, the minimum water depth in this channel was only about 7 m near the mouth bar formed by sediment deposition. Consequently, a waterway deepening project has been planned to construct two levees, with three groins attached at each of them, along the sides of the North Channel (the layout of the first phase hydrostructures is shown in Fig. 1) in order to maintain a proper flow rate of water in the navigation waterway and to facilitate sediment sluice (Zhou *et al.*, 2000).
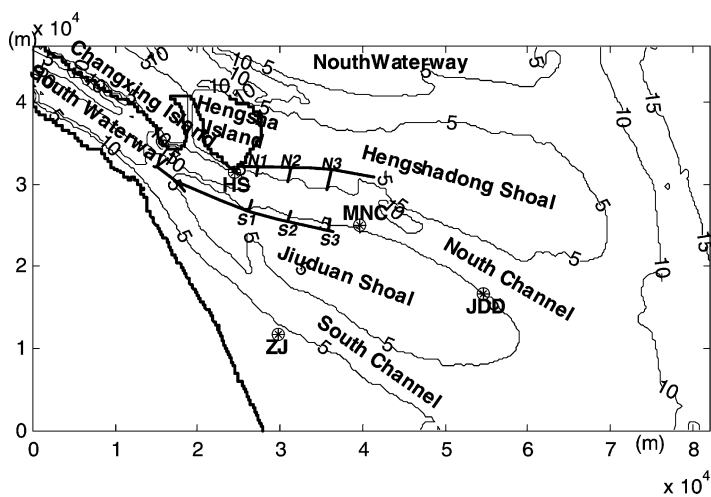

FIG. 1.	General Bathymetry of the North and South Channel in the Yangtze River Estuary. The thin solid lines are bathymetric isobars with a 5-m increment. In the domain, there are four gauging stations: Hengsha (HS), Middle of North Channel (MNC), Jiuduandong (JDD) and Zhongjun (ZJ), which are marked by circled stars. The two thick solid lines in the center of the domain are the levees of the first phase project with groins N1, N2, N3 and S1, S2, S3 attached.

Associated with this project, engineers and scientists are much concerned with the following problems: What are the major impacts on the environment that are feasible to arise from the project, for instance, will the sea water interface by sea water intrusion shift downstream or upstream? Will there be any alteration in sediment transport and turbidity maximum, which could have direct influence on the growth of phytoplankton and zooplankton? What will be the annual and diurnal variations in salinity and sediment concentration in the Yangtze River Estuary? Whether or not the waterway may maintain a certain depth at affordable maintenance cost in dredging. (Luo and Shen, 1994). We plan to delineate our recent fundamental investigations in this section to explore these challenging problems in the area of estuarine environment.

1. *Ruling Factors for Estuarine Flow and Mass Transport*

a. *Runoff and Tide Interaction*

Runoff and tide are two major dynamic factors that can substantially affect estuarine flow and mass transport. In the Yangtze River Estuary, both runoff discharge and tide flooding volume are enormous. The annual total runoff recently recorded amounts to 925 billion m^3 with the mean discharge as high as 29,300 m^3/s. The maximal discharge of 92,600 m^3/s and the minimal one of 6020 m^3/s were reported in history. It belongs to a weakly or intermediately mixing estuary with mean tidal level of 2.66 m observed at Zhongjun tide station. In the meantime, the tidal flood discharge may reach 264,000 m^3/s, nine times the mean runoff (Zhou *et al.*, 1999b).

For better understanding of sediment transport processes in estuaries, we should first examine the vertical structure of estuarine flows in detail as due to interaction of tide and runoff (Zhou *et al.*, 1999a). In estuarine regions, tide forces the fluid to oscillate back-and-forth, thus resulting in an essentially periodic flow field. For instance, there are four different phases or segments in one tidal cycle: namely, low water rapid (LWR) with maximal ebb speed; high water rapid (HWR) with maximal flood speed; low water slack (LWS) when the flow turns from ebb to flood; and high water slack (HWS) when the reverse occurs. For the sake of convenience, we define u_{max}^{ζ} and U_{max} as the top velocity and the depth-integrated mean velocity, respectively, at LWR; u_{min}^{ζ} and U_{min} as the minimum and depth-mean minimum velocities at HWR, respectively. Around the instants of rapid water stage, the current runs in a manner very much similar to the unidirectional flow in rivers, owing to long tidal period, lasting usually 12 or 24 h. While around the slack water period, flow reversal occurs. The flow is evidently characterized by the fact that the current in the lower layer is generally opposite

to that in the upper layer. Nevertheless, runoff superposed on tides may produce a seaward net flux throughout. Therefore, we have $u_{\text{max}}^{\zeta} > -u_{\text{min}}^{\zeta}$ and $U_{\text{max}} > U_{\text{min}}$ generally. To facilitate analysis, we decompose the runoff and tidal components as follows:

$$U = U_{\text{c}} + U_{\text{w}} \tag{4.1}$$

$$u(z) = u_{\text{c}}(z) + u_{\text{w}}(z), \tag{4.2}$$

where U is depth-averaged mean velocity, $u(z)$ the longitudinal current component at vertical coordinates z, U_{w}, U_{c} denote the tide and runoff components of U, respectively; and likewise for the $u_{\text{w}}(z)$, $u_{\text{c}}(z)$ components of $u(z)$. Obviously, $u_{\text{w}}(z)$ can be derived from u_{w}^{ζ}, the tide component of the speed at the free surface, by applying an oscillatory boundary layer theory. Similarly, $u_{\text{c}}(z)$ can be expressed in terms of u_{c}^{ζ}, the runoff component of the speed at the free surface, by using the logarithmic law for unidirectional flow velocity, which is accurate enough for engineering purpose. For further analysis, we define

$$u_{\text{c}}^{\zeta} = \tfrac{1}{2}[u_{\text{max}}^{\zeta} + u_{\text{min}}^{\zeta}], \tag{4.3}$$

$$u_{\text{w}}^{\zeta} = \tfrac{1}{2}[u_{\text{max}}^{\zeta} - u_{\text{min}}^{\zeta}]\cos\phi \tag{4.4}$$

where ϕ denotes the tidal phase. The above variables are functions of x, t or x, z, t. For simplicity, the symbols x and t will be omitted.

According to the logarithmic law of velocity profile, we have

$$u_{\text{max}}^{\zeta} = U_{\text{max}}\left(1 + \frac{n\sqrt{g}}{\kappa h_{\text{max}}^{1/6}}\right) \tag{4.5}$$

$$u_{\text{min}}^{\zeta} = U_{\text{min}}\left(1 + \frac{n\sqrt{g}}{\kappa h_{\text{min}}^{1/6}}\right) \tag{4.6}$$

where κ is the von Karman constant, n is the Manning roughness coefficient, and h_{max}, h_{min} are the water depths corresponding to U_{max} at LWR and U_{min} at HWR, respectively.

Hence, the vertical two-dimensional structure of estuarine flow can be delineated by oscillatory boundary layer theory and runoff-tide decomposition approach as stated above. In this way, $u(z)$, vertical distribution of horizontal velocity component, can be deduced from the time series of U, depth-averaged velocity. Furthermore, $w(z)$, distribution of vertical velocity component, can be obtained with the help of continuity equation.

We begin our analysis by investigating the relationship between $u_c(z)$ and u_c^ζ. Integrating the logarithmic formula

$$\frac{u_c(z)}{u_{*_c}} = \frac{1}{\kappa}\ln z + \text{const} \tag{4.7}$$

over the vertical stretch yields

$$\frac{U_c}{u_{*_c}} = \frac{1}{\kappa}\ln h - \frac{1}{\kappa} + \text{const} \tag{4.8}$$

in which u_{*_c} is the friction velocity of the runoff component of estuarine flow and h the water depth. Substitution of h for variable z in Eq. (4.7) leads to

$$\frac{u_c^\zeta}{u_{*_c}} = \frac{1}{\kappa}\ln h + \text{const} \tag{4.9}$$

Subtracting Eq. (4.7) from Eq. (4.9), we have

$$\frac{u_c^\zeta - u_c(z)}{u_{*_c}} = \frac{1}{\kappa}\ln\frac{h}{z} \tag{4.10}$$

Subtracting Eq. (4.9) from Eq. (4.8), we have

$$u_c^\zeta = U_c + \frac{u_{*_c}}{\kappa} \tag{4.11}$$

By using the Manning formula we have:

$$u_{*_c} = n\sqrt{g}U_c/h^{1/6} \tag{4.12}$$

Solving the simultaneous Equations (4.10)–(4.12), we obtain the relationship between $u_c(z)$ and u_c^ζ which reads

$$u_c(z) = u_c^\zeta\left(1 - \frac{1}{1 + \dfrac{\kappa h^{1/6}}{n\sqrt{g}}}\ln\frac{h}{z}\right) \tag{4.13}$$

We consider next the relationship between $u_w(z)$ and u_w^ζ. As the reference frame is fixed at the bottom, the velocity at the water surface oscillating with a simple harmonic mode as

$$u_w^\zeta = \tfrac{1}{2}(u_{max}^\zeta - u_{min}^\zeta)\cos\phi = A\cos\phi \tag{4.14}$$

is found to induce all the lower horizontal layers of fluid to move back and forth, due to the viscous effects, with a velocity distribution (Nielsen, 1992):

$$u_{\mathrm{w}}(z) = A \cos \phi - A \exp\left(-\left(\frac{z}{\delta}\right)^p\right)\cos\left(\left(\frac{z}{\delta}\right)^p - \phi\right) \qquad (4.15)$$

in which $\delta = \sqrt{2\nu/\omega}$ is the so-called Stokes length, ν the kinetic viscosity, ω the oscillating circular frequency, A the amplitude, p a constant which is 1 for laminar flow and may be 1/3 for turbulent flow, whereas the phase ϕ is unknown but should satisfy

$$U_{\mathrm{w}} = \frac{1}{h}\int_0^h u_{\mathrm{w}}(z)\mathrm{d}z \qquad (4.16)$$

where

$$U_{\mathrm{w}} = U - U_{\mathrm{c}} \qquad (4.17)$$

and

$$U_{\mathrm{c}} = \frac{u_{\mathrm{c}}^{\zeta}}{1 + \dfrac{n\sqrt{g}}{\kappa h^{1/6}}} \qquad (4.18)$$

which is obtained by solving Eqs. (4.11) and (4.12) simultaneously. Integrating Eq. (4.16), with $u_{\mathrm{w}}(z)$ substituted by Eq. (4.15), we have

$$U_{\mathrm{w}} = \sqrt{(A + \alpha)^2 + \beta^2}\sin(\phi + \psi) \qquad (4.19)$$

Hence,

$$\phi = \arcsin\frac{U_{\mathrm{w}}}{\sqrt{(A + \alpha)^2 + \beta^2}} - \psi \qquad (4.20)$$

in which $\psi = \arctan((A + \alpha)/\beta)$, and

$$\alpha = \frac{A\delta}{2ph}\{e^{-q}(q + 1)[(q - 1)\cos q - (q + 1)\sin q] + 1\}, \qquad (4.21)$$

$$\beta = \frac{A\delta}{2ph}\{e^{-q}(q + 1)[(q + 1)\cos q + (q - 1)\sin q] - 1\}, \qquad (4.22)$$

where $q = (h/\delta)^p$. In summary, we now have established a relation between $u(z)$ and U by means of Eqs. (4.13), (4.15), (4.18) and (4.19) and also $w(z)$, in association with the interaction between runoff and tide.

b. *Sediment Flocculation due to Salinity*

Sediment particles in estuaries are generally very fine. For instance, the mean diameter of the suspended particles is 0.0086 mm in the Yangtze River Estuary. A group of fine particles of this kind tends to flocculate through physical and chemical processes at the particle surface. According to Chien and Wan (1986), particles smaller than 0.01 mm in diameter display a conspicuous flocculation effect. The finer the particles, the stronger the physical and chemical effects and hence the more easily flocculation would occur. Once sediment flocculates, the particles settle down in groups rather than individually. Thus, the settling velocity, which is dependent on the grain diameter for an individual particle, may substantially increase by thousands of times. In salty turbid water environment, sediment concentration and salinity in sea water are important factors that can prompt sediment to flocculate. Figure 2 (Chien and Wan, 1986) shows that the settling velocity increases abruptly with salinity in sea water when salinity is within a certain range, which is also dependent on the sediment concentration. Therefore, mixing process in estuary is bound to exert crucial impact on sediment transport there.

Generally speaking, there are three types of mixing processes corresponding to different kinds of estuaries: sharply stratified estuaries or salt-wedge estuaries, partially stratified estuaries, and well-mixed estuaries. Quantitatively, they are
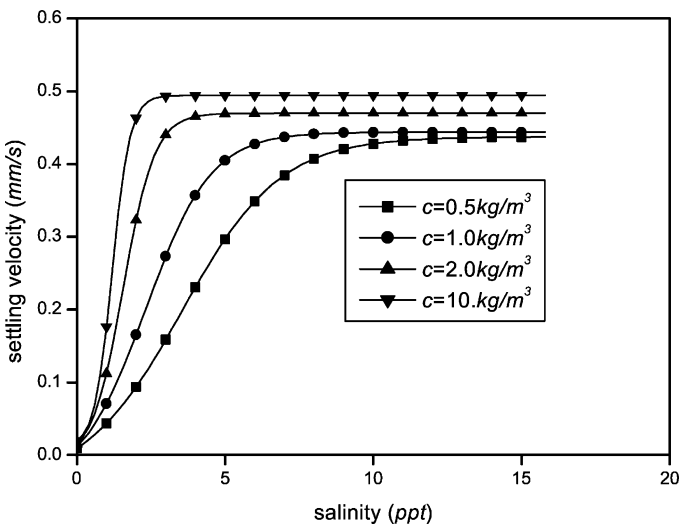

FIG. 2.   Variation of settling velocity with salinity at different sediment concentration (Chien and Wan, 1986).

classified by the mixing index N, defined as the ratio of runoff volume to flood volume within one tidal cycle. Conventionally, we have the following criteria:

$$N \geq 0.7 \qquad \text{sharply stratified}$$

$$0.1 \leq N < 0.7 \quad \text{partially stratified}$$

$$N < 0.1 \qquad \text{well mixed}$$

In a sharply stratified estuary, runoff discharge as compared to the tidal range is so large that fresh water runs seawards along the upper layer and salt water intrudes upstream from the lower layer. Mixing only takes place in the neighborhood of the interface between the two layers by turbulent entrainment. In regard to the quite extensive literature on this subject, the studies have mainly focused on the interfacial mixing mechanism and dependence of location and geometry of the arrested salt-wedge on runoff and tidal discharge (Grubert, 1989, 1990; Kurup *et al.*, 1998). In contrast, the runoff discharge as compared to tidal range is rather small in well-mixed estuaries, hence the tidal force can potentially produce strong turbulence, resulting in a vertically uniform salinity profile. The dynamic process can be examined by depth-integrated models. As for the partially stratified estuary, such as the Yangtze River Estuary, the mixing index, being 0.18 on average, varies with seasons and the salinity distribution displays distinct three-dimensional characteristics. To describe this kind of mixing process, it is indispensable to have a better understanding of vertical structure of estuarine flows.

c. *Resuspension in Turbulent Flows*

The mechanism of sediment resuspension in turbulent flows is a challenging problem. It is essential to specify a well-founded resuspension flux formulation in sediment transport modeling with the flux directly serving as the bottom condition in a vertical two-dimensional or three-dimensional numerical model. At the same time, this flux is implicitly represented in the source term in a depth-averaged two-dimensional model.

The mechanism of sediment resuspension has been explored for several decades. The intermittence of sediment inception has provided a resemblance to turbulence. Early in the 1960s, Sutherland (1967) put forward an idea that a mechanism to entrain sediment grains into suspension would correspond to flow ejections associated with coherent structures in the near-bed region of a turbulent boundary layer. This idea has been verified more recently by empirical evidence. In fact, the sediment-laden boils observed at the free surface of rivers exhibit the effects of burst events on sediment transport in alluvial channels (Jackson, 1976). Also, different indoor experiments have been conducted to examine

the entrainment mechanism of particles into suspension. Particularly, Nino and Garcia (1996) studied particle–turbulence interactions in near-wall region with natural sediment particles and proved the strong dependence of sediment inception and entrainment on turbulent bursting events. This led them to draw the following conclusions. Sediment particles tend to accumulate in the low-speed regions and form wall streaks accompanied by the presence of counter-rotating quasi-streamwise vortices. The wall streaks extend about 1000–2000 wall units in the streamwise direction, and have a transverse wavelength of about 100 wall units. Particles are picked up from the bed by flow ejection events occurring downstream of the shear layers, and particle ejection angles are in the range 10–20°, very similar to the angle of inclination of the shear layers, typically being 14°. The number of particles reaching the outer regions of the wall layer increases with the dimensionless bed shear stress. Particles would be only rarely deposited by the action of sweep events, but rather they appear to be falling back toward the bed as they lose correlation with the turbulent structures that lifted them from the bed and kept them in suspension for some time. These studies, however, delineate only qualitatively that the mechanism of turbulent bursting is supposed to be responsible for sediment inception and suspension.

More recently, Cao (1997) has established a quantitative formula for sediment entrainment flux based on the turbulent bursting mechanism. His formula relates the flux to the temporal and spatial scales of bursting events so as to take the form:

$$E_n = PC_0 \sqrt{\frac{S}{g}} d \left(\frac{\tau'}{\tau_c} - 1 \right) \frac{\tau'}{\rho_s - \rho} \qquad (4.23)$$

in which C_0 is the volumetric concentration of bed material, $P = \lambda \sqrt{Sg}/\nu T_B^+$, $\lambda \approx 0.02$ the averaged area of all bursts per unit bed area, $T_B^+ \approx 100$ the non-dimensional bursting period, $S = (\rho_s - \rho)/\rho$, ρ_s the sediment density, d the diameter of sediment grain, τ_c the critical incipient stress, and τ' the skin friction of bed shear stress.

In estuaries, the bulk density of bed material is usually smaller when fine particles start to settle down. It then gradually grows with time due to a compact process, during which the incipient condition alters with bed mixture's bulk density. To take this factor into account, we introduce Tang–Cunben's formula (Tang, 1963)

$$\tau_c = \frac{1}{77.5} \left[3.2(\gamma_s - \gamma)d + \left(\frac{\gamma_b}{\gamma_{b0}} \right)^{10} \frac{k}{d} \right] \qquad (4.24)$$

where $\gamma = \rho g$; $\gamma_s = \rho_s g$; $\gamma_{b0} = 1.6$ g/cm^3 is the bulk density of compact bed material; $k = 2.9 \times 10^{-4}$ g/cm; γ_b is the bulk density of bed material, which is not a constant but varies with tidal phase.

2. *Model and its Validation*

For long and narrow estuaries, a vertical two-dimensional model is applicable. Here, we are ready to propose a quasi-two-dimensional vertical model instead of the conventional one. This model computes vertical two-dimensional flow by profiling one-dimensional current obtained from the Saint Venant Equations via the vertical structure of estuarine flow as discussed in Section IV.A.1.a. Therefore, the model is advantageous in requiring less CPU time and affording more apparent physical implications. In addition, it can be easily extended to three-dimensional circumstances (Zhou and Li, 1999; Zhou and Li, 2000).

a. *Governing Equations*

The one-dimensional continuum and momentum equations for shallow water are

$$\frac{\partial \zeta}{\partial t} + \frac{\partial Uh}{\partial x} = 0, \tag{4.25}$$

$$\frac{\partial U}{\partial t} + U\frac{\partial U}{\partial x} = -g\frac{\partial \zeta}{\partial x} - \frac{gh}{\rho}\frac{\partial \bar{\rho}}{\partial x} - g\frac{|U|U}{C^2 h}, \tag{4.26}$$

where t is the time; x, z the horizontal (seawards) and the vertical (upwards) coordinates, respectively; ζ the water level; h the depth; U the vertical mean velocity; g the gravitational acceleration; C the Chezy coefficient; and $\bar{\rho}$ the depth-averaged value of salt water density ρ, which is defined by the state equation:

$$\rho = \rho_0 + \eta s, \tag{4.27}$$

in which ρ_0 is the density of fresh water; s the salinity; η a constant, which approximates to 0.0007 provided s is measured in parts per thousand (ppt). To further derive the vertical velocity component, we introduce the vertical two-dimensional continuity equation

$$\frac{\partial u}{\partial x} + \frac{\partial w}{\partial z} = 0, \tag{4.28}$$

where u and w, respectively, denote the x- and z-component of the flow velocity. Then, the salinity and sediment concentration can be obtained via the respective vertical two-dimensional advection–diffusion equation:

$$\frac{\partial s}{\partial t} + \frac{\partial us}{\partial x} + \frac{\partial ws}{\partial z} = \frac{\partial}{\partial x}\left(D_x\frac{\partial s}{\partial x}\right) + \frac{\partial}{\partial z}\left(D_z\frac{\partial s}{\partial z}\right), \tag{4.29}$$

$$\frac{\partial c}{\partial t} + \frac{\partial uc}{\partial x} + \frac{\partial (w - \omega_f)c}{\partial z} = \frac{\partial}{\partial x}\left(N_x\frac{\partial c}{\partial x}\right) + \frac{\partial}{\partial z}\left(N_z\frac{\partial c}{\partial z}\right). \tag{4.30}$$

in which c is the sediment concentration; ω_f the settling velocity of flocculated sediment particles, D_x and D_z the horizontal and vertical turbulent diffusivities for salinity, N_x and N_z horizontal and vertical turbulent diffusivities for sediment.

It should be mentioned that the main point in solving Eq. (4.30) is how to specify the bed boundary condition more reasonably. As we have argued in the previous paragraph, an entrainment function E_n is used for bottom sediment flux, i.e.,

$$-N_z \frac{\partial c}{\partial z} = E_n, \tag{4.31}$$

where E_n is a function of either incipient velocity or incipient stress. For unsteady sediment transport, incipient stress is preferred. Here, we adopt the turbulent bursting-based formula as cited in Section IV.A.1.c.

b. *Solution Methods and Procedures*

The methods and steps to solve the foregoing equations are as follows. First, we solve Eqs. (4.25)–(4.27) simultaneously, yielding the time series of mean speed U and water level ζ in a tidal cycle. Resorting to the theory we have proposed, $u(z)$ is obtained via Eqs. (4.3), (4.4), (4.13), (4.15) and (4.17)–(4.20). Then, $w(z)$ is directly derived by continuity equation (4.28). And the patterns in salinity and sediment concentration are ultimately produced by integrating the advection–diffusion equations (4.29) and (4.30) in sequence. In order to solve Eqs. (4.25) and (4.26) numerically, we choose the Preissmann implicit finite difference scheme, which is advantageous in its stable nature and less CPU time demand. Equations (4.29) and (4.30) are discretized by an up-wind difference scheme and the alternative direction implicit (ADI) method. However, iterations are always necessary due to the s being unknown in the state equation.

c. *Validation of the Model*

Observational database in the North Channel waterway of the Yangtze River Estuary is used for the model validation. Hourly tide levels were acquired on September 3–5, 1989 at four gauging stations at Hengsha, Middle of North Channel, 18 km downstream of Hengsha, and at Jiuduandong, 40 km downstream of Hengsha (see Fig. 1). The salinity, sediment concentration and horizontal velocities were measured at SN2, SN3 and SN4, 8, 12 and 16 km downstream of Hengsha station, respectively. Taking Hengsha station as the upstream boundary and Jiuduandong as the downstream boundary, the simulated spatial domain is meshed by 20 grids with horizontal step $\Delta x = 2$ km and vertically divided into 10 layers. The time step for temporal integration from 6:00 a.m. on Sep. 4 to 6:00 a.m. on Sep. 5 is $\Delta t = 60$ s. The roughness coefficient is

assumed to be $n = 0.01$. With $\zeta(x,0) = 0$ and $U(x,z,0) = 0$ as the initial conditions, the simulated time series of water level at the Middle of North Channel station is compared very well with the measurement as shown in Fig. 3 (Zhou and Li, 2000). The calculated flow field in the vertical plane around HWR and LWR is shown in Fig. 4 (Zhou and Li, 2000), demonstrating that the horizontal velocity component is much greater than the vertical one. Comparing the simulated horizontal velocity component with the corresponding data in-situ in Fig. 5, we find that the calculated flow field represents the real patterns of estuarine flows approximately.

For the sake of validating the salinity and sediment concentration prediction, the downstream boundary is replaced by that at SN4 owing to lack of salinity and sediment concentration data at Jiuduandong station. The water level at SN4 obtained from the computation for water level validation is taken as the boundary conditions. The salinity at Hengsha as the upstream boundary can be assumed to be zero because the Hengsha station is situated approximately at the limit section which divides salty and fresh water (Wang *et al.*, 1995). According to Kuang (1993), the horizontal diffusivity assumes the value $N_x = D_x = 500 \text{ m}^2/\text{s}$, and the vertical diffusivity has the form

$$N_z = D_z = \begin{cases} \kappa u_* z \left(1 - \dfrac{z}{h}\right), & z/h < 0.5, \\ \kappa u_* h, & z/h \geq 0.5. \end{cases} \tag{4.32}$$
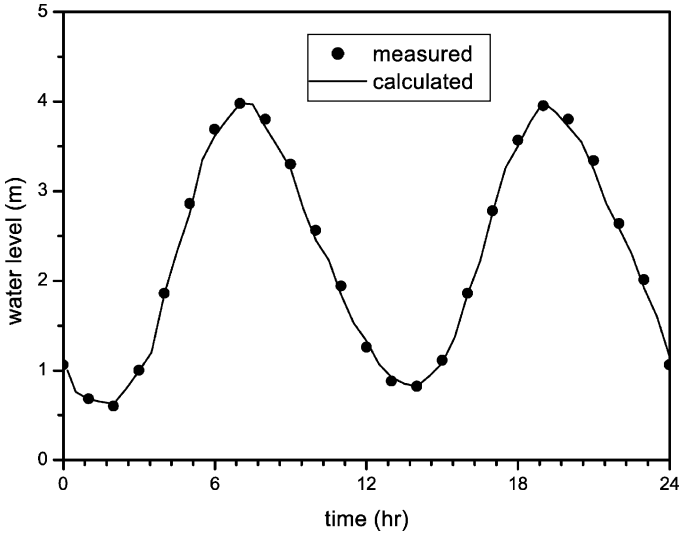
FIG. 3. The water level at the Middle of North Channel station. The time duration is from 6:00 a.m. (corresponding to $t = 0$ h) on Sep. 4 to 6:00 a.m. (corresponding to $t = 24$ h) on Sep. 5, 1989.
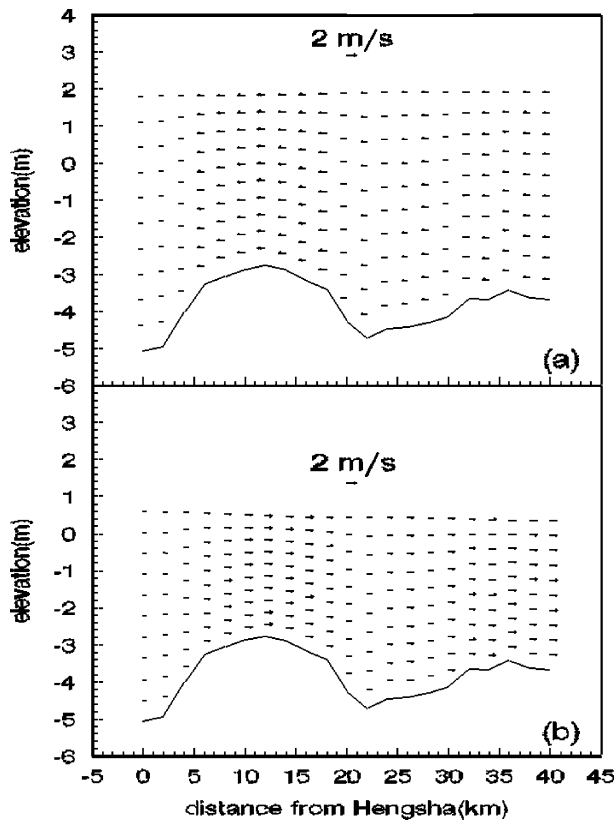
FIG. 4. The simulated flow vector field. The solid line is the bed profile. (a) Around high water rapid (HWR); (b) around low water rapid (LWR).

Here u_* is the friction velocity of the mean flow. Transition from the initial salinity field $s(x, z, 0) = 0$ to a stable state takes a few tidal cycles. Figures 5–7 (Zhou and Li, 2000; Zhou *et al.*, 1999a) present some comparison of the calculated time series of velocity, salinity and sediment concentration at the site of SN3 with the measured ones at six different heights of $1.0h$, $0.8h$, $0.6h$, $0.4h$, $0.2h$ and $0.0h$. The agreements are satisfactory, i.e., well within permitted errors for engineering practice.

3. *Variation of Salinity*

Generally speaking, mixing processes of sea water in estuaries are very complicated due to the interactions of different dynamic factors and irregular
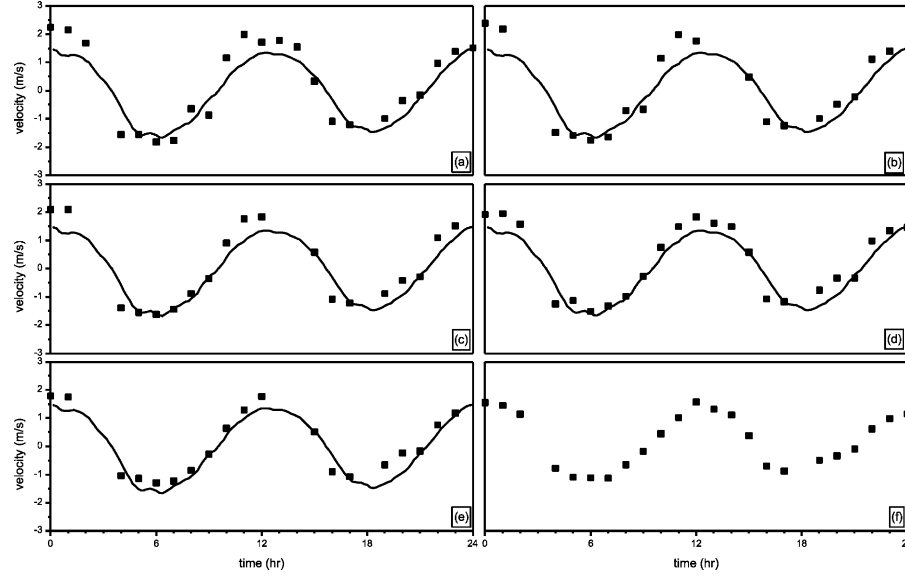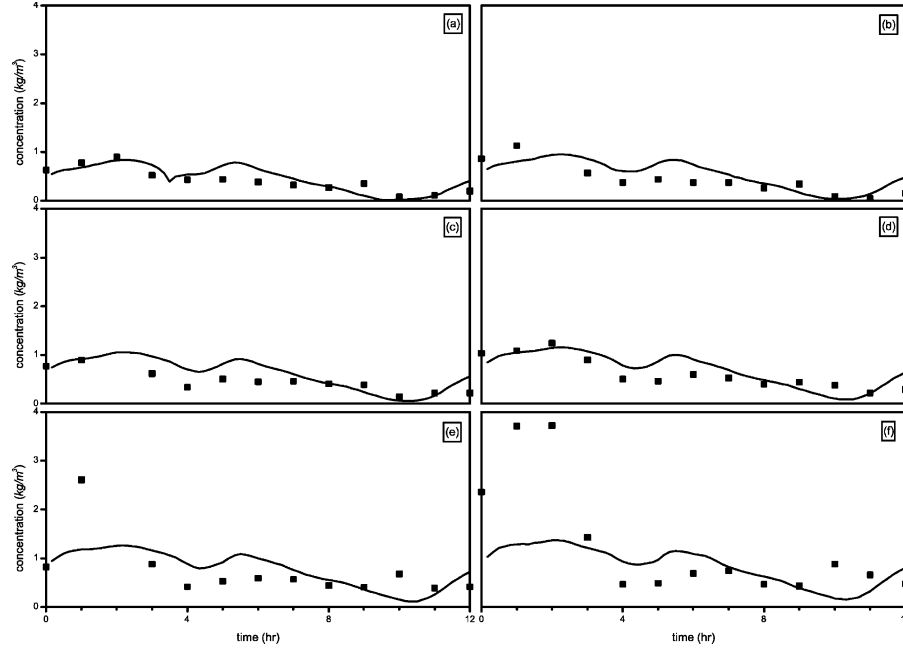
FIG. 5. Comparison of the calculated (line) and observed (dots) velocity time series. The time duration is from 6:00 a.m. (corresponding to $t = 0$ h) on Sep. 4 to 6:00 a.m. (corresponding to $t = 24$ h) on Sep. 5, 1989.
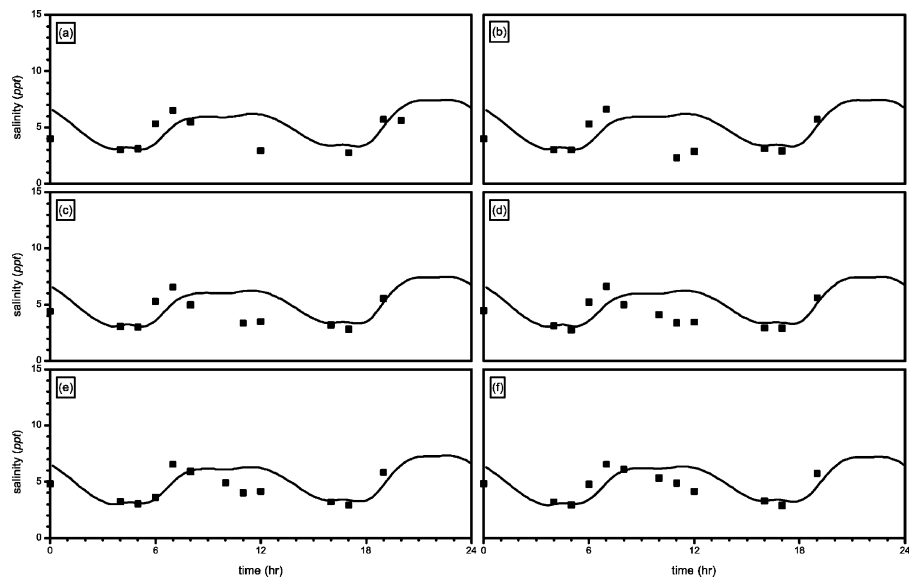
FIG. 6. Comparison of the calculated (line) and observed (dots) salinity time series. The time duration is from 6:00 a.m. (corresponding to $t = 0$ h) on Sep. 4 to 6:00 a.m. (corresponding to $t = 24$ h) on Sep. 5, 1989 (reproduced from Zhou *et al.* (1999a) with permission by Scientia Sinica).

FIG. 7. Comparison of the calculated (line) and observed (dots) sediment concentration time series. The time duration is from 6:00 a.m. (corresponding to $t = 0$ h) to 6:00 p.m. (corresponding to $t = 12$ h) on Sep. 4, 1989.

TABLE IV
CASES FOR STUDYING SALINITY AND SEDIMENT CONCENTRATION

Case label	Presumed conditions		Calculated results	
	te (m)	uc (m/s)	N	$\Delta s/\Delta x$ (km^{-1})
a	2.0	0.1	0.13	0.48
b	1.0	0.1	0.18	0.61
c	0.5	0.1	0.22	0.69
d	0.5	0.2	0.40	1.09
e	0.5	0.3	0.57	1.50

topography. For simplicity, a plane bottom is assumed to facilitate analyzing the influences of runoff and tides on the mixing processes. The adopted parameters are referred to those of the North Channel waterway of the Yangtze River Estuary. For example, the depth is taken as 10 m below theoretical datum plane. The hydrological factors are listed in Table IV.

In this table, te denotes the amplitude of tide level, half of the tidal range, uc stands for the runoff component of velocity at the upstream boundary, and N is the mixing index, expressing the relative strength of runoff and tides.

a. *Longitudinal Distribution of Mean Salinity*

Some representative variations of salinity with runoff and tides have been obtained by case studies (see Fig. 8). Comparisons of cases *a*, *b*, *c* and of cases *c*, *d*, *e* reveal the variations of salinity with tides and runoff, respectively. Figure 8 suggests that the longitudinal mean salinity distribution is dependent on tidal range, phase angle and runoff discharge. The gradient reaches its smallest for the most upstream sea water intrusion at HWS and its greatest for the most downstream sea water intrusion at LWS, and it is between these two values at all the other moments. At a given phase, the gradient decreases with increasing tidal range or hydrodynamic tidal force, if runoff discharge remains unchanged. When te = 2.0 m, uc = 0.1 m/s, the longitudinal salinity profile is approximately linear. If tidal range remains the same, an increase in the runoff discharge results in a large salinity gradient, with the longitudinal profile deviating from a linear one. In fact, we may as well introduce a single variable, namely the mixing index, to explain the variation of longitudinal salinity distribution at a given phase of the tides and runoff. For case *a* to *e*, the degree of mixing becomes gradually weaker with increasing mixing index Table IV while the salinity gradient grows correspondingly. When the index takes the value 0.13, the longitudinal salinity profile becomes approximately a linear one.
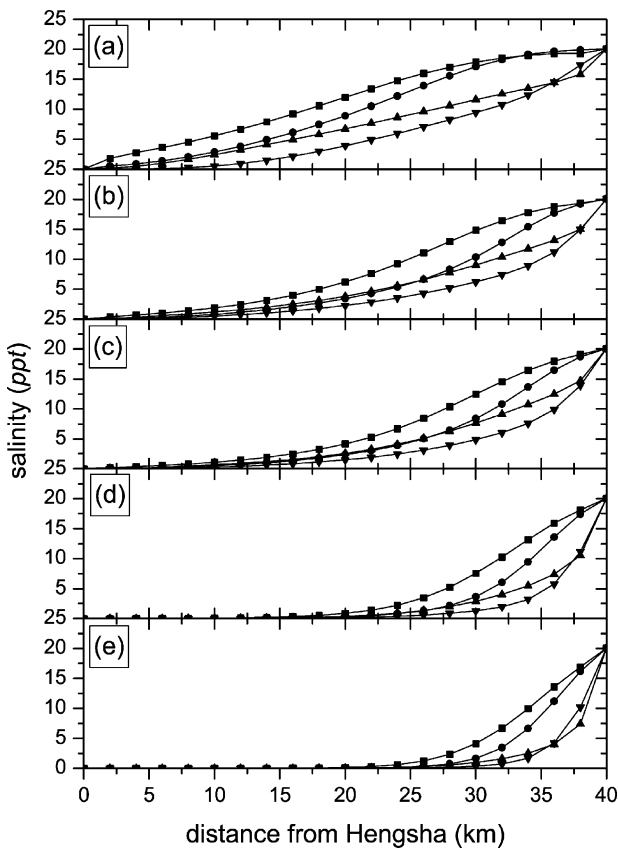
F<small>IG</small>. 8. Variation of the longitudinal distribution of the mean salinity with runoff and tides. Square: at HWS; Dot: at HWR; Upper-Triangle: LWR; Down-Triangle: LWS. (a) case *a*; (b) case *b*; (c) case *c*; (d) case *d*; (e) case *e* (reproduced from Zhou *et al.* (1999a) with permission by Scientia Sinica).

b. *Variations of the Salt Front*

The 'front' concept was early used in meteorology to represent an interface between two air masses with different temperatures. This concept has been introduced to oceanography to describe the interface between two water masses with different temperatures or densities at which the gradient of certain hydrological quantities (such as salinity, density, etc.) is large. Nearby the front, the salinity favors flocculation of sediment particles, and the circulation caused by density difference tends to capture the suspended sediment. All these effects result in the formation of 'turbidity maximum' in a certain zone of estuary.

The salt front intensity can be quantified by the longitudinal salinity gradient $\Delta s/\Delta x$. In Table IV, a list of the mean salt front intensities at HWS and LWS is given. The figures in the table show that $\Delta s/\Delta x$ increases with N, namely, the salt front for weakly mixing case becomes more intense with runoff discharge increasing or tidal range decreasing. Thus, it can be inferred that the salt front intensity in flood seasons is greater than that in dry seasons. On the other hand, the salt front intensity during ebbing is greater than that during flooding of tide, owing to the seaward movement of the salt front forced by runoff on ebb and the upstream movement of the salt front forced by tide on flood. These statements are demonstrated in Fig. 8 (Zhou *et al.*, 1999a). Figure 9 (Zhou *et al.*, 1999a) plots in $\Delta s/\Delta x$ against N, approximately exhibiting a linear increase in salt front intensities with mixing indices, with different slopes at different phases. The slope turns from its minimum at HWS to its maximum at LWS.

Field measurements indicate that a salt front with the greatest longitudinal salinity gradient exists in an estuary all the year round. Its intensity and position are phase-, runoff- and tide-dependent. This is implied by the data in Fig. 8. At the HWS instant, the greatest salinity gradients of cases *a*, *b*, *c*, *d* and *e* are 0.70, 0.94, 1.00, 1.37 and 1.78 km^{-1}, respectively. The fronts are located at some 20, 25, 28, 32 and 36 km downstream from the Hengsha station, with the position displacement reaching 16 km approximately.
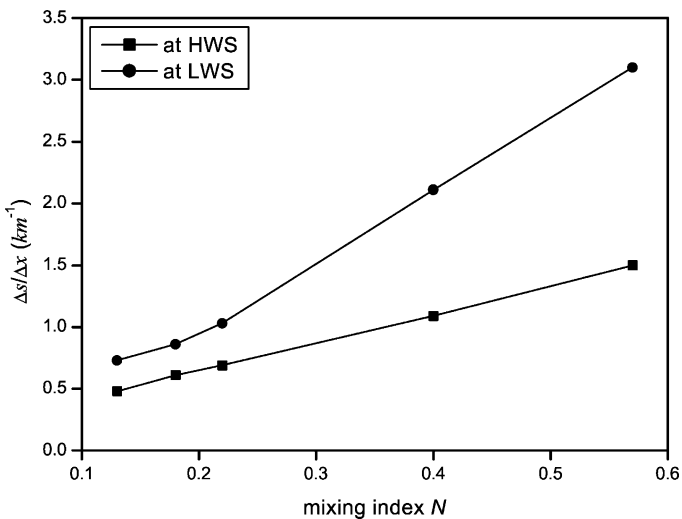

FIG. 9. Relationship of salt front intensity and mixing index (reproduced from Zhou *et al.* (1999a) with permission by Scientia Sinica).

c. *Salinity Distributions in the Vertical Plane*

Salinity contours in the vertical plane (see Fig. 10, Zhou *et al.*, 1999a) describe the patterns of salinity distribution both in the longitudinal and vertical directions, exhibiting different characteristics related to different combinations of the hydrological factors involved, including certain periodic variations for a given combination of hydrological factors. In Fig. 10(a)–(d) are plotted the contours of case *b* (te = 1.0 m, uc = 0.1 m/s) at slack water and rapid water phases, which once again depict the characteristics of the longitudinal mean salinity distribution shown in Fig. 8, e.g., the salt front intruding the most upstream at HWS under the tide effects, and being pushed seawards to the most downstream end at LWS by the runoff force. In addition, a rudimentary salt-wedge is seen from the figures as a result of the density flow. On the other hand, in the vicinity of the upstream end, which may lie beyond the uppermost reach by the sea water, and the downstream end, where there is little fresh water, the salinity distributes uniformly in the vertical direction. Therefore, the vertical salinity gradient experiences a small-to-large-to-small variation, suggesting uniform vertical salinity profiles at the two ends and non-uniform ones in the intermediate range.

Figure 10(d)–(f) shows of the salinity contours for different tidal ranges, 0.5, 1.0 and 2.0 m, with the same runoff discharge. It can be seen that the salt front approaches more upstream with increasing tidal force when runoff discharge remains unchanged, with a 5-km shift of the front locations. Likewise, a comparison of the salinity contours for different uc values, 0.1, 0.2 and 0.3 m/s with a given tidal range, is made between Fig. 10(f)–(h), suggesting that an increase of runoff discharge constrains the upstream intrusion of the salt water and makes the salt front move seawards, with a 15 km shift of the front. Therefore, effects of runoff and tides make the salt front oscillate downstream and upstream, respectively, with the former effect being more apparent.

4. *Turbidity Maximum Zone*

The turbidity maximum zone, in which the sediment concentration is relatively higher, is a natural phenomenon almost found in every estuary. Studies on ecological environment in estuaries have shown that the turbidity maximum plays an important role in the growth of phytoplankton and zooplankton (Gu *et al.*, 1995; Xu *et al.*, 1995). In the turbidity maximum, suspended sediment reduces the light transmittance of water, affecting the photosynthesis and, hence, the chlorophyll content of water. In addition, the content and distribution
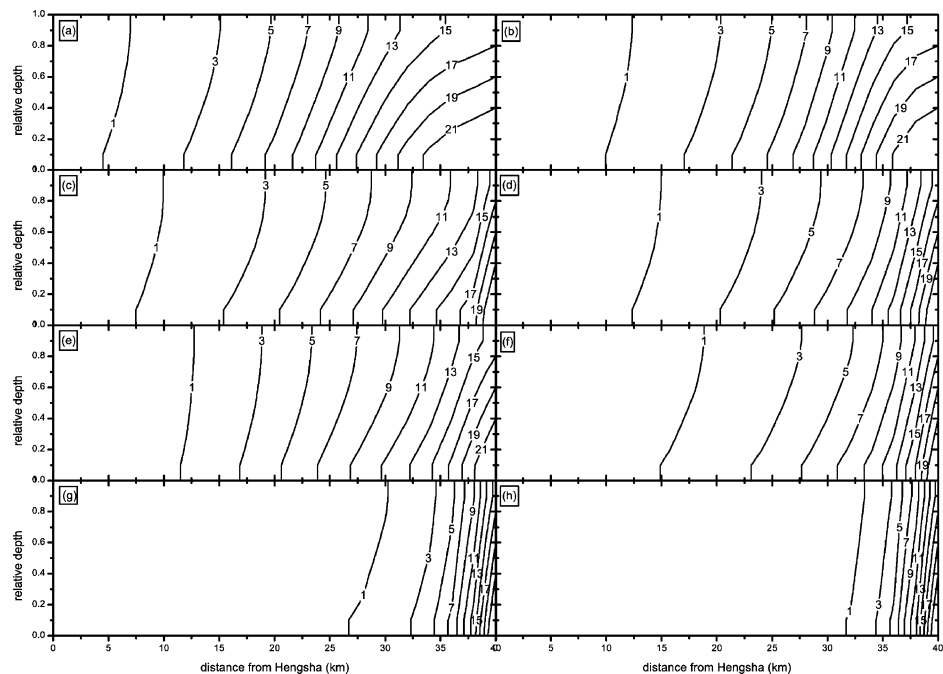
FIG. 10.   Variations of salinity contours with time, runoff and tides. (a) Case *b* at HWS; (b) case *b* at HWR; (c) case *b* at LWR; (d) case *b* at LWS; (e) case *a* at LWS; (f) case *c* at LWS; (g) case *d* at LWS; (h) case *e* at LWS (reproduced from Zhou *et al.* (1999a) with permission by Scientia Sinica).

of nutrient substances are bound to change with sediment transport due to the strong adsorption capacity of sediment particles to the nutritious salt and heavy metal elements (Shen and Shi, 1999). It is also of significance to study turbidity maximum in order to elucidate the formation of the mouth bar. We have examined the variation of sediment concentration with runoff and tides by case studies as discussed in the foregoing section, aiming at revealing the mechanism why turbidity maximum occurs.

Figure 11 (Zhou and Li, 2000) shows distributions of concentration around high slack water phase. A common characteristic can be found in each case: a high concentration zone exists in the middle of the simulated domain. As a matter of fact, vertical sediment transport can be accounted for by the balance of resuspension and settling. The former depends on the interaction of bed and current, and the latter represents the effect of salinity. In the upstream domain, resuspension is dominant due to slow settling of sediment grains. This causes the concentration to increase. With increasing salinity downstream, the settling velocity ω_f increases correspondingly. At the same time, the mean flow velocity is reduced. Therefore, the settling effect becomes the dominant one, resulting in a decrease in the sediment concentration. In this low-to-high-to-low process of concentration, a midway high concentration zone exists naturally. This special zone is generally called 'turbidity maximum'. It is around this area that a mouth bar forms easily.

Figure 11 also shows the variation of turbidity maximum position with the relative strength of runoff and tides. From case b to e, the mixing index, N, changes from small to large. Correspondingly, the turbidity maximum shifts from upstream to a downstream area. This is simply because the smaller the N, the stronger the tides, the farther the sea water intrudes upstream. Meanwhile, the salt water mixes with the fresh water more uniformly. As a result, ω_f increases immediately along the whole water column, and the concentration decreases.

Secondly, our calculated results indicate that the concentration distribution is phase dependent. The turbidity maximum position varies in a tidal cycle. It is most upstream at HWS and most downstream at LWS, shifting 8 km or so. This is also attributed to the non-uniform salinity distribution. With the upstream intrusion of flood tides, salinity increases and then ω_f increases as well due to the flocculation effect. Hence, the turbidity maximum moves upstream till HWS. On the contrary, it moves seawards till LWS. It seems that the shifting distance within one tidal cycle is independent of the mixing index N. But the averaged position within a tidal cycle varies with N. The larger the N, the more downstream the turbidity maximum locates. The maximal shifting distance of mean position of the turbidity maximum approximates to 20 km.
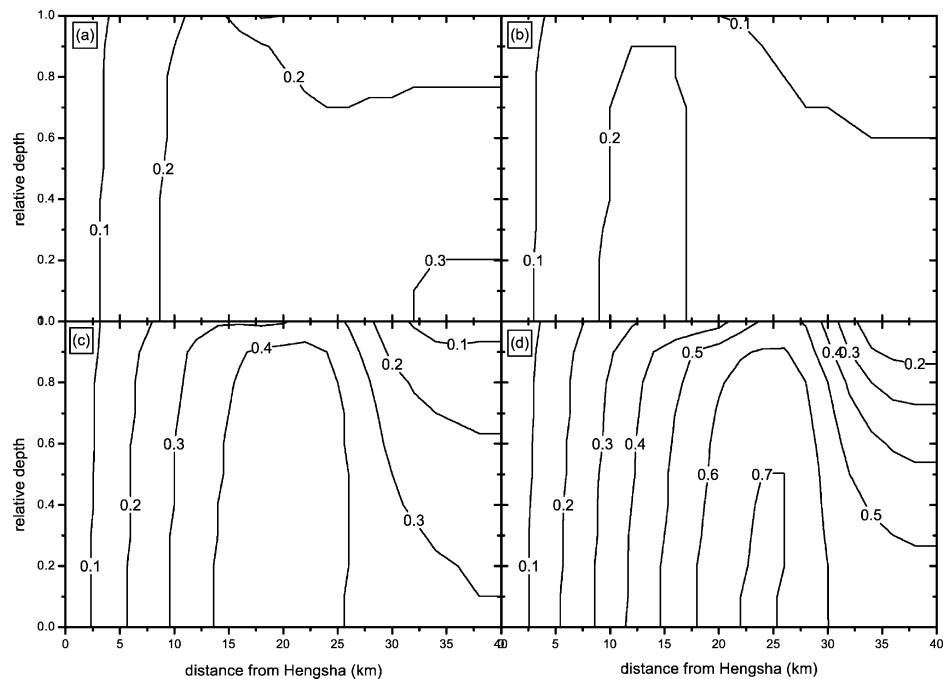
FIG. 11.   Contours of sediment concentration corresponding to different mixing indices. (a) Case *b* at HWS; (b) case *c* at HWS; (c) case *d* at HWS; (d) case *e* at HWS.
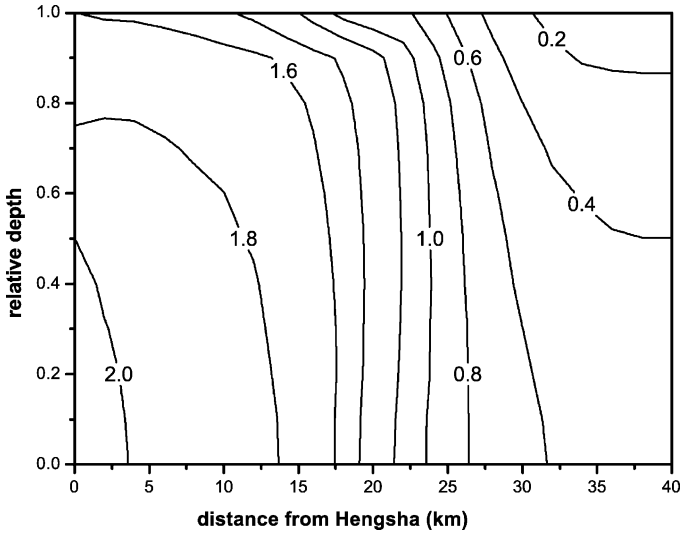
FIG. 12. Sediment concentration contours of case d at HWS ($\bar{c}_e = 2.0$ kg/m^3). The turbidity maximum feature is not noticeable if the sediment concentration at the entrance is large enough.

Finally, the concentration distribution is also adjusted by the entrance sediment condition even if the hydraulic factors remain the same. Figure 12 (Zhou and Li, 2000) displays some concentration contours of case d when $\bar{c}_e$, the depth-averaged sediment concentration at the entrance, is equal to 2.0 kg/m^3. It is found that the concentration decreases seawards while variations of the turbidity maximum features are not noticeable. In this case, suspended load q_s continues to decrease seawards (see Fig. 13, Zhou and Li, 2000, dq_s/dx is always negative) owing to the dominant settling effect over resuspension, and hence deposition occurs everywhere. When $\bar{c}_e$ is small, dq_s/dx changes from positive to negative, suggesting that erosion occurs upstream followed by downstream deposition.

B. RUNOFF GENERATION AND SOIL EROSION ON THE LOESS PLATEAU

The Loess Plateau in the central China with an area of 430,000 km^2 is noted for its ancient culture and serious water and soil loss. About 287,600 m^2 of area in this region has an annual erosion rate greater than 1000 ton/km^2. Moreover, the eroded soil totally amounts to more than 2.2×10^9 tons, among which about 1.6×10^9 ton, on average, is delivered into the Yellow River, rendering the river one of the highest sediment-laden
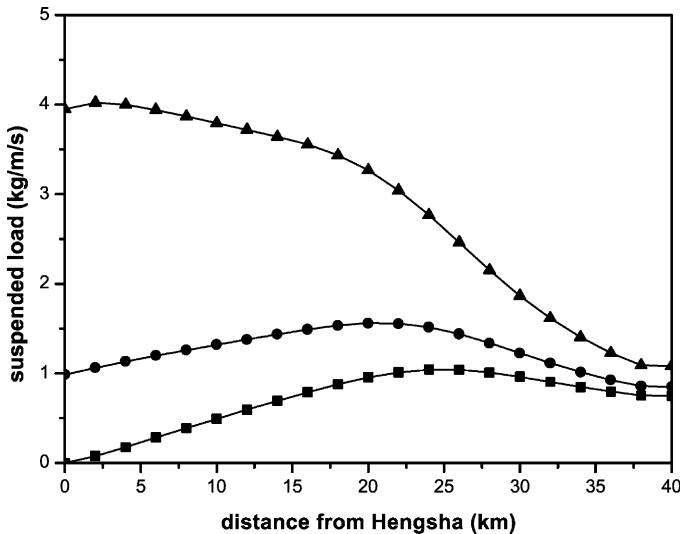
Fig. 13. Influence of sediment supply at the entrance on the curve of suspended load vs distance. Square: $\bar{c}_e = 0.0$ kg/m^3; dot: $\bar{c}_e = 0.5$ kg/m^3; upper-triangle: $\bar{c}_e = 2.0$ kg/m^3.

rivers in the world. The serious soil erosion of long period leads to the fragment geomorphy in this region. Especially, the recent violent human activities considerably aggravate the situation and have brought about a series of consequences such as lean soil, desert land formation, arable land diminish and production reduction. The eroded soil input into the Yellow River and carried downstream to block water channel is responsible for frequent flooding disasters in the middle and lower reaches. Furthermore, the sediment with adsorbed toxic elements from pesticide and fertilizer in the cultivated land may cause water pollution by concentration effect. Therefore, it is an urgent and challenging task to prevent ecological environment deterioration in Western China due to soil erosion.

During the recent decades, there have been extensive investigations on soil erosion in the Loess plateau area. A general qualitative description of this issue such as erosion type, erosion intensity, erosion geomorphy and their regional distribution has been acquired. Many empirical and semi-empirical relationships have been established to estimate runoff and soil erosion quantitatively. However, most of the previous researches aiming at a certain specific erosion type or region only covered very limited parameter range. As a matter of fact, surface feature, topography and soil characteristics of the Loess Plateau along with rainfall conditions are substantially varied in different regions. The research

in a specific region without quantitative comparison and mechanism exploration is unable to reflect overall roles of various factors in the process of erosion. Accordingly, the research of soil erosion at present tends to shift from the empirical approach to the process-based dynamic description such as WEPP in USA and ANSWERS in Europe. In recent years, some process-based models are also developed in China (Chen *et al*., 1996; Qi and Huang, 1997). Tang and Chen (1997) have ever presented a more theoretical model for predicting transportation capacity of overland flows. But comparatively, the dynamic study of erosion process on the Loess Plateau is relatively weak. The present investigation is mainly concerned with the physical mechanism of overland flows and soil erosion on the Loess Plateau. Since the water erosion caused by rainfall is a rather complicated process affected by both water and soil interactively, three research methods including theoretical analysis, laboratory experiment and mathematical model were used in the research. As a first step, the objective of the current research therefore is to examine the fundamental laws of overland flows, runoff generation and rill erosion in several typical regions on the Loess Plateau, which will certainly be helpful for gaining an insight into these processes on the Loess Plateau in the Northwest China.

1. *Formation of Runoff on the Slope*

Hillslope runoff erosion is such a process that sheet flow generated during rainfall scours the soil surface. The water flow produces eroding force and plays an active role in the whole process. It is of primary importance to first understand the runoff generation characteristics. The motive power led to erosion is the acting force of surface flow, while the erosion-resisting capacity is dependent on the stability of soil body. That is to say, the soil loss on the hillslope occurs when the scouring capability of surface runoff exceeds the erosion-resisting capacity. The whole process can be divided into three stages. Firstly, when the rainfall intensity is greater than the soil infiltration rate and the surface ponding capability, the excess rain flows down the hillslope under the action of gravity and thus forms the surface sheet flow. Then, when the scouring ability is greater than the erosion-resisting capacity of soil, the scour of soil particles is initiated. And finally, the scoured soil is transported downstream by overland flow. Therefore, the soil erosion is mostly dependent on the overland flow caused by rainfall. To sum up, when the rainfall intensity exceeds soil infiltration rate, water begins to accumulate in the depressed pool or vacancy. It is not until beyond the surface ponding ability that water flows down the slope under the action

of gravity and form sheet flow. That is just the beginning of runoff generation. Obviously, precipitation, infiltration and overland flow formation are the most fundamental hydrodynamic processes in soil erosion study.

a. *Precipitation on the Loess Plateau*

The Loess Plateau belongs to the semi-humid and semi-arid region, the annual precipitation is in the scope of 400–800 mm. The annual precipitation in whole Loess Plateau area, on average, is about 500 mm, and its seasonal distribution in a year is very non-uniform. More than 70% of precipitation occurs from July to September. Moreover, these rainfalls are mostly rainstorms with shorter duration and indefinite location. The precipitation of one storm is often more than 10% of total annual amount.

What is unique for the erosion on the Loess Plateau is that it always occurs during rainstorm. The rainfall number giving rise to apparent erosion does not exceed 10% of the total ones. On average, three rainfalls each year may cause serious erosion, only occupying about 4% of total rainfall number. As roughly estimated, 80% of the total erosion quantity is yielded in 1.3 times of rainfalls while 50% of the total erosion quantity in 0.6 times of rainfalls (Wang and Jiao, 1996). Thus we would rather lay emphasis on the erosion of the Loess Plateau under rainstorm conditions.

So far, there is still no standard rainfall frequency and intensity available in the Loess Plateau area. According to Wang and Jiaos (1996) research, the rainstorms in this region can be divided into three types: uniform rainstorm, a single-peak rainstorm and multi-peaks rainstorm. The single-peak rainstorm is assumed as a single-peak rain process of short duration with high peak, while multi-peaks rainstorm is assumed as multi-peaks rain process of long duration with relatively low peak in which one peak value is equal to three to five times of the others.

b. *Infiltration Process*

Soil infiltration is a precursory process for runoff formation. While its influencing factors include cumulative infiltration quantity, infiltration rate, saturate conductivity (or infiltration coefficient), saturate volumetric water content, i.e., efficient porosity, and initial volumetric water content, etc. So a reasonable description of soil infiltration process is considerably essential for overland flow modeling. The famous Green–Ampt model with explicit physical meaning was put forward in 1911, then the models of Horton (1940) and Philip (1957) in succession. So far the Green–Ampt model is still commonly used

owing to its simplicity and credible applications. In particular, the improvements by Mein and Larson and Chu have extended its applicability to the circumstances of both steady and unsteady rainfall. Although the Horton model is widely applied in China, the parameters involved do not bear apparent physical meaning as the Green–Ampt model. So we select the revised Green–Ampt model (Mein and Larson, 1973; Chu, 1978) to describe the soil infiltration process. The governing equations of soil infiltration may be written as:

$$i = \frac{dI}{dt} = K[1 + (\theta_s - \theta_i)S/I]$$

$$I = Kt - S(\theta_s - \theta_i)\ln\left(1 + \frac{I}{S(\theta_s - \theta_i)}\right)$$

(4.33)

where I is the cumulative infiltration quantity (m), i the infiltration rate (m/s), K the saturate conductivity of soil (or infiltration coefficient) (m/s), θ_s the saturate volumetric water content, i.e., the efficient porosity(%), θ_i the initial volumetric water content (%), and S the soil suction (m).

The classic Green–Ampt formula is merely applied to ponding water infiltration process on dry soil. Mein and Larson (1973) generalized it to the infiltration process during rainfall. Suppose p is the steady rainfall intensity. In initial stage of rainfall, all the rain infiltrates into soil. The moment when infiltration rate i equals p ponding occurs. The cumulative infiltration, I_p, may be derived by the Green–Ampt model:

$$I_p = \frac{(\theta_s - \theta_i)S}{p/K - 1},$$

(4.34)

from which the ponding moment

$$t_p = I_p/p$$

is yielded. Thus the infiltration rate in the whole process can be expressed as

$$\begin{aligned} i &= p & t \leq t_p \\ i &= K[1 + (\theta_s - \theta_i)S/I] & t > t_p \end{aligned},$$

(4.35)

where I is the cumulative infiltration depth after the ponding time (including I_p). For the sake of convenience, the formula may be revised as

$$K[t - (t_p - t_s)] = I - S(\theta_s - \theta_i)\ln\left[1 + \frac{I}{S(\theta_s - \theta_i)}\right],$$

(4.36)

in which $t_s < t_p$ represents the time needed for reaching the same accumulative infiltration I_p (or $i = p$) supposing ponding occurs initially. It is determined by

$$Kt_s = I_p - S(\theta_s - \theta_i)\ln\left[1 + \frac{I_p}{S(\theta_s - \theta_i)}\right]$$ (4.37)

The main idea of revision is to assume the entire process as ponding infiltration from the very beginning. Therefore, the whole curve should be translated to the left by $t_p - t_s$ and translate back to the right by $t_p - t_s$. In this manner, we may continue to use the Green–Ampt model after ponding by introducing a pseudo-time concept.

However, the steady rainfall is unable to meet the requirements in actual applications. Chu (1978) generalized the GA-ML model again to the unsteady rainfall process. The main procedure is to sort the ground surface conditions into four kinds for each time step:

(1) no ponding at the beginning, no ponding at the end
(2) no ponding at the beginning, ponding at the end
(3) ponding at the beginning, ponding at the end
(4) ponding at the beginning, no ponding at the end

At the beginning of each time interval, the total rainfall quantity, the total infiltration quantity and the total excess quantity are known. Whether the ponding occurs at the end of the interval could be distinguished by two indices, where c_u is used for determining whether ponding occurs at the beginning of the interval, while c_p is used for determining whether ponding occurs at the end of the interval:

$c_u = P(t_n) - R(t_{n-1}) - KSM/(i - K)$
$c_u > 0$ ponding at the end of the interval,
$c_u < 0$ still no ponding
$c_p = P(t_n) - I(t_n) - R(t_{n-1})$
$c_p > 0$ still ponding at the end of the interval,
$c_p < 0$ ponding disappears,

where M represents $\theta_s - \theta_i$. Provided that $i < K$, there is no ponding all the time and we need not use these two indices.

c. *Kinematic Wave Theory*

Because of the very thin depth of overland flow and the complicated boundary conditions, it is a tough task to describe the movement of this kind of

flow appropriately. Usually, one-dimensional shallow water equation (Saint Venant equation) is used in modeling of overland flow (Emmett, 1978).

$$h\frac{\partial v}{\partial t} + v\frac{\partial h}{\partial x} + \frac{\partial h}{\partial t} = q_* \qquad (4.38)$$

$$\frac{\partial v}{\partial t} + v\frac{\partial v}{\partial x} + g\frac{\partial h}{\partial x} + q_*\frac{v}{h} + g(S_\mathrm{f} - S_0) = 0 \qquad (4.39)$$

in which t is the time, x the distance, h and v represent the runoff depth and velocity, q_* means rain excess, S_0 the slope, S_f the energy slope, and g the gravity acceleration.

Nevertheless, Saint Venant equation always needs more parameters. As for runoff, most researchers prefer to describe overland flows by the so-called kinematic wave theory. Actually, it is a simplified form of the one-dimensional Saint Venant model. Woolhiser and Ligget (1967) have ever analyzed the one-dimensional unsteady overland flow. They found that when the kinematic wave number $K > 20 (K = S_0 L/h_0 F_0^2)$, (in which S_0 is the slope, L the runoff length, h_0 the depth of the runoff at the distance L, F_0 is the Froude number) and $F_0 > 0.5$, the kinematic wave model can describe overland flow quite well. Actually the kinematic wave number is certainly much greater than 10 on the Loess Plateau as Shen (1996) reported. Therefore, the kinematic wave approximation turns out to be a suitable mathematical description of the runoff generation process on the Loess Plateau. Till now there have been some revisions in the kinematic wave model (Ponce *et al*., 1978; Govindaraju, 1988). If the streamwise variation of water depth is considered by introducing an additional pressure gradient term, it becomes diffusion wave model.

The main assumption of the kinematic wave model is that the gravity component along the slope is equal to the resistance force ($S_\mathrm{f} = S_0 = \sin \theta$) and thus a concise relationship between discharge and water depth is established. Considering that the slope gradients on the Loess Plateau are generally precipitous, Eqs. (4.38) and (4.39) could be simplified as (Chen and Liu, 2001):

$$\frac{\partial h}{\partial t} + \frac{\partial q}{\partial x} = p \sin \theta - \mathrm{i}$$
$$q = \frac{1}{n} h^{5/3} S_0^{1/2}$$

where x is the coordinate alone the flow direction (m), t the time (s), h the water depth (m), q the unit discharge (m²/s), p indicates the rainfall intensity (m/s), $S_0 = \sin \theta$ the slope gradient and θ the inclination angle of slope (in degree), and n the Manning roughness coefficient.
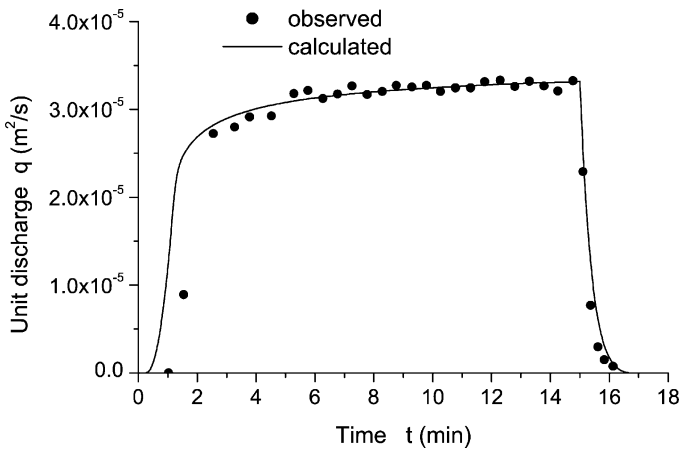
FIG. 14. Variation of the runoff generation process on a permeable slope. The comparison of the calculated (line) and experimental (dots) unit discharge at the outlet (experimental data are from Lima, 1992).

The laboratory experimental data of Lima (1992) are used to verify the performance of the model. This experiment was proceeded in a flume with length 1 m, width 0.5 m and slope $S_0 = 0.1$. The rainfall intensity was 0.03741 mm/s together with other soil parameters as follows

$$K = 1.67 \times 10^{-6}\ \text{m/s}, \qquad \theta_s = 0.506, \qquad \theta_i = 0.0107, \qquad S = 0.02\ \text{m}$$

Figure 14 is the comparison of calculated result and the experiments of the unit discharge at the outlet. The simulated diagram shows good agreement between them except during the very short initial period. It is especially encouraging to find the consistency between the theory and the experiment when runoff is about to stop. The results indicate that the model presented in this paper can efficiently simulate the runoff generation on the slope.

Moreover, we have analyzed various factors affecting the major parameters as well as the process of rainfall−infiltration−runoff generation (Chen *et al.*, 2001a). The results are shown in Fig. 15, and we can obtain the following principal conclusions:

(1) Each dynamic parameter (unit discharge, water depth, velocity, shear stress) grows as the rainfall intensity is increasing;
(2) Each dynamic parameter increases as the infiltration rate is diminishing;
(3) Each dynamic parameter rises as the slope becomes longer;
(4) Each dynamic parameter decreases as the volumetric soil water deficiency (the difference between the saturated water content and the initial water content) becomes larger;
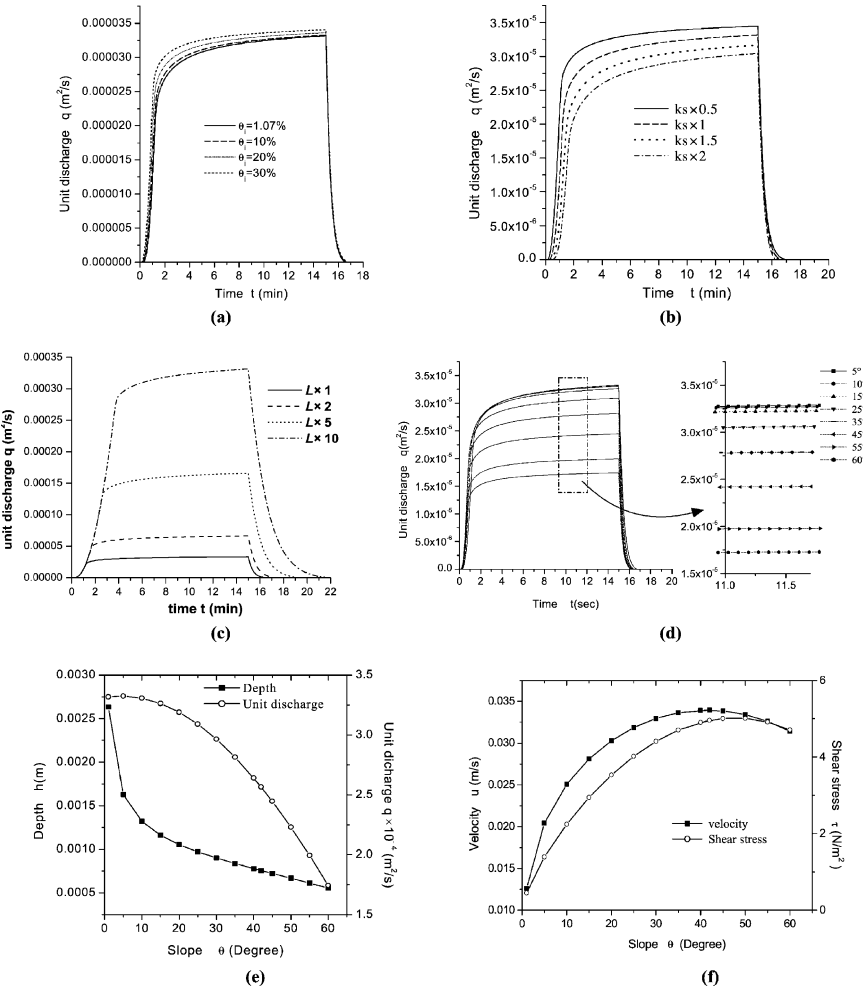
FIG. 15. Variation of runoff generation with various major affecting factors. (a)–(d) Unit discharge (m³/s) vs time. ((a) For different initial volumetric water contents. (b) For different saturate conductivity of soil. (c) For different lengths of slope surface. (d) For different slope gradients). (e) Unit discharge and water depth vs slope degree. (f) Velocity and sheer stress vs slope degrees.

(5) The water depth and the discharge rate of overland flow decrease with the increase of the slope gradient.

(6) The slope gradient plays both positive and negative roles on the flow velocity and shear stress of overland flow. The flow velocity and shear stress increases at first and then began to decrease when the slope gradient reaches their respective critical values. Although the corresponding critical

slopes are not equal, both of them are estimated within the range of about 40–50°. This conclusion also accords with our theoretical analysis (Liu *et al.*, 2001) well.

2. *Runoff Generation Characteristics in Typical Erosion Regions*

a. *Typical Erosion Regions*

Generally speaking, the soil erosion intensity is gradually increasing from the south to the north in the Loess Plateau area (Chen *et al.*, 1988; Chen, 1996). According to Liu's research (1965), this area could be partitioned into three belts correspondingly, namely clay loess belt, loess belt and silt loess belt. We choose one typical region in each belt and then simulate runoff generation in these typical regions in order to analyze the characteristics of runoff generation under different rain types.

These three regions are marked as region N, M and S, respectively (see Fig. 16, Chen *et al.*, 2001a). Region N is located at the Yellow River valley with extremely intensive erosion in the northeast of Shanxi province just adjacent to the border of Sanxi province. The soil there belongs to silt loess, its grain is relatively coarse
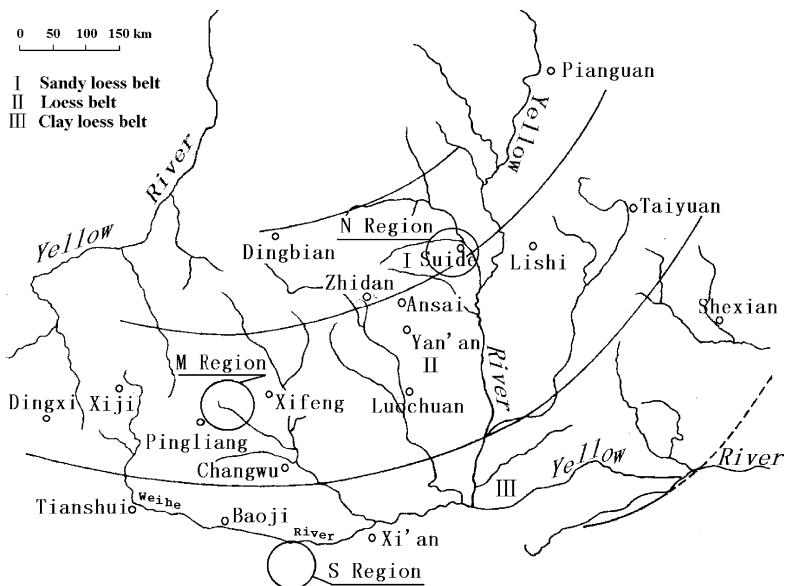

FIG. 16.   The sketch of the Loess Plateau and the selected typical regions.

and the clay content is quite low. Region M denotes the area around Gu Yuan–Ping Liang–Xi Feng with intermediate intensity of erosion in the central Shanxi. The soil there belongs to loess and its property is between clay and silt loess. Region S is at the Weinan plain with slight erosion intensity. The soil there belongs to clay loess, its grain is relatively fine and the clay content is high.

The modeled slopes are all assumed flat and barren without any vegetation cover. The calculated slope length is 30 m in each case study. We take the average values of the slope distribution provided by Jiang (1997) as slope gradient. In the long run, the slope inclination of regions N, M, S are selected as 28°, 22.6°, 14.3°, respectively.

The basic characteristics of soil have great effects on the runoff generation and soil erosion processes. According to the previous research (Jiang, 1997; Yang, 1996; Tang and Chen, 1994; Qi and Huang, 1997), we have determined the characteristic parameters of soil in the three typical regions in Table V.

b. *Determination of Rainfall Process*

Choosing uniform rainstorm, three single-peak rainstorms (Type A) and two multi-peaks (Type B) rainstorms, we have designed rainfall patterns for all circumstances. The whole duration of Type A rainstorm is 1 h and the total rainfall is 60 mm while 6 h and 120 mm for Type B rainstorm (with two peaks). The peak of type A1 rainstorm is in the middle of the duration, whereas the peak of Type A2 at the beginning and the peak of Type A3 rainstorm at the end. The higher peak of Type B1 rainfall is before the lower peak and the Type B2 rainfall is just the opposite. These diagrams are shown in Fig. 17 (Chen *et al.*, 2001a).

c. *Runoff Generation Characteristics*

By using the runoff generation model mentioned above, we have calculated the runoff generation processes of six rainfall types, respectively (Chen *et al.*,

TABLE V
SOIL CHARACTERISTIC PARAMETERS

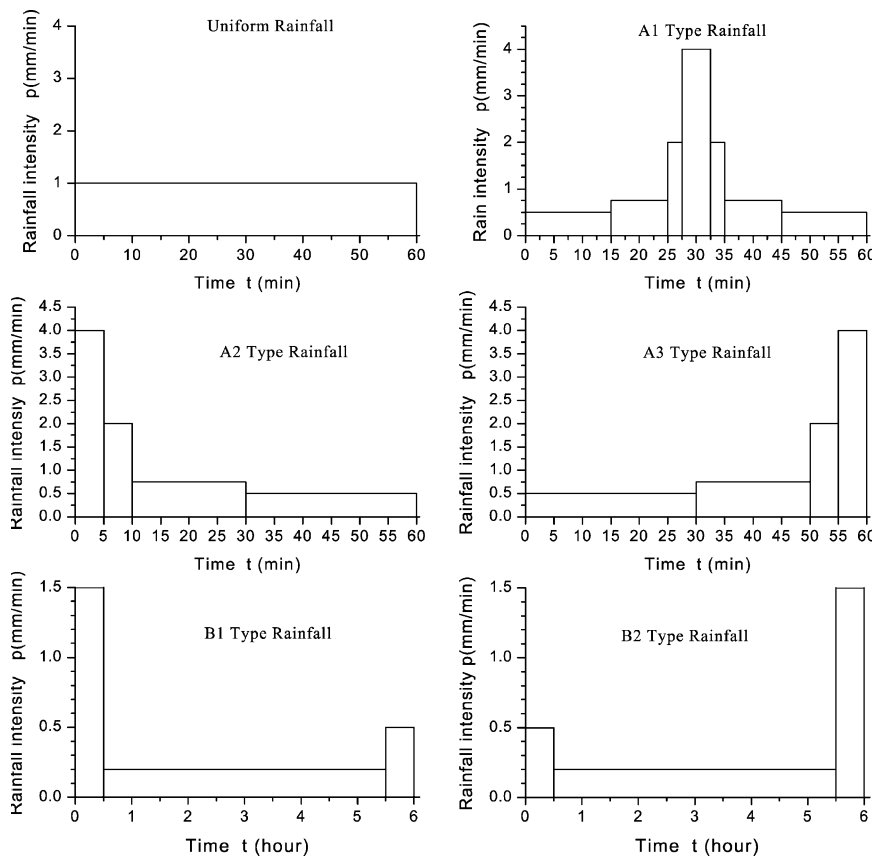| Parameter	N region	M region	S region
Infiltration coefficient K (mm/min)	0.75	1.08	0.92
Porosity θ_s (%)	57	55	50
Initial moisture weight percentage (%)	$14.4 \times 50\%$	$21.0 \times 70\%$	$20.7 \times 70\%$
Soil suction S (m)	0.06	0.10	0.15
Roughness coefficient n	0.03	0.03	0.03

FIG. 17. The types of rainfall process. Based on the analysis on rainfall characteristics on the Loess Plateau, six types of rainstorms are designed for calculation: a uniform rainstorm, three types of single-peak rainstorms (Type A) and two sorts of multi-peaks (Type B) rainstorms.

2001b), that is, a uniform rainstorm, three Type A rainstorms and two Type B rainstorms.

The calculated results of the runoff generation ratio in every region and for every rain type are listed in Table VI. The runoff generation ratio is mostly above 50% for Type A rainfall, or even near 70% in some areas. In contrast, it is around 30% for Type B rainfall or near 50% at most. This result is consistent with the conclusion by Wang and Jiao (1996). We can find from the table that the runoff generation rate is increasing from the south to the north. In the context of runoff generation, we can predict that the erosion force in the northern region is stronger than that in the southern region under the same rainfall conditions. Furthermore, the comparison of different rain types shows that the runoff generation ratio of

TABLE VI
RUNOFF GENERATION RATIO OF EVERY TYPICAL REGION UNDER DIFFERENT RAINFALLS

Rain type	Region		
	N region	M region	S region
Uniform	0.666	0.518	0.485
A1	0.680	0.556	0.529
A2	0.664	0.509	0.474
A3	0.678	0.559	0.537
B1	0.497	0.301	0.281
B2	0.502	0.332	0.322

Type A rainstorm is always larger than that of Type B rainfall. And the later the peak of rainfall intensity appears, the larger the runoff generation ratio. Thus, the rainfall with later peak exhibits more powerful erosion capability than that with earlier peak.

The runoff generation characteristics in different erosion intensity regions, including the unit width discharge q, water depth h, flow velocity u, shear stress τ varying with time at the slope outlet for each rain type have also been studied as shown in Figs. 18 and 19 (Chen *et al.*, 2001a), respectively.

By carefully analyzing the runoff generation process in the Loess Plateau region under different types of rainfall conditions, we have obtained the following main conclusions: Under the same rainfall conditions, the runoff generation ratio in the Loess Plateau region tends to increase from the south to the north. At the same time, the hydraulic parameters such as the unit discharge, flow velocity, shear stress as major influencing erosion factors generally agree with this tendency. The runoff generation ratio of Type A rainstorm with shorter duration and higher intensity is larger than that of Type B rainstorm with longer duration and relatively lower intensity. The peak values of flow parameters for Type A rainfall are higher than Type B rainfall, whereas it lasts for shorter duration correspondingly. The effects of the two types of the rainfall manifest themselves differently in different regions. Generally speaking, the later the peak of rainfall, the higher the peak values of runoff generation parameters and the higher the erosion capability of sheet flows.

3. *Dynamic Overland Flow Hydraulics*

a. *Foundation of Dynamic Model*

While the surface of a hill slope appears undulant in the transverse direction, the overland flow may direct to lower area, and form concentration flow route,
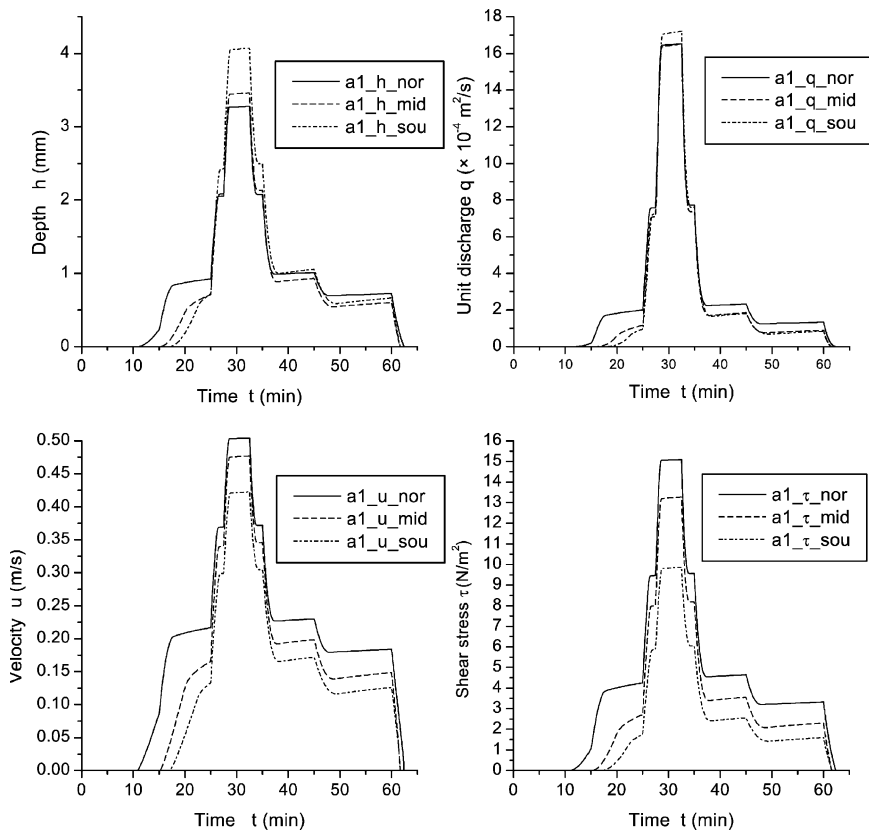
FIG. 18. Runoff generation characteristics of Type A1 rainfall in different erosion intensity regions, including the unit width discharge q, water depth h, flow velocity u, shear stress τ varying with time at the slope outlet. Type A1: single-peak rainstorm. nor: region N, mid: region M, sou: region S.

which ultimately results in rill formation. Because of the fragment geomorphy in the Loess Plateau area, the reasonable simulation of this concentrated flow route on the surface landform of hillslope is of primary importance for prediction of runoff generation and soil erosion in this area.

Obviously, a one-dimensional dynamic model is inadequate to properly simulate the flow routing caused by the landform. On the other hand, it is also infeasible to simulate the process of flow concentration by a two-dimensional full Saint Venant equation system because of the thin flow depth and the complex geomorphy. One potential numerical approach is to introduce two-dimension grids on the slope surface, and the flow in a cell is simulated by
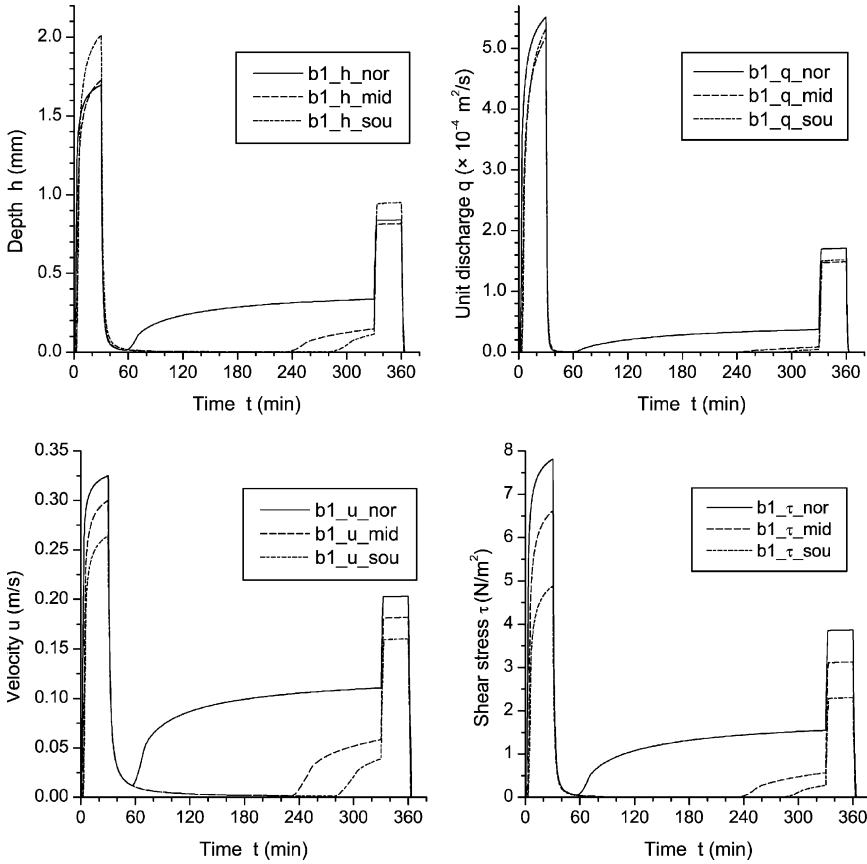
FIG. 19. Runoff generation characteristics of B1 Type rainfall in different erosion intensity regions, including the unit width discharge q, water depth h, flow velocity u, shear stress τ varying with time at the slope outlet. Type B1: multi-peaks rainstorm. nor: region N, mid: region M, sou: region S.

one-dimensional dynamic model. The different flowline routine is specified in every grid and the inflow discharge into and the outflow discharge from the adjacent grids is calculated. Based on this concept Scoging (1992) developed a distribution mathematical model of hillslope overland flow by determining the direction of flow according to the heights of the four corners of computational elements or cells. The flowline vector was represented as originating from the highest corner of a cell, with its magnitude and direction determined by the relative heights of four corners of the cell. The side intersecting the vector was considered the outlet of the cell for flow, assuming that all the water of

the element flows out from this side. So every element exports water to the adjacent element, at the same time every element receives the water flow from the four adjacent elements. Using a one-dimensional difference equation obtained between the downstream cell and its several upstream neighboring cells, the process of the run-off and the concentrated water flow route was described for the whole area. Nevertheless, this method possesses an apparent drawback in flow routing. Actually, water in a cell tends to flow out through two lower side boundaries instead of one side boundary.

Based on the analogue approach to previous investigation, we have developed a dynamic model that can handle the runoff concentrating process more adequately.

As in Fig. 20, the slope is partitioned into rectangle grids. This so-called rectangle is the projection of the grids to the horizontal plane. Assuming the element plane as a bilinear element, represented as:

$$z = f(x, y) = (ax + b)(cy + d) \tag{4.41}$$

where z is the height of the element, x and y are the abscissa and ordinate, respectively.

$$\text{Grad} f(x, y) = \frac{\partial f}{\partial x}\mathbf{i} + \frac{\partial f}{\partial y}\mathbf{j} \tag{4.42}$$

Taking the slope gradient of the center point of the element as the slope gradient of the whole element, the representative slope gradient θ can be obtained by:
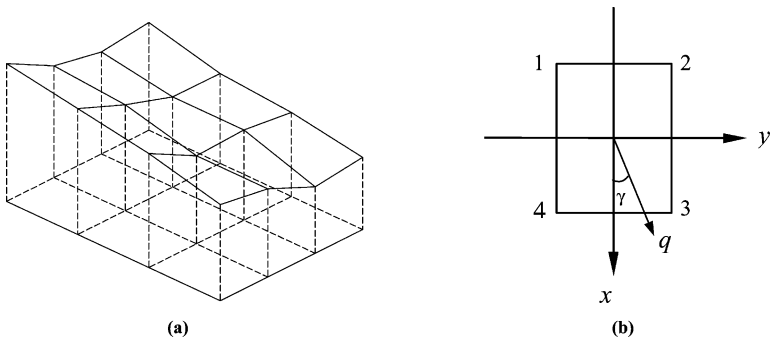

FIG. 20. Sketch of two-dimensional grids and cell flow direction. (a) Two-dimensional grids (The projection of grids to the horizon plane forms rectangles). (b) Cell flow direction and four corner marks.

$$tg\theta = |\operatorname{Grad} f(x, y)| = \sqrt{\frac{(z_1 + z_2 - z_3 - z_4)^2}{4dx^2} + \frac{(z_1 - z_2 - z_3 + z_4)^2}{4dy^2}} \quad (4.43)$$

and the flowing vector direction angle γ looks

$$tg\gamma = \frac{\partial f}{\partial y} \Big/ \frac{\partial f}{\partial x} = \frac{dx}{dy} \frac{(z_1 - z_2 - z_3 + z_4)}{(z_1 + z_2 - z_3 - z_4)} \quad (4.44)$$

where z_1, z_2, z_3 and z_4 are the heights of four corners, respectively; dx and dy values are the projected grid lengths on the horizontal plane in the x and y directions, respectively.

Assuming that the water flow direction is controlled completely by the landform of hillslope, and the water interaction may not affect its flow direction, the water in every element is considered flowing out along the flow direction angle into the two adjacent grids. So the flow route may usually intersect with two sides of the cell. If the unit discharge is q, then the unit discharge along the x and y directions are:

$$q_x = q \cos \gamma, \qquad q_y = q \sin \gamma$$

Consequently, we can derive the governing equations of overland flow as follows:

$$\begin{cases} \dfrac{\partial h}{\partial t} + \dfrac{\partial q_x}{\partial x} + \dfrac{\partial q_y}{\partial y} = p \cos \theta - i \\[2mm] q = uh = \dfrac{1}{n} h^{5/3} S_0^{1/2}, \quad q_x = q \cos \gamma, \quad q_y = q \sin \gamma \end{cases} \quad (4.45)$$

b. *Laboratory Experiments*

The process of runoff generation and flow concentration on a hillslope with rugged landform was investigated experimentally in the Chinese National Key Laboratory of Soil Erosion and Dryland Farming in Loess Plateau, the Northwestern Institute of Water and Soil Conservation of Chinese Science Academy, China. The drop-former type rainfall simulator was employed to generate artificial rainfall. Raindrops were formed at 16 m above the ground, falling down at a fixed speed near the surface of the test plot. The rainfall intensity is adjustable in the range of 15–200 mm/h.

The soil used in this experiment was the local loess of Yangling in Shanxi province of China. The soil was packed into a 320 cm long, 100 cm wide and 30 cm deep wooden-box with holes on the bottom, and controlled to reach a bulk

density of 1.3 g/cm^3. In the experiment, the slope gradient of the soil box was secured at 10°. The initial surface landform is shown in Fig. 21 exhibiting three main grooves on the slope surface.

The rainfall intensity adopted in this experiment was 1.6 mm/min, and the rainfall duration was 1 h.

The runoff volume at the test plot outlet was measured, and the flow velocities at several specific points were also measured using stained method at different times from the beginning of runoff formation.

c. *Model Validation*

Using the proposed model, the process of runoff generation and flow route concentration on the test plot were simulated (Fig. 22). The model parameters used in simulation are shown in Table VII.

Figure 23(a) shows the distribution of simulated flow depths on the entire test slope. In the figure, the position with larger values of water depth is on the right where the water starts to concentrate into a route. Compared to the experimental

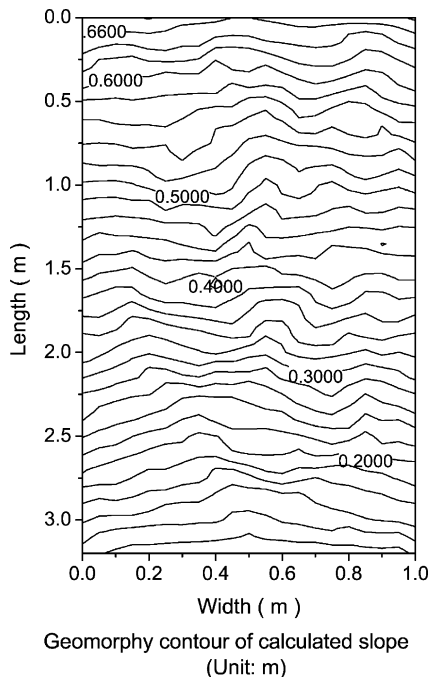
Geomorphy contour of calculated slope
(Unit: m)

FIG. 21. Initial geomorphic contours of the slope surface (Unit: mm). The test wooden-box is 320 cm long, 100 cm wide and 30 cm deep.

TABLE VII
COMPUTE PARAMETERS

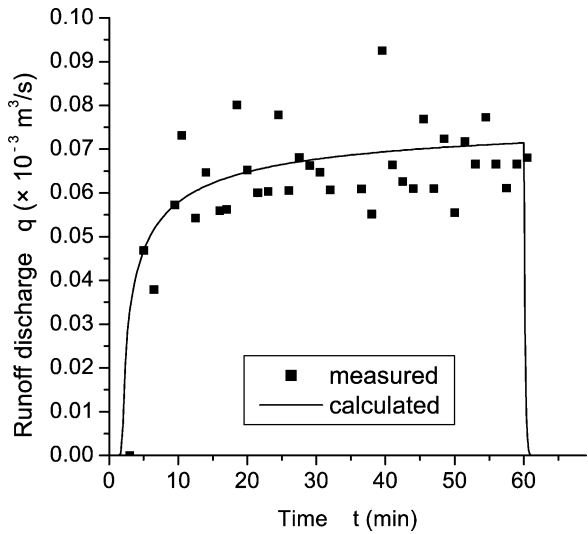|	
Porosity of soil	50.27%
Initial water content	22.62%
Permeability coefficient	0.1 mm/min
Soil suction	0.15 m
Roughness coefficient	0.03

FIG. 22. Comparison of simulated and experimental results of runoff discharge. Line: simulation, dots: experiment.

result in Fig. 23(b), the agreement between simulated result and experimental observation is excellent, implying that the present model is capable of simulating the runoff generation and concentrated flow route on the hillslope.

4. *Rill Erosion Estimation*

Rill erosion is a principal form of soil erosion caused by overland flow. Generally speaking, overland flow brings forth sheet erosion at first, then start to cause rill erosion with increasing flux. The rill erosion is commonly seen in the Loess Plateau area as rainstorm occurs on the steep slope there. Previous research
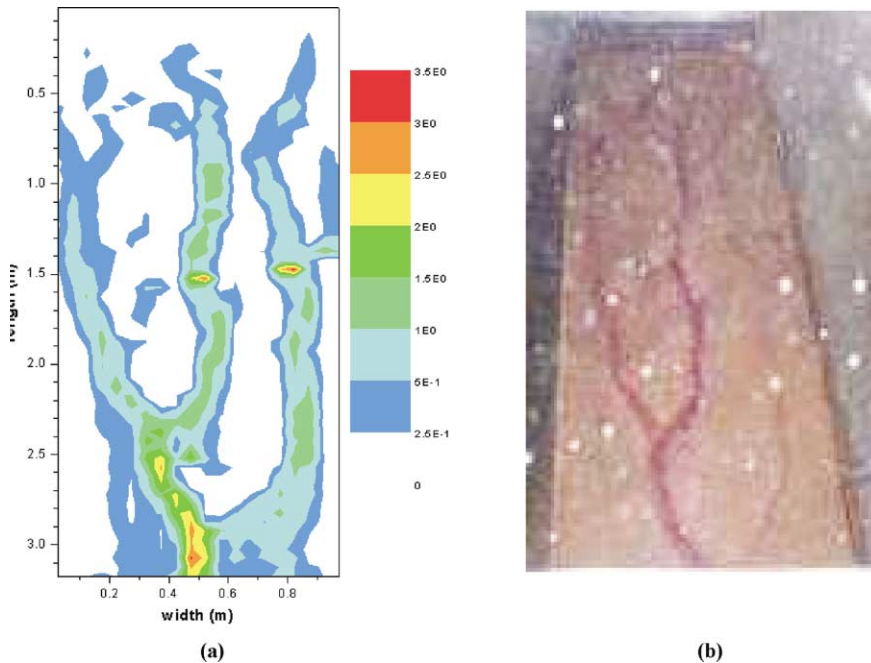
FIG. 23. Comparison of simulated and observed flowline routine concentration on the slope as shown in Fig. 12(a) Simulated result of water depth contours (unit: mm). (b) Observation of flowlines on the slope surface.

has shown that the rills on the hillslope of Loess Plateau are usually as wide as 5–20 cm with the depth less than 20 cm (Liu *et al.*, 1998).

After the rill occurs on the hillslope, the sheet flow will convert into concentrated flowline, and its depth, velocity and erosion capability all rapidly increase. Lots of research (Zhang, 1991; Zheng and Kang, 1998) demonstrated that the rill erosion intensity would be severe, even scores of times of the interrill erosion, and the sheet erosion can be ignored compared with the rill erosion. So understanding rill erosion mechanism is of primary significance for prediction of soil erosion.

a. *Experimental Research*

Generally, the formation of rill is irregular, and its length, width, depth and form are changing during erosion process. For non-uniform soil, rugged hillslope surface and unsteady flow, the generation and development of rill are more stochastic. The situation brings much difficulty in rill erosion study. In order to better understand the rill erosion law, a series of rill erosion experiments with soil
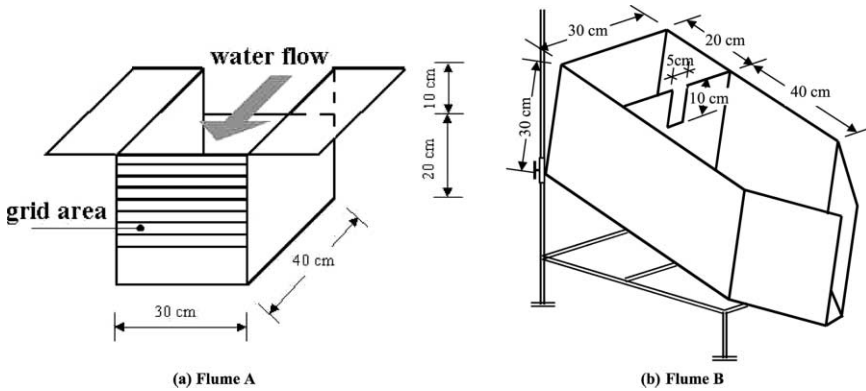
FIG. 24. The sketch of experimental equipment. (a) Flume A: Soil box that is used to pack soil. In experiment, a 10 cm long, 5 cm wide and 2 cm deep rill from the outlet is artificially made along the center line of flume A. (b) Flume B: Trestle flume. Its slope gradient can be adjusted according to experimental requirement. During experiment, the flume A was fixed in the flume B.

flume was carried out in the Chinese National Key Laboratory of Soil Erosion and Dryland Farming in Loess Plateau, the Northwest Institute of Water and Soil Conservation of Chinese Science Academy, China. The experimental soil flume is shown in Fig. 24.

During experiments, the soil was firstly packed into flume A 20 cm thickness, and then adjusted to reach actual bulk density of 1.3 g/cm^3. A 10 cm long, 5 cm wide and 2 cm deep groove from the outlet is artificially made along the center line of flume A. Then we fixed the flume A in the flume B and adjusted the flume B to required slope gradient. The water flow is supplied at the top inlet of flume instead of artificial rainfall. This experimental method can easily manipulate the flow discharge (runoff rate) well, and assure the water flow in the groove directly to form rill erosion at the very beginning of experiment. Thus, we can directly obtain the relation of erosion rate and runoff by neglecting splash erosion. In addition, relatively larger amount of rill flow discharge may be obtained in a small scale test.

The soil used in experiments is the local loess of Yangling in Shanxi province of China. Before the experiments, the soil was sprinkled in water so as to approximately saturate the surface soil. Five slopes of 5, 10, 15, 20, 25° and five flow discharges of 0.01×10^{-3}, 0.025×10^{-3}, 0.05×10^{-3}, 0.075×10^{-3}, 0.1×10^{-3} m^3/s for each slope were designed in experiments. The rill erosion rate, rill flow velocity, depth and width were measured carefully.

Part of experimental results demonstrating the relations among sediment transport rate, rill flow discharge and slope gradient are shown in Fig. 25.
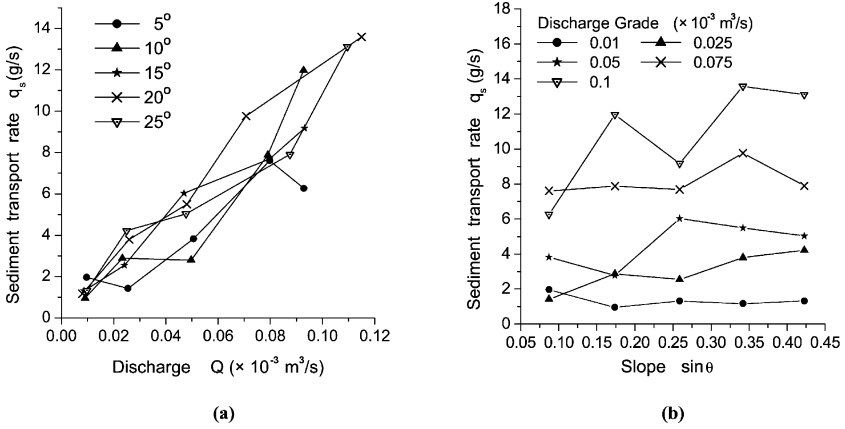
FIG. 25. The experimental results of rill erosion. (a) Sediment transport rate vs rill flow discharge in five different slope gradients (5, 10, 15, 20, 25°). (b) Sediment transport rate vs rill flow discharge in five different discharge grades (0.01×10^{-3}, 0.025×10^{-3}, 0.05×10^{-3}, 0.075×10^{-3}, 0.1×10^{-3} m³/s).

Although the results fluctuate greatly owing to the inherent randomness of rill erosion, the rule that rill erosion rate varies with slope gradient and rill flow discharge is comparatively clear. Total erosion quantity increases as the slope gradient and the discharge of rill flow.

Lots of research show that the width of rill has relatively good correlation with runoff discharge Q and slope gradient S. Supposing that there exists exponential relationship, we obtain the following formula by using multi-variable linear regression.

$$B = 0.596Q^{0.316}S^{-0.23} \qquad (4.46)$$

where B is the rill width (m), Q the discharge of rill flow (m³/s), and S the slope gradient. The correlation coefficient in the above formula is $r = 0.674$. This formula is close to the relationship obtained by Zhang (1999) on Loess hillslope.

We found that the wet perimeter of rill flow has better relation with runoff discharge Q and slope S. If the rill width B is replaced by wet perimeter p, then

$$p = 1.512Q^{0.371}S^{-0.245} \qquad (4.47)$$

It is obviously a better relationship compared with formula (4.46) with correlation coefficient $r = 0.9011$.

b. *Rill Erosion Model*

Similar to that in open channel, the sediment transport in the rill flow should also satisfy the mass conservation law. Supposing the sediment transport process in the rill is steady, the following equation can be utilized to express the rill erosion rate (Huang *et al.*, 1996):

$$\frac{dq_s}{dx} = D_r + D_i \tag{4.48}$$

where q_s is the erosion rate per unit width, D_r the rill erosion rate, and D_i the interrill erosion rate. The sediment coming from interrill is supposed to be totally transported through rill flow. This differential equation is also adopted in other physics-based erosion model, such as WEPP.

Supposing the rill erosion rate is proportional to the difference of saturated sediment transport capacity and real sediment transport rate q_s in rill flows, we have

$$D_r = \alpha(T_c - q_s) \tag{4.49}$$

Obviously, T_c represents the transport capacity of rill flows. α is a coefficient, its reciprocal, $1/\alpha$ with a length dimension, implying the distance that sediment concentration of rill flow reestablishes from zero to the maximum capacity, i.e., saturated sediment transport. The expression of α should be determined by further study.

Physically, two aspects should be pointed out in formula (4.49): one is that the erosion capability of rill flow has a limit value relating to its transport capacity, which is not more than αT_c, the other is that the erosion capacity of rill flow may decrease gradually as the sediment concentration increases. When the sediment concentration in rill flow is saturated, the rill erosion stops.

The interrill erosion is negligibly small compared with rill erosion, so Eq. (4.48) is simplified in the following form:

$$\frac{dq_s}{dx} = \alpha(T_c - q_s) \tag{4.50}$$

Supposing that T_c is constant, the soil is homogeneous, and the sediment transport rate is zero at the inlet, we can solve Eq. (4.50) analytically:

$$q_s = T_c(1 - e^{-\alpha x}), \tag{4.51}$$

which can be considered as a basic formula describing rill erosion. Then, the coefficient α turns out to be

$$\alpha = -\frac{\ln(1 - q_s/T_c)}{x} \tag{4.52}$$

Since there is no formula of sediment transport rate especially for sheet flow and rill flow till now, the sediment transport rate in river dynamics is still widely used. Some scholars used experimental data of sheet flow and rill flow verified their validity, but unable to obtain consistent result between majority of them. Foster and Meyer (1977) and Alonso *et al.* (1981) recommended Yalin's formula, Moore and Burch (1986) suggested Yang's formula, Lu *et al.* (1989) considered Engelund and Fredsoe's as the best and Govers (1992) thought Low's was better. According to the experimental data, we find that the results given by Yalin are more reasonable for the soil of Loess Plateau. Yalin's formula can be expressed as

$$q_s = GY^{0.5}(Y - Y_c)d(gd(s-1))^{0.5}\rho_s \tag{4.53}$$

$$G = \frac{0.635}{Y_c}\left[1 - \frac{\ln(1+as)}{as}\right] \tag{4.54}$$

$$as = \frac{2.45}{s^{0.4}}Y_c^{0.5}\left(\frac{Y}{Y_c} - 1\right) \tag{4.55}$$

where Y is the dimensionless shear stress, $Y = \tau/[(\rho_s - \rho)gd]$, τ is flow shear stress, N/m^2. Y_c is the dimensionless critical shear stress force, $Y_c = \tau_c/[(\rho_s - \rho)gd]$, τ_c is the critical shear stress, N/m^2. ρ is the density of fluid, kg/m^3, ρ_s the density of sediment, kg/m^3, $s = \rho_s/(\rho_s - \rho)$. d is the diameter of sediment, m, g gravitational acceleration, m/s^2, R hydrodynamic radius, m. S_0 ($= \sin\theta$) represents the slope gradient, θ is the angle of a hillslope.

Generally, the soil is mainly separated by rill flow in the form of single particle or aggregation of some particles to be similar to the process of sediment transport in open channel flow. So we choose Dou's (1999) formula to describe the critical shear stress τ_c.

$$\tau_c = k^2\rho\left[\frac{d'}{d_*}\right]^{1/3}\left[3.6\frac{\rho_s - \rho}{\rho}gd + \left[\frac{\gamma_0}{\gamma_{0_*}}\right]^{5/2}\left[\frac{\varepsilon_0 + gh\delta\sqrt{\delta/d}}{d}\right]\right] \tag{4.56}$$

where k is a non-dimensional parameter, $k = 0.128$, d' the characteristic diameter (mm), d_* the referenced diameter, and is taken as 10 mm, h the water depth, ε_0 the parameter of adherence force, for ordinary sediment $\varepsilon_0 = 1.75$ cm^3/s^2, δ the thickness parameter of water film, $\delta = 2.31 \times 10^{-5}$ cm, γ_0 the dry density of sediment (N/m^3), γ_{0*} is the stable dry density of sediment (N/m^3). According to our research, γ_{0*} can be determined by the following formula:

$$\begin{aligned}\gamma_{0*} &= 0.68\gamma_s(d/d_0)^n \\ n &= 0.080 + 0.014(d/d_{25})\end{aligned} \tag{4.57}$$

in which $d_0 = 1$ mm, d_{25} is the grain diameter, than which 25% of the total particles by weight is finer.

Formula (4.56) can relatively express the sediment incipient motion law of various diameters well, such as coarse sediment, fine sediment, cohesive sediment, and light sediment. For fine sediment-like soil, this formula specially considers two forces, the cohesive force between particles and the additional pressure of water film. In addition, the slope gradients on the Loess Plateau are usually large, so the influence of slope on soil particle's incipient motion should be taken into account. In accordance with Zhang *et al.* (1989), we have the critical shear stress on a slope:

$$\tau_c = k^2 \rho \left[\frac{d'}{d_*} \right]^{1/3} \left[3.6 \frac{\rho_s - \rho}{\rho} g \cos \theta d + \left[\frac{\gamma_0}{\gamma_{0*}} \right]^{5/2} \left[\frac{\varepsilon_0 + g \cos \theta \, h \delta \sqrt{\delta/d}}{d} \right] \right]$$
(4.58)

Using Eqs. (4.52), (4.53) and (4.58), α and its governing law can be determined by means of our experimental data on rill erosion. Let $L_\alpha = 1/\alpha$, the experimental results show that the value of L has a trend to increase with the increase of discharge of rill flow and slope gradient, but the correlation is not very satisfactory. Considering the influence of various factors, such as the effective shear stress of the rill flow $\tau - \tau_c$, the hydraulic radius R, the velocity u, the diameter of soil particles d, the density of soil particles under water $(\rho_s - \rho)g$, and the slope gradient S_0, the relation can be acquired by using multi-variable regression of experimental data under the assumption of an exponential relation.

$$\frac{L_\alpha}{R} = 15165.8 \left[\frac{\tau - \tau_c}{(\rho_s - \rho)gd} \right]^{0.148} \left(\frac{u}{\sqrt{gd}} \right)^{-1.022} S_0^{1.550}$$
(4.59)

where the correlation coefficient $r = 0.9314$. The predicted value given by the above formula is compared with experiments in Fig. 26.

The rill erosion model is validated by a series of indoor artificial rainfall experiments which were accomplished by Li Zhanbin at the Chinese National Key Laboratory of Soil Erosion and Dryland Farming in Loess Plateau, Northwestern Institute of Water and Soil Conservation of Chinese Science Academy. The test plot used in the experiments is 320 cm long and 100 cm wide. According to lots of experiments, there are three rills to distribute evenly in a 1 m width hillslope, and the influx coefficient of rill flow is supposed to be 0.8. Two sets of experimental results are shown in Fig. 27.

The agreement between the predicted results and the experimental data shows that the present rill erosion model may effectively simulate rill erosion process and predict erosion rate on the Loess Plateau.
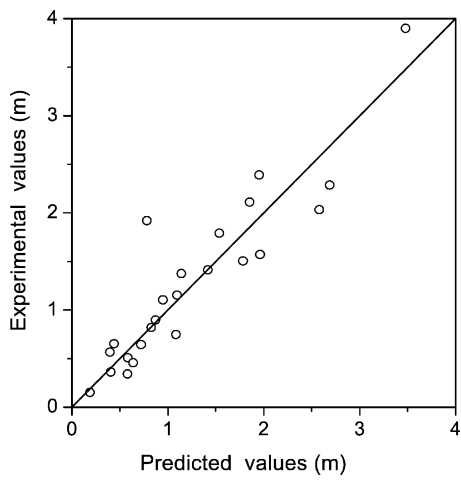
FIG. 26.   Comparison of calculated (line) and experimental results (dots) of L_α value. L_α has a length dimension, it represents the distance that sediment concentration of rill flow re-establishes from 0 to maximum value, i.e., saturated sediment carrying capacity.

c. *Rill Erosion Characters*

The rill erosion process is simulated with the present model according to variable slope gradient, slope length and rain intensity. Figure 28 shows the simulated results of rill erosion rate varying with time under different slope gradients, slope lengths and rain intensities.
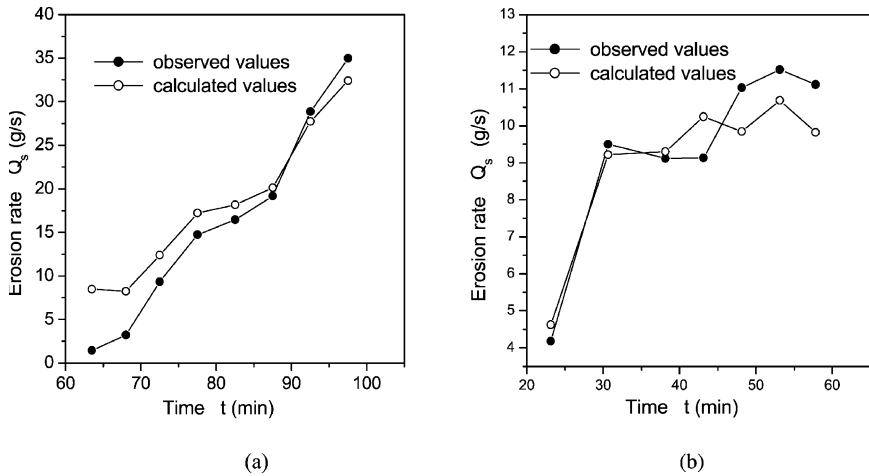

| (a) | (b) |

FIG. 27.   Comparisons of simulated and artificial rainfall experimental results of rill erosion rate. (a) Experimental condition: rain intensity: 1.0 mm/min, slope gradient: 20° (b) Experimental condition: rain intensity: 1.71 mm/min, slope gradient: 30°.
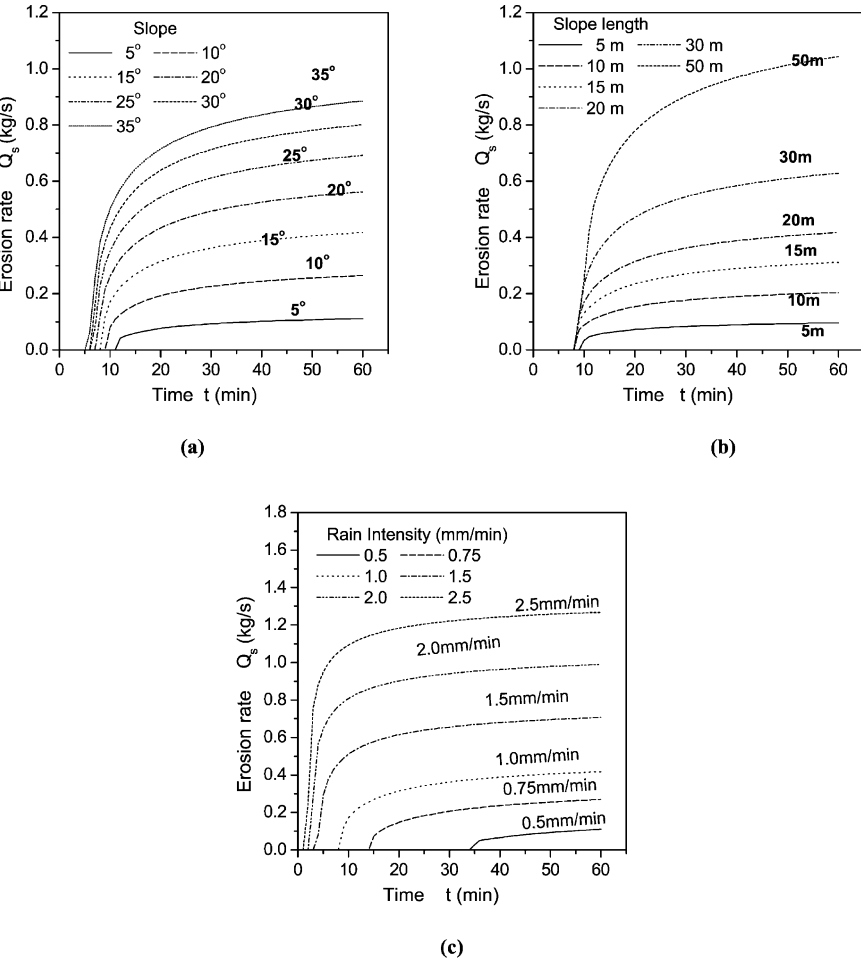
FIG. 28.   Simulated results of rill erosion rate with different slopes, rill lengths, slopes and rain intensities. (a) Rill erosion rate in seven different slope gradients (5, 10, 15, 20, 25, 30, 35°). (b) Rill erosion rate in six different slope lengths (5, 10, 15, 20, 30, 50 m). (c) Rill erosion rate in six different rain intensities (0.5, 0.75, 1.0, 1.5, 2.0, 2.5 mm/min).

Analyzing the simulated results, we may come to the following main conclusions:

The rill erosion rate is proportional to the length of slope. Because the infiltration rate decreases and runoff increases gradually, the sediment transport rate increases rapidly at the beginning and then slows down gradually till to a stable value. Correspondingly, the accumulative erosion quantity increases drastically at first and then increases linearly. The longer the slope is, the more

obvious the trend is. The fact shows that the main factor influencing rill erosion is runoff discharge as different slope lengths reflect the different runoff discharges at the outlet.

The sediment transport rate and the accumulative erosion quantity both increases with slope gradient. Generally speaking, the runoff discharge grows as slope gradient increases. However, it directly leads to the increase of shear stress. As a result, rill erosion rate may increase as slope gradient increases.

The influence of rain intensity on the rill erosion is similar to the slope gradient. The erosion rate and accumulative erosion quantity increases with rain intensity almost linearly. It is accounted for by larger runoff discharge during intensive raining. In addition, we find that the influence of rain intensity variation on the erosion rate in slight rainfall is more obvious than that in heavy rainfall.

C. Terrestrial Processes in Arid Areas, the Northwest China

It is reported by UNEP that desert land formation occurs at the rate of approximately 6 million hectares annually owing to global climate change and human activities. Meanwhile it has also become a bottleneck in the economic development of Northwest China. For example, Xinjiang as the largest province in China is rich in petroleum, gas and metal. Although local precipitation seems little, there is enough sunshine and water supply from rain in mountain area and melted snow. Therefore, we have cultivated a large expanse of oasis though many environment problems such as shrinking of rivers, drying of lakes and invasion of desert have become more severe than ever (Wu, 1992). An additional example is the 'San Bei' windbreak aiming to protect the railway from being buried by advancing desert. In the 1950s, a few kinds of drought-enduring plants surprisingly survived using cellular straw technique at the southern border of the Tenggeli Desert (Figs. 29 and 30). During the infant stage, they grew normally, thus forming a windbreak belt to hinder the movement of the desert (Li and Ouyang, 1996). Nevertheless, these plants started to wither due to the increase of water requirement and the formation of biological crust skin. Hence, the study of energy and water cycling at the interface of atmosphere and land is certainly beneficial to improving environment quality and developing regional economics. Of course, the objective of terrestrial process study is twofold. A better understanding of momentum, energy and mass exchange between land and atmosphere may provide reasonable parameterization scheme for meteorologists in AGCM as well.

F<small>IG</small>. 29.   *Artemisia ordosica*—a typical drought-enduring plant which was fitted by the cellular straw technique in the southern border of the Tenggeli Desert in order to prevent desert invasion and protect the Bao-Lan Railway since 1950s.
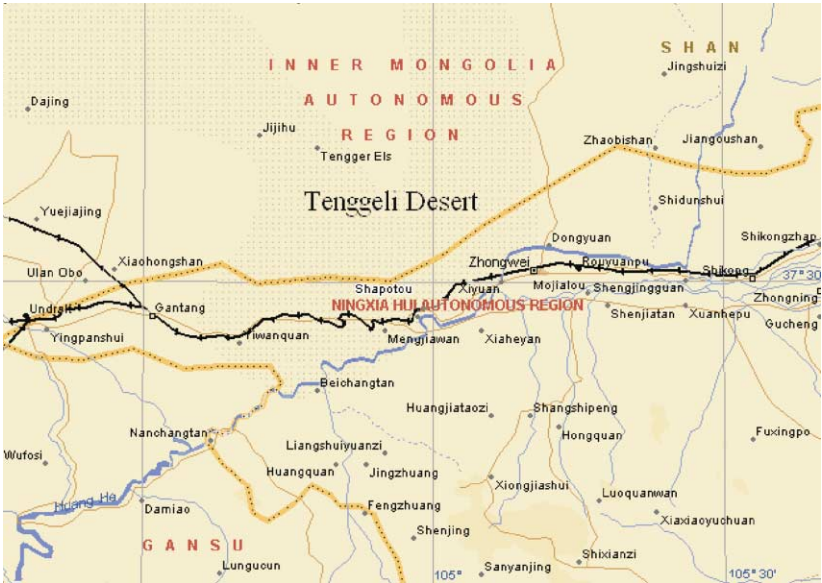

F<small>IG</small>. 30.   Location of windbreak, where black line is the BaoLan rail way, grey line is the Yellow river.

1. *SPAC System Models*

We have defined soil–plant–atmosphere as a Continuum (SPAC) to facilitate us to apply classical fluid mechanics or heat and mass transfer theories available in this field. There have been a number of models used for describing air, water and heat transport in the SPAC system so that micrometeorological states in vegetation and soil or parameterization scheme can be acquired. Generally speaking, these models may be classified as the following three categories:

a. *Force-Restore Method*

Basically, the force-restore model is of hydrologic nature. With planetary parameters measured at the anemometer height at one site, the force-restore model aims to predict water and heat motion in soil at different sites (Lin and Sun, 1986). Deardorff (1978) has compared different models among simple schemes and proved that the force-restore method is most satisfactory.

Sun and Lu (1992), Liu *et al.* (1996) and Sun *et al.* (1998) extended the theory to an area partly covered by vegetation. Liu and Sun have made a critical review on ecological aspects of water cycle by the same approach in 1999 (Liu and Sun, 1999). By considering the diurnal and seasonal variation in temperature and different heat diffusivity, the soil is divided into three layers, i.e., surface layer δ, diurnal layer depth d_1 (5–10 cm) and annual layer of depth d_2 (1–2 m):

$$\alpha \frac{\mathrm{d}T_\mathrm{g}}{\mathrm{d}t} = \frac{2G(0,t)}{cd_1} - \frac{2\pi}{\tau}(T_\mathrm{g} - \bar{T})$$

$$\frac{\mathrm{d}\bar{T}}{\mathrm{d}t} = \frac{2G(0,t)}{cd_2}$$

where T_g and $\bar{T}$ are the temperature at the surface layer and depth-averaged temperature, respectively, $G(0,t)$ the heat flux into the soil directly derived from the energy balance at the ground surface, τ the diurnal period, c the volumetric heat capacity of soil and α a weighted factor.

Based on the conservation principle, we may derive water cycling equations by dividing soil into shallow and deep layers with thickness $\bar{d}_1$ and $\bar{d}_2$ in a similar way:

$$\bar{d}_1 \frac{\mathrm{d}\theta_1}{\mathrm{d}t} = \left(I_\mathrm{b} - \frac{E_\mathrm{b}}{\rho_\mathrm{w}}\right)\sigma_\mathrm{b} + (I_\mathrm{c} - U_1)\sigma_\mathrm{c} - q_{12}$$

$$\bar{d}_2 \frac{\mathrm{d}\theta_2}{\mathrm{d}t} = q_{12} - q_{23} - U_2\sigma_\mathrm{c} \tag{4.61}$$

where θ_1 and θ_2 are the volumetric moisture contents in the upper and lower layers, U_1 and U_2 are the water uptake from upper and lower layers through roots, E_b is

the evaporation at bare soil, I_b and I_c are infiltration at bare or vegetated land occupying σ_b and σ_c of total area. Finally, q_{12} and q_{23} are the water transfer between layers.

In particular, we have noticed that real evaporation may differ from potential evaporation due to various factors such as: the effects of border in 20 m, the species and height of plants (usually conifer evaporated less than deciduous trees), the period of growth (coverage is larger during elongation and evaporation more in blossom and milk period). Generally, actual evaporation is estimated by potential evaporation multiplied by evapotranspiration coefficient:

$$E_m = K_c E_0 \qquad (4.62)$$

where

$$E_0 = \frac{\Delta R_n + \gamma E_a}{\Delta + \gamma} \qquad (4.63)$$

in which Δ is saturated vapor pressure, γ dry–wet constant, R_n denotes net radiation, E_a means drying force of air. Water is insufficient to supply plants growing in arid areas so that the evaporation is reduced correspondingly. As a matter of fact, that is one kind of physiological response to an unfavorable environment. Insufficient supply of water leads to lack of water in the plant body so as to close their stomata. The task for us is to determine two parameters: critical water capacity θ_k (about 75% of field capacity) under which the evaporation is greatly reduced and the assimilation process almost ceases; the water capacity for zero evaporation θ_p, which is even lower than wither point. Then, the evapotranspiration coefficient may be written as (Li *et al.*, 1997):

$$K_c' = \left\{ \begin{array}{c} \theta > \theta_k, \\ \theta_k \geq \theta > \theta_p, \\ \vartheta \leq \theta_p \end{array} \right\} \qquad (4.64)$$

b. *Turbulent Modeling*

As a matter of fact, people have recognized that the transfer of momentum, energy and mass is essentially turbulent. However, the force-restore model has entirely neglected the atmospheric motion, thus merely predicting the evolution of physical quantities in the soil and fluxes at the ground surface. The atmospheric states are heavily dependent on the observation in the surface layer. As early as in 1960s', Tan and Ling (1961) firstly applied turbulent models in the turbulence research in canopy. By regarding branches and leaves

of forest or crops as a sink of momentum and assuming the mixing length proportional to the height z, they successfully yielded wind profile with an inflexion at the top of canopy, which is in good agreement with observations. Mellor and Yamada (1974) developed a hierarchy of second-order models to simulate unsteady atmospheric boundary layer with varying thermal stratification. In regard to the coupling with soil layer, earlier crude model only used empirical relation of aerodynamic and water vapor resistance. Deardorff (1978) further proposed a concept of surface wetness function to represent this kind of interaction between air and soil. In 1980s', Naot and Mahrer (1982) and Ten Berge (1990) have established a coupling model for heat and water transfer in the lower atmosphere and the upper soil over bare or vegetation-covered field. Based on the previous investigations, we have constructed a comprehensive coupling model (Xie *et al.*, 1998; Li *et al.*, 1999a) both for AGCM parameterization in climate prediction and agricultural production enhancement or environment protection in micrometeorology with revised source and sink terms.

Then, the Reynolds Averaged Navier–Stokes equations including rotation and stratification effects for horizontally homogeneous atmospheric flows look like:

$$\frac{\partial \bar{u}}{\partial t} = f(\bar{v} - v_{\mathrm{g}}) - \frac{\partial}{\partial z}\left(\frac{\tau_x}{\rho}\right) - C_{\mathrm{d}}A(z)\bar{u}|\bar{u}|$$

$$\frac{\partial \bar{v}}{\partial t} = -f(\bar{u} - u_{\mathrm{g}}) - \frac{\partial}{\partial z}\left(\frac{\tau_y}{\rho}\right) - C_{\mathrm{d}}A(z)\bar{v}|\bar{v}|$$

$$\frac{\partial \bar{T}}{\partial t} = -\frac{\partial}{\partial z}\left(\frac{H}{\rho C_{\mathrm{p}}}\right) + 2A(z)(T_1 - \bar{T})/r_{\mathrm{b}}(z)$$

$$\frac{\partial \bar{q}}{\partial t} = -\frac{\partial}{\partial z}\left(\frac{E}{\rho}\right) + 2A(z)(q_1 - \bar{q})/(r_{\mathrm{s}}(z) + r_{\mathrm{b}}(z)) \tag{4.65}$$

$$\frac{\partial e}{\partial t} = \frac{\tau_x}{\rho}\frac{\partial \bar{u}}{\partial z} + \frac{\tau_y}{\rho}\frac{\partial \bar{v}}{\partial z} + \frac{g}{T}\frac{H}{\rho C_{\mathrm{p}}} + \frac{\partial}{\partial z}\left(K_{\mathrm{M}}\frac{\partial e}{\partial z}\right)$$

$$- \frac{(Ce)^{3/2}}{l_{\mathrm{M}}} + C_{\mathrm{d}}A(z)(\bar{u}^2 + \bar{v}^2)^{3/2}$$

where u, v, T, q are the mean velocity components, potential temperature and specific humidity, respectively. The symbol overbar indicates the Reynolds Averaged Quantities. u_{g} and v_{g} denote the components of geostrophic wind, while $f = 2\Omega \sin \phi$ is the Coriolis parameter with $\Omega = 7.27 \times 10^{-5}$/s, ϕ the local latitude. ρ is the density of atmosphere, C_{P} the heat capacity, g the acceleration of gravity. e the turbulent kinetic energy, τ_x and τ_y are shear stress

components, H and E the sensible and latent heat transfer fluxes, respectively. For flows in ABL, the Boussinesq approximation is usually assumed, meaning atmosphere is regarded as incompressible except in the buoyancy term. And people tend to use $K-e$ model to close RANS equations, in which the turbulent diffusivity for momentum, energy and mass can be proportional to the mixing length written as:

$$K_{MM,H,E} = l_{M,H,E}(Ce)^{1/2} \tag{4.66}$$

where the mixing length are dependent on the stratification states and their expressions are omitted here for brevity. C_d is the aerodynamic drag, r_b and r_s are the impedance corresponding to leaf boundary layer and stomata, respectively, $A(z)$ denotes leaf area index, which turns out to zero for bare land.

Similarly, we may derive the equations for heat and water in soil:

$$\frac{\partial T}{\partial t} = \frac{\partial}{\partial z}\left(\lambda \frac{\partial T}{\partial z}\right)$$
$$\rho_w \frac{\partial \theta}{\partial t} = \frac{\partial}{\partial z}\left(K(\theta,T)\frac{\partial p(\theta,T)}{\partial z}\right) - \rho_w g \frac{\partial}{\partial z}K(\theta,T) - S(z,T)$$

where T and θ are temperature and volumetric water content in soil, λ the thermal conductivity, C the volumetric heat capacity, ρ_w the density of water, p the pressure potential and $K(\theta,T)$ the hydraulic conductivity. $S(z,t)$ is the water absorption function for roots (Molz, 1981) written as:

$$S(z,t) = \frac{E_c(t)L(z)f(\theta)}{\displaystyle\int_0^{L_r} L(z)f(\theta)\mathrm{d}z} \tag{4.68}$$

where $E_c(t)$ is the flux of transpiration, $L(z)$ the root density distribution function, $f(\theta)$ a function associated with water absorption resistance of root implying reduction of water absorption as soil moisture is less than field capacity until wilting point.

With seven variables, we specify the corresponding conditions as vanished normal derivatives at upper and lower boundaries, respectively. In addition, we require equilibrium in energy transfer at the interface between atmosphere and land to determine the temperature at the ground, thus leading to:

$$R_n + H + LE = G \tag{4.69}$$

where R_n is the net radiation, H and E are sensible and latent heat flux and finally G is the ground heat flux. No doubt, the iteration is unavoidable in the computation for satisfying the last condition.

c. *Large Eddy Simulation*

During the last two decades, people have commonly recognized the role of large eddy simulation (LES) as a powerful research tool, which is most suitable for unsteady three-dimensional complex turbulent flows in industry and natural environment. The main point in LES is that the large-scale motion is resolved while the small scale motion is modeled or, in geophysical terminology, parameterized. On the one hand, LES obtains three-dimensional unsteady instantaneous flow fields to yield any statistical quantities instead of the Reynolds averaged ones, which relies on great many empirical constants. On the other hand, LES seems more perspective to simulate the complex flows in the foreseeable future due to its moderate CPU time and storage memory demands. Initial applications are mainly focused on the geophysical fluid flows, in particular, the convective atmospheric boundary layer (Deardorff, 1970). Recently, the scope of research has extended to additional geophysical as well as industrial flows which exhibit complicated features such as stable boundary layer, turbulence in plant canopy, compressible flows, acoustics and combustion (Galperin and Orszag, 1993; Piomelli 1999; Li, 2001b).

The investigation of turbulence over and in plant canopy is of significance due to demand in understanding terrestrial processes. Previous research was based on the models such as biosphere–atmosphere transfer scheme (BATS) and simple bioshere model (SiB). Turbulent modeling and LES for planetary boundary layer was introduced in the last decades (Deardorff, 1970; Moeng, 1984). With the same vegetation model as in the previous research, we present a new subgrid model for turbulence within and over vegetative canopy in this paragraph.

The earliest subgrid scale (SGS) model of dissipative eddy viscosity is due to Smagorinsky (1963). As we know, SGS stress tensor can be decomposed into isotropic and an-isotropic components. The former determines the rate of global SGS dissipation, namely, the net energy flux from the resolved to the unresolved scales while the latter determines the mean shear stress and therefore the mean velocity profile (Baggett, 1997). Modeling dissipation and stress are two different tasks fulfilled by different models. It has been shown that modeling the former is absolutely of primarily significance. It seems that LES is able to reproduce characteristics of moderately complex turbulent flows such as mean velocity and rms velocity fluctuation even if they are mostly based on the variants of the Smagoringsky mode.

To describe the energy cascade drain, Smagorinsky (1963) assumed that SGS stress may be represented as:

$$\tau_{ij} = -2\nu_{\mathrm{T}}\bar{S}_{ij} \tag{4.70}$$

where

$$\bar{S}_{ij} = \frac{1}{2}\left(\frac{\partial \bar{u}_i}{\partial x_j} + \frac{\partial \bar{u}_j}{\partial x_i}\right) \tag{4.71}$$

is the strain rate, ν_T the eddy viscosity defined as the product of the mixing length of grid size Δ and the velocity difference at this length scale:

$$\nu_T = (C_s\Delta)^2|\bar{S}| \tag{4.72}$$

and

$$|\bar{S}| = (2\bar{S}_{ij}\bar{S}_{ij})^{1/2} \tag{4.73}$$

The determination of the Smagoringsky constant C_s ranging from 0.18 to 0.23, even reduced to 0.10 for most practical flows is crucial for correct estimation of dissipation. The presence of shear near the wall or in transitional flows diminishes the dissipation.

Since the Smagoringsky model is valid only for convective ABL far above the underlying surface, whereas structure–function model becomes more suitable by considering overestimation of dissipation due to intermittence and under-development of small-scale motion in shear turbulence (Lesieu and Metais, 1996). Then, we assume the viscosity coefficient as:

$$\nu_M = \beta\nu_{M1} + (1 - \beta)\nu_{M2} \tag{4.74}$$

$$\nu_{M2} = 0.105C_K^{-3/2}\Delta F(x,\Delta)^{1/2} \tag{4.75}$$

$$F(x,\Delta) = \frac{1}{6}\sum_{i=1}^{3}[|u(x) - u(x + \Delta x_i e_i)|^2 + |u(x) - u(x - \Delta x_i e_i)|^2] \tag{4.76}$$

where ν_{M1} and ν_{M2} are those for convection or shear dominant region, β a ratio ranging from 0 to 1 representing situation in the vicinity of or far from canopy top. F is the local structure-function of filtered velocity field of the second order (Li and Xie, 1998).

2. *Observations*

Despite of expensive investment, field experiments are always indispensable for model validation in the atmosphere–land process research. The most influential international projects in this field are First ISLSCP Field Experiment (FIFE), Hydrological Atmosphere Experiment (HAPEX) and Heihe River Basin Field Experiment (HEIFE) under the framework of World Climate Research Program (WCRP) and International Biosphere–Geosphere Program (IGBP)

(Ye and Lin, 1995). In FIFE, synchronized observations of varying terrestrial process due to grazing and wildfire were conducted within an area of 15×15 km^2 at the middle of Kansas State, USA by satellite, airplane and ground-based equipment. HAPEX-MOBILHY over a field of 100×100 km^2 in the southwest of French, where scattered were mixture crops or forest (mainly pine) was implemented by an observatory network equipped with automatic meteorology and hydrology apparatus. However, HEFEI was firstly initiated by famous Chinese meteorologists D.Z. Ye in May 1986 at a WCRP meeting in Geneva. Chinese and Japanese scientists were jointly performing 5 years' observations in the middle reach of the Heihe River along Hexi corridor, Gansu province with an area of 70×90 km^2. In particular, people have implemented intensive observation at the border of desert, gobi and oasis in order to better understand the ABL structure, radiation, water budget and turbulent flux in arid areas. Objectives of the large-scale projects mainly aim at global and regional climate research as well as meteorology study.

Since 1950s, Chinese Academy of Sciences started to establish field experiment observatories. Up to now there have been tens of observatories available, representing typical ecological systems such as crops, forest, grassland, meadow, desert, glacier and marine biology. They have become centers of long-term observation and scientific research and a window open to the world community (CAS, 1988). In regard to atmosphere–land process study, we have a constant collaboration with Shapotou Desert Research Station, Yucheng Experimental Station and Aksu water Budget Experimental Research Station by joint projects. For instance, Shapotou Station located at $37°27'$N and $104°57'$E belongs to the semi-arid area of northwest inner land with a hot, dry and windy climate. The average temperature in this area is $9.6°$C and the unevenly distributed precipitation, mainly in July to September, is 186.2 mm on average. Due to low relative humidity (usually 40%, the lowest is 10%, especially in spring) and strong winds (averaging 5 m/s over 200 days), sand transport is very severe. There is little vegetation coverage because of deep underground water table and poor water-holding ability of sandy soil (usual water capacity is 2–3%). One or two experiments have been conducted nearly every year. Apart from routine weather and hydrology observations by local engineers, we have performed different kinds of measurements by a MAOS-1 automatic meteorology observation system, including net pyrradiometer by TBB-1 sensor, heat flux into ground by CN-3 thermal flux plate, ground and soil temperature by HBW-2 and HBW-2B sensors. To explore boundary layer structure, tower-mounted instruments at different heights are used: for instance, specific moisture by HTF-2 ventilated psychrometer sensor and wind speed cup or sonic anemometers. In dense vegetation layer, we would rather use more sensitive wind

sensor VF-1 with magnetic bear and EC9-b wind direction sensor with high
frequency response. As for water content in soil, we usually measure it by
weighting augered soil and evapotranspiration by Lysimeter for low moisture
cases (Kaimal and Finnigan, 1994; Li and Ouyang, 1996; Yao *et al.*, 2001).

3. *Discussion on Water and Air Motions in SPAC System*

a. *Water Requirement of Plants*

Numerical simulation has been conducted for the fields with bare soil or
covered with Caragana korshinskii or Artimisia ordisica during 20–27th,
September, 1993. The soil there consists of fine sand containing little organic
matter, calcium carbonate and nutrient. Its field capacity of water is 3.34–3.96%
and wither capacity 0.7%. We have compared the simulated soil temperature and
water content in agreement with measurement. The variations of evapotranspira-
tion over Caragana korshiskii and Artemisia ordosica have been shown in Figs. 31
and 32 (Li *et al.*, 1997). We find that the evapotranspiration by Caragana
korshinskii is larger, implying that Artemisica ordosica with little water
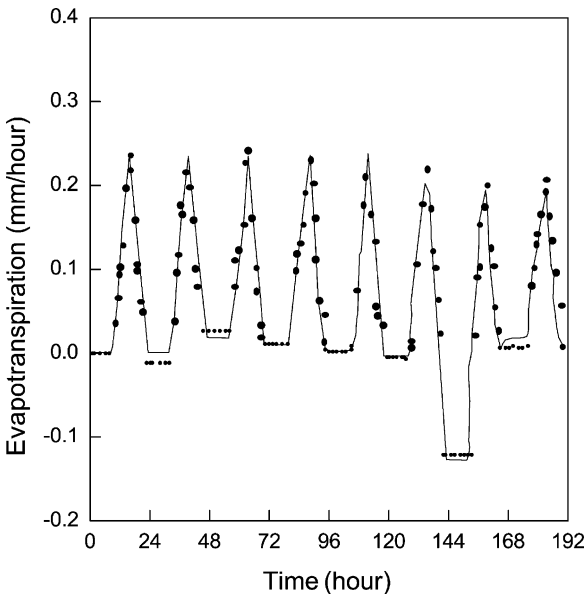requirement among drought-enduring plants is preferred in order to save water.

FIG. 31. Variation of evapotranspiraton from *Caragana korshiskii* with time solid line indicates
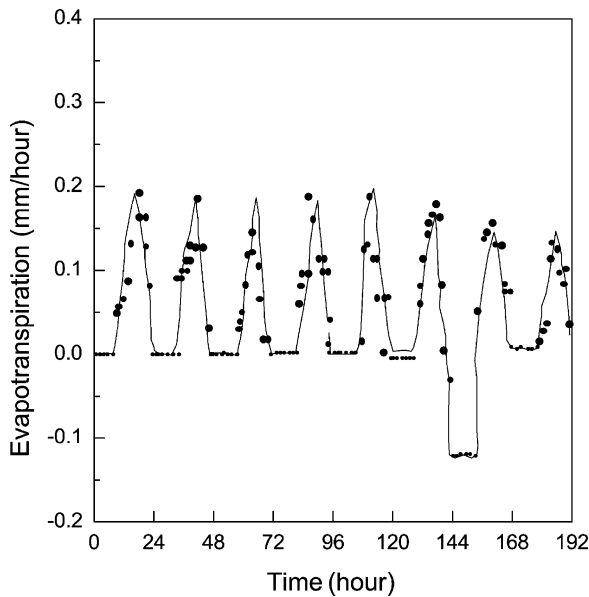numerical data; dash line indicates observation data at Shapotou during Sepp. 20–27, 1993.

FIG. 32.   Variation of evapotranspiraton from *Artemisia ordosica* with time solid line indicates numerical data; dash line indicates observation data at Shapotou during Sepp. 20–27, 1993.

Quantitatively, the total amount of evapotranspiration for Caragana korshinskii is around 1.4 mm/d, almost double of that for bare soil. The evapotranspiration for Artemisia ordosica is in between. Usually, evapotranspiration may reach maximum at 15:00 p.m. and then reduce to minimum late in the night. A drizzle is responsible for negative evapotranspiration during the seventh night on September 25, 1993.

b. *Roles of Dry Layer and Biological Crust Skin*

As stated in the previous paragraph, 68.7% of precipitation occurs in June to September. Annually, 50 days on average are rainy with 10 days larger than 5 mm and seldom continuous precipitation. We may find that there are two factors in moisture distribution in soil to restrict water supply and plant growth. Figs. 33 and 34 (Li *et al.*, 1997) provide volumetric capacity of water in the soil by numerical simulation and observations. Obviously, a dry sand layer with moisture only around 1% can be identified at the depth of 6–7 cm and the most humid layer occurs at the depth of 50 cm or so. The reason for the phenomenon is that little precipitation and fierce evaporation in arid areas prevent water from penetrating into the deep layer. If precipitation is less than 8 mm, it is even not enough to wet upper dry sand and therefore regarded as ineffective. Moreover,
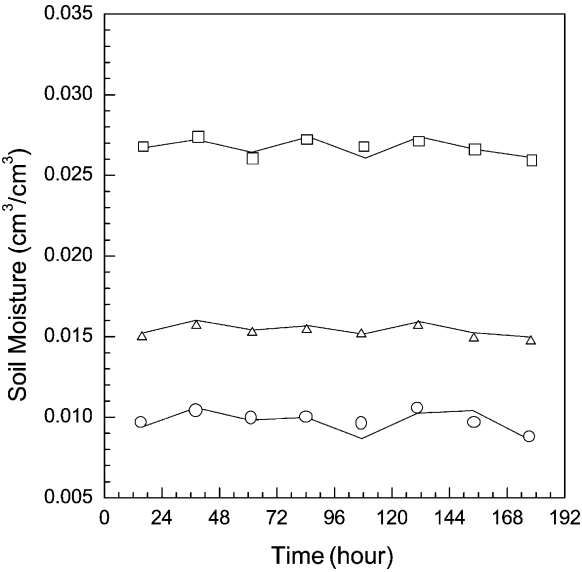
FIG. 33.   Variation of soil moisture at the surface, depths of 50 and 120 cm with time. Solid line indicates numerical simulation; blank circles, triangles and squares denote measurements at different depths at Shapotou during Sep. 20–27, 1993.
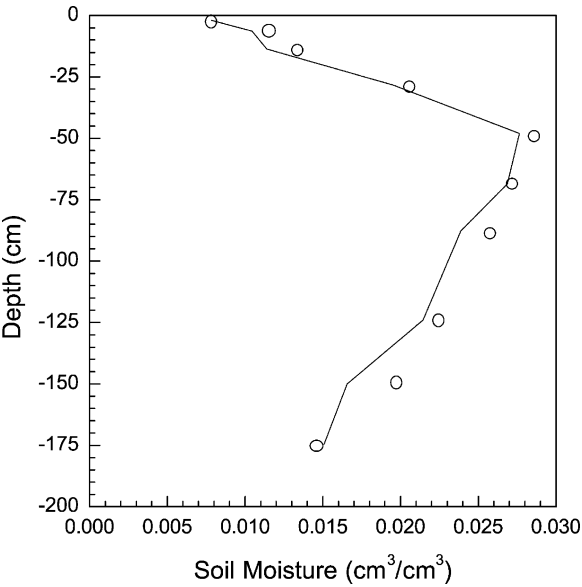

FIG. 34.   Vertical profile of soil moisture. Solid line indicates numerical simulation; blank circles denote measurements at different depths at Shapotou during Sep. 20–27, 1993.

deeper underground water may not reach soil of shallow layer. On the other hand, there has formed a biological crust skin in the elder plant region due to dust deposition and rotted fading material accumulation in microorganism environment. Consisting of 12.6–28.7% of silt and 1.78–3.88% of clay grains and covered with moss, the sponge-like biological crust skin usually may contain much more water than sand. Despite its capability of erosion resistance, the crust skin reduces water infiltration into deep layer. Observation shows that soil water content in the elder plant region with thicker crust skin of 1.5–2.0 cm is less than that with thinner crust skin in the younger plant region. The forgoing described climate and soil water distribution factors account for the continuous reduction of moisture in deep soil layer of 100–200 cm in elder plant region, which leads to the overspread of shallow root plants and the degeneration of deep root trees. Generally, rare vegetation flourishes and dense vegetation fades. Therefore, the optimal distance between individual plants is proved 1.5 m instead of 1 m (Li and Wu, 1998; Yao *et al*., 2001).

c. *Turbulent Structure Within and Over Vegetation Canopy*

We have simulated a region of $192 \, \text{m} \times 192 \, \text{m} \times 64 \, \text{m}$ with $96 \times 96 \times 32$ grids, and integrated 6400 time steps of 0.1 s by LES. The computations are conducted on SGI Origin 2000 parallel supercomputer at LASG, CAS for 11 h for each case. Convective and weakly convective ABL with the Monin–Obukhov length $-40 \, \text{m}$, $-700 \, \text{m}$ and LAI 2, 5 have been calculated as examples (Li and Xie, 1999). Mean horizontal velocity profile, Reynolds stress and turbulent kinetic energy have been simulated and well compared with both observation and simulation results (Shaw and Schumann, 1992; Shaw *et al*., 1988; Patton, 1997) (see Figs. 35–38, Li, 2001a). This model also exhibits smaller fraction of SGS energy than Patton's (1997). Such organized structure of ramp pattern in temperature scalar field has been observed for strong convective ABL by Gao *et al*. (1989). It means that a sharp sloping frontal between relatively warm, humid air being expelled from the forest and cooler, drier air being swept into the canopy from aloft. This kind of turbulent structure caused by strong velocity shear is responsible for the exchange of warm and cold air in ejection and down sweeping process. In the simulation of turbulence within and above the vegetation canopy, we have also identified such structure for strong convective situation by this new model. About 15% of the tree height over the canopy, we may find a slant front of width 3–6 m with drastic temperature variation separating warm and cold regions (see Figs. 39–40, Li, 2001a).
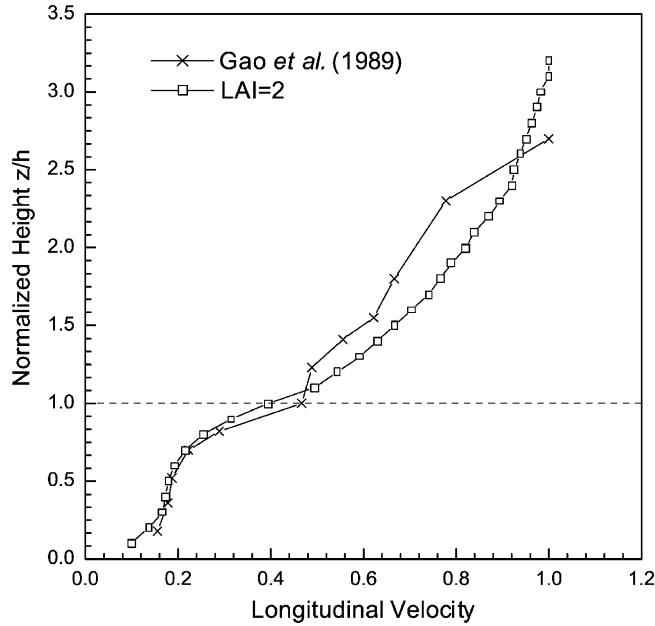
Li Jiachun et al.

FIG. 35. Comparison of longitudinal velocity profile within and over a forest with LAI = 2.
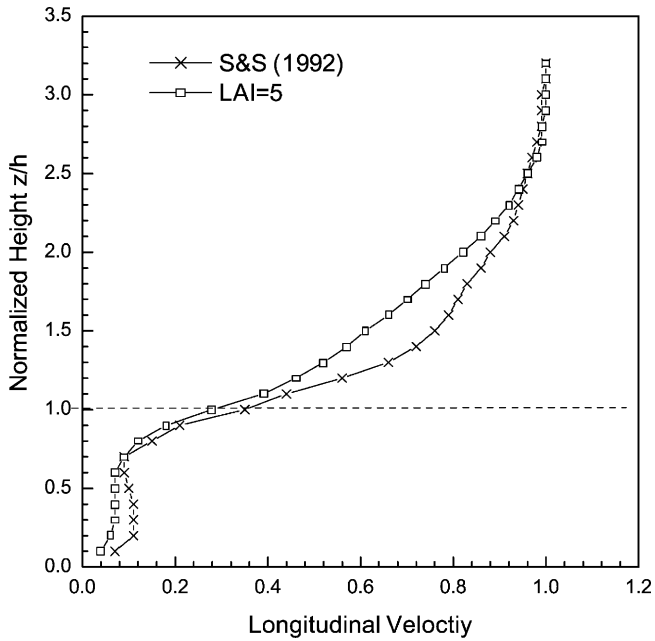

FIG. 36. Comparison of longitudinal velocity profile within and over a forest with LAI = 5.
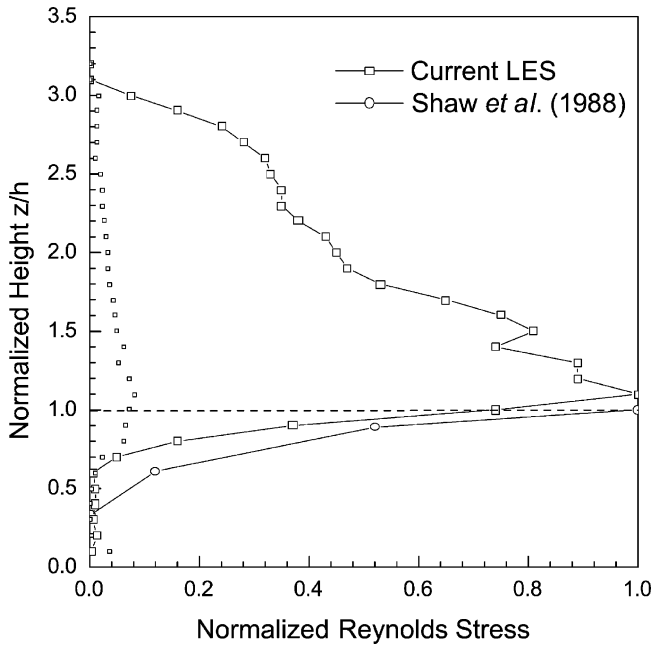
Fig. 37. Comparison of Normalized Reynolds stress within and over a forest by LES, where blank squares denote numerical simulation for resolved and unresolved components; blank circles denote numerical simulation by Shaw *et al.* (1988).

V. Concluding Remarks

As we have previously stated in the present article that although people have come to adequately recognize the significance of environment protection and sustainable development, China is still confronting twofold pressure. One is from swift economic development at the annual rate of 7–8% in GDP and endeavor to complete the transition to a developed country in tens of years. Another is from delayed growth peak in population despite of successful family planning policy during past decades. Major sources to generate environment hazards in today's China are found to be unfavorable distribution in water resources and coal burning. Certainly, radical alleviation of these problems can substantially ameliorate China's living surroundings in future.

Resolution of these environmental issues that are obviously interdisciplinary, of multiple scales and multi-composition in nature needs joint efforts of scientists from relevant communities of scientific branches. The central tasks of scientists in environmental fluid mechanics circle should be at first focused on clarifying
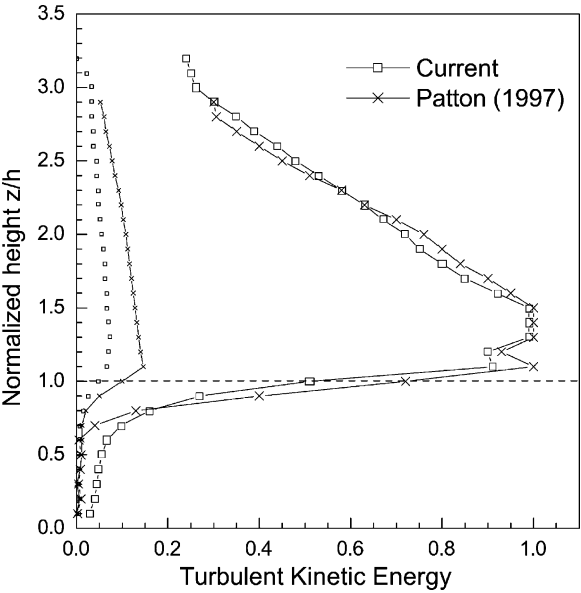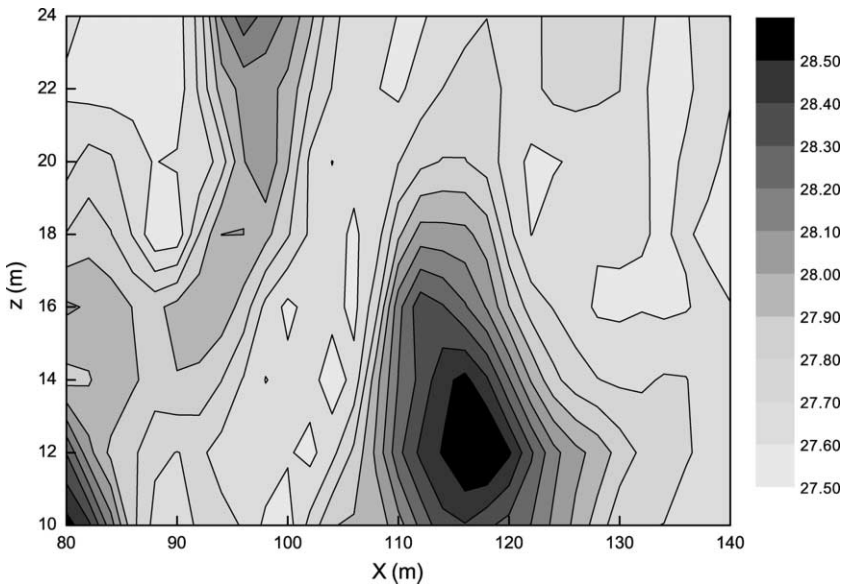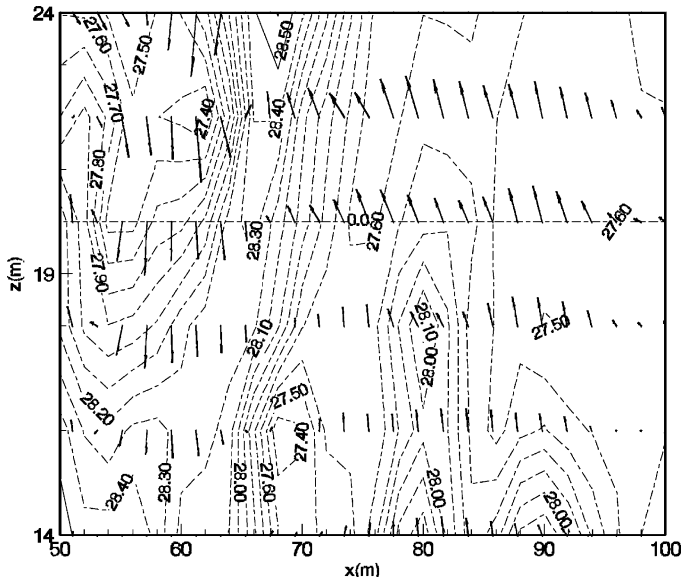
FIG. 38. Comparison of Turbulent kinetic energy within and over a forest by LES, where blank squares denote numerical simulation for resolved and unresolved components; solid crosses denote numerical simulation by Patton (1997). The present results with smaller proportion of subgrid energy are better than Patton's results.

dynamic processes to better understand how natural flows in atmosphere, hydrosphere, geosphere and biosphere accompanied with momentum, energy and mass transfer occur, instead of direct prediction or forecast of an environment event from the very beginning. Therefore, the proper objective of their research aims at qualitatively describing environment episode or designing typical experiments on small scale in order to reveal the mechanism implied in them. Then, we should manage to answer these questions, which remain open to us or still in controversy. Through this kind of process-based research, we are now in a position to improve existing somewhat empirical engineering approaches and enhance quantitative accuracy in prediction. Finally, the numerical simulation based on thus established models, which have been validated and proved credible by comparison with observation, becomes such a powerful tool for prediction, assessment and manipulation of environmental events in order to partly replace expensive long-term and large scale field experiments. The ultimate goal may very likely be to provide a scientific foundation for policy-makers in decision from macroscopic and strategic point of view.

To illustrate this process-based research approach, three typical examples associated with the Yangtze River Estuary, Loess Plateau and Tenggli Desert

FIG. 39. Velocity field and thermal contours nearby a forest canopy, where a temperature ramp structure can be clearly identified for a strongly convective boundary layer ($L = -40$ m).

FIG. 40. A typical ramp structure of temperature over a forest canopy for a strongly convective atmospheric boundary layer.

environments have been dealt with, respectively. A theoretical model of vertical flow field accounting for runoff and tide interaction has been established to delineate salinity and sediment motion in the estuarine region. We have simulated diurnal and seasonal variations of salt front and turbidity maximum, which are responsible for the formation of mouth bar at the outlet of a river and the evolution of ecological environment there. A kinematic wave theory combined with the revised Green–Ampt infiltration formula is applied to the prediction of runoff generation and erosion in three types of erosion region on the Loess Plateau in excellent accord with observational reality. A new rule of runoff routing we put forward is able to properly recover two-dimensional overland flows on rugged slope. Moreover, the influential factors of dominant rill erosion compared to inter-rill erosion can be used as valuable references in returning reclaimed sloping land into vegetation covered field as an effective measure of erosion prevention. Three approaches describing water motion in SPAC system at different levels have been improved by introducing vegetation sub-models, which have ability to reflect momentum, moisture and heat transfer between atmosphere and land in arid areas. As drought-enduring plants grow up, the water requirement is necessarily rising. However, we have found that the formation of a dry sandy layer and biological crust skin are additional primary causes leading to deterioration of water supply and succession of ecological system. To enlarge distance between individual plant, to select water-saving trees and to artificially break crust skin therefore seem to be suitable measures for windbreak to survive for a longer time. Facing such a tough task in a country with vast territory and more than one billion of population, we certainly need sustainable efforts in research and in harness of natural environment. As a result, we ultimately achieve sustainable development in economy and society. At the same time, we should also take an active part in the study of those problems relevant to global environments and industrial processes.

Acknowledgments

Appendix: Acronyms

ABL	Atmosphere Boundary Layer (p230)
BATS	Biosphere–Atmosphere Transfer Scheme
CAS	Chinese Academy of Sciences (p297)
CBL	Convective Boundary Layer
CFC	ChloroFluroCarbons (p237)
DMS	DiMethyl Sulphide
FIFE	First ISLSCP Field Experiment (p296)
HAPEX	Hydrological Atmospheric Pilot EXperiment program
HEIFE	EEIhe river basin Field Experiment
HWR	High Water Rapid (p241)
HWS	High Water Slack
IGBP	International Geosphere–Biosphere Program
INDNR	International Decade of Natural Disaster Reduction (p225)
ISLSCP	International Satellite Land Surface Climatology Project
LAI	Leaf Area Index (p301)
LES	Large Eddy Simulation (p295)
LUCC	Land Use and Cover Change
LWR	Low Water Rapid
LWS	Low Water Slack
MRP	Middle Route Project (p227)
NCAR	National Center for Atmospheric Research
SBL	Stable Boundary Layer
SGS	Subgrid Scale model
SiB	Simple Biosphere model
SPAC	Soil–Plant–Atmosphere Continuum (p291)
UNCED	United Nation Conference on Environment and Development
UNCHE	United Nation Conference on Human Environment (p224)
UNEP	United Nation Environment Program
WCRP	World Climate Research Program

References

Alonso, C. V., Neibling, W. H., and Foster, G. R. (1981). Estimating sediment transport capacity in watershed modeling. *Trans. Am. Soc. Agric. Eng.* **24,** 1211–1226.

Baggett, J. S. (1997). Some modeling requirement for wall models in large eddy simulation. *Annual Research Reports*, pp. 123–134, CTR, Stanford University.

Beniston, M. (1998). *From Turbulence to Climate*. Springer-Verlag, Berlin.

Bernard, J. N. (1981). *Environmental Sciences, the Way the World Works*. Prentice-Hall, Englewood Cliffs.

Bigg, G. R. (1996). *The Oceans and Climate*. Cambridge University Press, Cambridge, New York and Melbourne.

Brenner, M. P., and Stone, H. A. (2000). Modern classical physics through the work of G.I. Taylor. *Phys. Today* **5,** 30–35.

Cao, Z. X. (1997). Turbulent bursting-based sediment entrainment function. *J. Hydr. Engng* **123**(3), 233–236.

CAS (1988). *Introduction of Field Experiment Observatories*. Science Press, Beijing.

Chen, Y. Z. (1996). Soil erosion in Loess Plateau. In *Soil and Water Conservation in Loess Plateau* (Q. M. Meng, and Z. Zheng, eds.), Yellow River Hydraulic Press.

Chen, L., and Liu, Q. Q. (2001). On the equations of overland flow and one-dimensional equations for open channel flow with lateral inflow. *Mech. Engng* **23**(4), 21–24.

Chen, Y. Z., Jing, K., and Cai, Q. G. (1988). *Modern Erosion and Regulation in Loess Plateau*. Science Press, Beijing.

Chen, G. X., Xie, S. N., and Tang, L. Q. (1996). On the erosion and sediment generation model of watershed in Loess Plateau region. In *Soil and Water Conservation in Loess Plateau* (Q. M. Meng, and Z. Zheng, eds.), Yellow River Hydraulic Press.

Chen, L., Liu, Q. Q., and Li, J. C. (2001a). Study on the runoff generation process on the slope with numerical method. *J. Sediment Res.* **2001**(4), 61–68.

Chen, L., Liu, Q. Q., and Li, J. C. (2001b). Runoff generation characteristics in typical erosion regions on the Loess Plateau. *Int. J. Sediment Res.* **16**(4), 473–485.

Chien, N., and Wan, Z. H. (1986). *Mechanics of Sediment Transport*. Science Press, Beijing. Also Chien, N., and Wan, z. W., (1998) by ASCE Press, Reston.

Chu, T. (1978). Infiltration during an unsteady rain. *Water Resour. Res.* **14**(3), 461–466.

Deardorff, J. W. (1970). Convective velocity and temperature scales for unstable planetary boundary layer and for Rayleigh convection. *J. Atmos. Sci.* **27,** 1211–1213.

Deardorff, J. W. (1978). Efficient prediction of ground surface temperature and moisture with inclusion of a vegetation layer. *J. Geophys. Res.* **83,** 1889–1903.

Dingman, S. L. (1994). *Physical Hydrology*. Macmillan Publishing Co, New York.

Dou, G. R. (1999). Incipient motion of coarse and fine sediment. *J. Sediment Res.* (6), 1–9.

Emmett, W. W. (1978). Overland flow. In *Hillslpoe Hydrology* (M. J. Kirkby, ed.), pp. 145–175, Wiley, New York.

Finnigan, J. (2001). Turbulence in plant canopy. *Annu. Rev. Fluid Mech.* **32,** 519–570.

Foster, G. R., and Meyer, L. D. (1977). Soil erosion and sedimentation by water—An overview. *Proceedings of a National Symposium on Soil Erosion and Sedimentation by Water*, 1–13.

Fuwa, K. (1995). *Earth Environment Handbook*. Asakura Publishing Co, Japan.

Galperin, B., and Orszag, S. A. (1993). *Large Eddy Simulation of Complex Engineering and Geophysical Flows*. Cambridge University Press, Cambridge and Oakleigh.

Gao, W., Shaw, R. H., and Paw, U. K. T. (1989). Observation of organized structure in turbulent flow within and above a forest canopy. *Boundary Layer Meteorol.* **47,** 349–377.

Garratt, J. R., and Taylor, P. A., eds. (1996). *Boundary-Layer Meteorology: 25th anniversary volume 1970–1995*. Kluwer Academic Publisher, Netherland.

Govers, G. (1992). Evaluation of transporting capacity formulae for overland flow. In *Overland Flow* (A. J. Parsons, and A. D. Abrahams, eds.), pp. 243–273, UCL Press.

Govindaraju, R. S. (1988). On the diffusion wave model for overland flow. *Water Resour. Res.* **24**(5), 734–754.

Grubert, J. P. (1989). Interfacial mixing in stratified channel flows. *J. Hydr. Div., ASCE* **115**(7), 887–905.

Grubert, J. P. (1990). Interfacial mixing in estuaries and fjords. *J. Hydr. Engng* **116**(2), 176–195.

Gu, X., Yuan, Q., Shen, H., and Zhou, Y. (1995). The ecological study on phytoplankton in maximum turbid zone of Changjiang Estuary. *J. Fish. Sci. China* **2**(1), 16–27.

Hamilton, D. P., and Schladov, S. G. (1997). Prediction of water quality in lakes and reservoirs. *Ecological modeling* **96,** 91–123.

Hopfinger, E. J. (1988). Turbulence and vortices in rotating fluids. In *Theoretical and Applied Mechanics* (P. Germain, eds.), North Holland.

Horton, R. E. (1940). An approach toward a physical interpretation of infiltration-capacity. *Soil. Sci. Soc. Am. Proc.* **5,** 399–417.

Huang, C.-h., Bradford, J. M., and Laflen, J. M. (1996). Evaluation of the detachment-transport coupling concept in the WEPP rill erosion equation. *Soil Sci. Soc. Am. J.* **60,** 734–739.

Jackson, R. G. (1976). Sedimentological and fluid dynamics implications of the turbulent bursting phenomenon in geophysical flows. *J. Fluid Mech.* **77,** 531–560.

Jiang, D. S. (1997). *Soil and Water Loss in Loess Plateau and the Regulation Mode*. Hydraulic and Water Power Press, Beijing.

Jager, J. (1988). *Climate and Energy System*, IIASA.

Kaimal, J. C., and Finnigan, J. J. (1994). *Atmospheric Boundary Layer Flows, Their Structure and Measurement*. Oxford University Press, Oxford.

Kuang, C.P. (1993). A study on changes of mouth bar and suspended sediment settlement in the Changjiang River Estuary and mathematical model for flow and transport of salinity and sediment. Doctoral Thesis, Nanjing Institute of Water Conservancy.

Kurup, G. R., Hamilton, D. P., and Patterson, J. C. (1998). Modeling the effect of seasonal flow variations on the position of salt wedge in a microtidal estuary. *Estuar. Coast. Shelf Sci.* **47,** 191–208.

Lamb, H. (1945). *Hydrodynamics*. Sixth edition, Dover, New York.

Lei, X. E., Han, Z. W., and Zhang, M. G. (1998). *Physical, Chemical, Biological Processes and Mathematical Model on Air Pollution*. China Meteorological Press, Beijing.

Lesieu, M., and Metais, O. (1996). New trends in large eddy simulation of turbulence. *Annu. Rev. Fluid Mech.* **28,** 15–82.

Levich, V. G. (1962). *Physico-Chemical Hydrodynamics*. Prentice-Hall, Englewood Cliffs.

Li, J. C. (1993). *Turbulence in atmosphere and ocean. New Trends in Theoretical Physics and Fluid Mechanics*, Peking University Press, Beijing, pp. 427–133.

Li, J. C., ed. (2001a). *Nature, Industry and Fluid Flows*. Meteorology Press, Beijing.

Li, J. C. (2001b). Large eddy simulation of complex turbulent flows: physical aspects and research trends. *Acta Mechanica Sinica* **17**(4), 289–301.

Li, J. C., and Kwok, Y. K. (1997). Vortex dynamics in the study of looping in tropical cyclone tracks. *Fluid Dynamic Res.* **21,** 57–71.

Li, J. C., and Ouyang, B., eds. (1996). *Modeling and Observation in Terrestrial Processes*. Science Press, Beijing.

Li, J. C., and Wu, C. K. (1998). Environmental mechanics and sustainable development. *Adv. Mech.* **18**(4), 433–439.

Li, J. C., and Xie, Z. T. (1998). *Subgrid models in large eddy simulation. Proceedings of International Conference on Nonlinear Mechanics* (W. C. Tsien, ed.), Shanghai Univ. Press.

Li, J. C., and Xie, Z. T. (1999). Large eddy simulation of turbulence in canopy layer. *Acta Mechanica Sinica* **31**(4), 406–414.

Li, J. C., Yao, D. L., and Shen, W. M. (1997). Studies on terrestrial interface processes in arid areas, China. *J. Arid Environ.* **36,** 25–36.

Li, J. C., Yao, D. L., and Shen, W. M. (1999a). A coupling model of terrestrial processes in arid areas. *Appl. Math. Mech.* **20**(1), 1–10.

Li, J. C., Zhou, J. F., and Xie, Z. T. (1999b). Oscillatory boundary layer and its applications. *Adv. Mech.* **29**(4), 451–460.

Lima, J. L. M. P. (1992). Model KINNIF for overland flow on pervious surface. In *Overland Flow* (A. J. Parsons, and A. D. Abrahams, eds.), pp. 69–88, UCL Press.

Lin, J. D., and Sun, S. F. (1986). A method for coupling a parameterization of the planetary boundary layer with a hydrologic model. *J. Climate Appl. Meteorol.* **25,** 1971–1976.

Liu, C. M., and Sun, R. (1999). Ecological aspects of water cycle: advances in soil–vegetation–atmosphere of energy and water fluxes. *Advances in Water Sciences* **10**(3), 251–259.

Liu, S. H., Huang, Z. C., and Liu, L. C. (1996). Numerical simulation of transpiration in SPAC system. *Acta Geographica Sinica* **51**(2), 118–126.

Liu, Y. B., Zhou, X. M., Zhou, P. H., and Tang, K. L. (1998). The types and generation law of rill erosion of slope in Loess Plateau. *Congregate Publication of Northwest Water and Soil Preservation Institution of Chinese Science Academy* **7,** 9–18.

Liu, Q. Q., Chen, L., and Li, J. C. (2001). Influences of slope gradient on soil erosion. *Appl. Math. Mech.* **22**(5), 449–457.

Lu, J. Y., Cassol, E. A., and Moldenhauer, W. C. (1989). Sediment transport relationships for sand and silt loam soils. *Trans. Am. Soc. Agric. Eng.* **32,** 1923–1931.

Luo, B. Z., and Shen, H. T. (1994). *Three-gorge Project and Ecological Environments in Estuary.* Science Press, Beijing.

Lumley, J. L., Acrivos, A., Gary Leal, L., and Leibovich, S. (1996). *Research Trends in Fluid Dynamics.* AIP, New York.

Mein, R. G., and Larson, C. L. (1973). Modeling infiltration during a steady rain. *Water Resour. Res.* **9**(2), 384–394.

Mellor, G. L., and Yamada, T. (1974). A hierachy of turbulence closure models for the planetary boundary layer. *J. Atmos. Sci.* **31,** 1791–1806.

Moeng, C.-H. (1984). A large eddy simulation model for the study of planetary boundary layer turbulence. *J. Atmos. Sci.* **41**(13), 2052–2062.

Molz, F. J. (1981). Models of water transport in the soil–plant system: A review. *Water Resource Res.* **17**(5), 1245–1260.

Moore, I. D., and Burch, G. J. (1986). Sediment transport capacity of sheet and rill flow: Application of Unit Stream Power Theory. *Water Resour. Res.* **22,** 1350–1360.

Naot, O., and Mahrer, Y. (1989). Modeling microclimate environments: a verification study. *Boundary Layer Meteorol.* **46,** 333–354.

Nielsen, P. (1992). *Coastal Bottom Boundary Layers and Sediment Transport. Advanced Series on Ocean Engineering*, Vol. **4** JBW Printers and Binders Pte. Ltd, Singapore.

Nino, Y., and Garcia, M. H. (1996). Experiments on particle–turbulence interactions in the near-wall region of an open channel flow: implications for sediment transport. *J. Fluid Mech.* **326,** 285–319.

Parsons, A. J., and Abrahams, A. D. (1992). *Overland Flows: Hydraulics and Erosion Mechanics*, UCL Press, London.

Patton, E. G. (1997) Large eddy simulation of turbulent flow within and above a plant canopy, Doctorial dissertation of the University of California.

Philip, J. R. (1957). The theory of infiltration. *Soil. Sci.* **84,** 254–264.

Phillips, O. M. (1977). *The Dynamics of Upper Ocean.* Cambridge University Press, Cambridge.

Piomelli, U. (1999). *Large eddy simulation: achievements and challenges. Progress in Aerospace Science*, pp. 335–365.

Ponce, V. M., Li, R. M., and Simons, D. B. (1978). Applicability of kinetic and diffusion models. *J. Hydr. Div. ASCE* **104,** 353–360.

Qi, L. X., and Huang, X. F. (1997). The numerical simulation on runoff generation and soil erosion on slope. *Acta Mechanica Sinica* **29**(3), 343–348.

Reible, D. D. (1999). *Fundamentals of Environmental Engineering*. Springer/Lewis Publisher, Heidelberg.

Rosenberg, N. J. (1974). *Micrometeorolog: the Biological Environment*. Wiley.

Scoging, H. (1992). Modeling overland-flow hydrology for dynamic hydraulics. In *Overland Flow* (A. J., Parsons, and A. D., Abrahams, eds.), pp. 89–103, UCL Press.

Shaw, R. H., and Schumann, U. (1992). Large eddy simulation of turbulent flow above and within a forest. *Boundary Layer Meteorol.* **61,** 47–64.

Shaw, R. H., Den Hartog, G., and Neumann, H. H. (1988). Influence of foliar density and thermal stability on profiles of Reynolds stress. *Boundary Layer Meteorol.* **45,** 391–409.

Shen, B. (1996). *Finite Element Simulation on Surface Hydrology*. Xi'an Press of Xibei Technology University.

Shen, H. T., and Shi, W. (1999). The state of art of studies on biogeochemistry of turbidity maximum in some estuaries. *Adv. Earth Sci.* **14**(2), 13–14.

Singh, V. P. (1996). *Environmental Hydrology*. Kluwer Academic Publisher, Norwell and Dordrecht.

Smagorinsky, J. (1963). General circulation experiments with the primitive equations. I. Basic experiment. *Mon. Weather Rev.* **91,** 99–102.

Sun, S. F., and Lu, Z. B. (1992). A ground hydrologic model with inclusion a layer of vegetation canopy that can be interact with general circulation model. *Sci. China* **B**(2), 216–224.

Sun, S. F., Niu, G. Y., and Hong, Z. X. (1998). Modeling of water and heat transfer in soil in arid and semiarid areas. *J. Atmos. Sci.* **21**(1), 1–10.

Sutherland, A. J. (1967). Proposed mechanism for sediment entrainment by turbulent flows. *J. Geophys. Res.* **72,** 191–198.

Tan, H. S., and Ling, S. C. (1961). A study of atmospheric turbulence and canopy flow, Production Research RPYT. 72, U.S. Dept of Agriculture.

Tang, C. B. (1963). The law of sediment incipience. *J. Hydr. Eng.* **2,** 1–12. in Chinese.

Tang, L. Q., and Chen, G. X. (1994). The foundation of soil erosion formula in slope surface and its application in sediment yield calculation in watershed. *Adv. Water Sci.* **5**(2), 104–110.

Tang, L. Q., and Chen, G. X. (1997). The dynamic model of runoff and sediment generation in small watershed. *J. Hydrodyn., Ser. A* **12**(2), 164–174.

Ten Berge, H. F. M. (1990). *Heat and Water Transfer in Bare Topsoil and the Lower Atmosphere*. Pudoc Wageningen, Netherland.

Turner, J. S. (2000). Development of geophysical fluid dynamics: the experiment of laboratory experiment. *Appl. Mech. Rev.* **53**(3), 11–22.

Wang, W. Z., and Jiaos, J. Y. (1996). *Rainfall and Erosion Sediment Yield in Loess Plateau and Sediment Transportation in the Yellow River Basin*. Science Press, Beijing.

Wang, Y. J., Zhang, Z. Z., Huang, W., and Gu, J. (1995). Hydrochemical characteristics and clay minerals of suspended sediment in South Channel, Changjiang Estuary. *Mar. Sci. Bull.* **14**(3), 106–113.

Warhaft, Z. (2000). Passive scalar in turbulence. *Annu. Rev. Fluid Mech.* **32,** 203–240.

Watt, R. G. (1998). *Mathematics Applied to Sciences*. Academic Press, New York, pp. 263–309.

Woolhiser, D. A., and Ligget, J. A. (1967). Unsteady, one-dimensional flow over a plane—The rising diagram. *Water Resour. Res.* **3**(3), 753–771.

Wu, S. Y. (1992). *Study on Heat and Moisture Transfer in the Tarimu Basin*. Marine Publishing House, Beijing.

Xie, Z. T., Li, J. C., and Yao, D. L. (1998). Land-atmosphere coupling model with vegetation effects. *Acta Mechanica Sinica* **30**(3), 267–276.

Xu, Z., Wang, Y., Chen, Y., and Shen, H. (1995). An ecological study on zooplankton in maximum turbid zone of estuarine area of Changjiang (Yangtze) River. *J. Fish. Sci. China* **2**(1), 39–48.

Yang, W. Z. (1996). On soil moisture in Loess Plateau. In *Soil and Water Conservation in Loess Plateau* (Q. M. Meng, and Z. Zheng, eds.), Yellow River hydraulic Press.

Yao, D. L., Li, J. C., Du, Y., Li, X. R., and Zhang, J. G. (2001). Mechanism of the crust layer and the evolution of canopy in artificial vegetation area of Shapotou. *Acta Ecologica Sinica* **22**(4), 452–460.

Ye, D. Z., and Lin, H. (1995). *China Contribution to Global Change Studies*. Science Press, Beijing.

Zhang, K. L. (1991). A study on the relationship between distribution of erosion sediment yield and rainfall characteristics in loess slope surface. *J. Sediment Res.* **6**(4), 39–46.

Zhang, Z. Z. (1994). Analysis of Chinese energy system: implication for future CO_2 emissions. *Int. J. Environ. Pollut.* **4**(3/4), 181–198.

Zhang, K. L. (1999). Hydrodynamic characteristics of rill flow on Loess slopes. *J. Sediment Res.* **1999**(1), 56–61.

Zhang, R. J., Xie, J. H., and Wang, M. F. (1989). *Sediment dynamics in river*. Hydraulic and Water Power Press of China, Beijing.

Zheng, F. L., and Kang, S. Z. (1998). Relation and mechanism of erosion sediment yield at different erosion zone in the loess slope surface. *J. Geography* **53**(5), 422–428.

Zhou, Y. (1998). Advances in the fundamental aspects of turbulence: energy transfer, interacting scales and self-preservation in isotropic decay. *Appl. Mech. Rev.* **51**(4), 267–301.

Zhou, J. F., and Li, J. C. (1999). Modeling unsteady sediment transport in Estuaries. *The Proceedings of the 8th Asian Conference on Fluid Mechanics*, pp. 859–863, Dec. 6–10, Shenzhen.

Zhou, J. F., and Li, J. C. (2000). Estuary mixing and sediment transport. *Acta Mechanica Sinica* **32**(5), 523–530.

Zhou, J. F., Liu, Q. Q., and Li, J. C. (1999a). Mixing Process in Estuaries. *Science in China (series A)* **42**(10), 1110–1120.

Zhou, J. F., Wang, T., Li, J. C., and Liu, Q. Q. (1999b). Effects of runoff and tide on sediment transport in the Yangzhe River Estuary. *J. Hydrodyn.* **14**(1), 90–100.

Zhou, J. F., Li, J. C., and Liu, H. D. (2000). Modeling sediment transport influenced by the waterway project in the Yangtze River Estuary. *Proceedings of the 8th International Symposium on Stochastic Hydraulics, ISSH'2000*, 333–341.